

University of Louisville

ThinkIR: The University of Louisville's Institutional Repository

Electronic Theses and Dissertations

5-2012

Thermally driven Knudsen gas pump enhanced with a thermoelectric material.

Kunal Pharas 1979-
University of Louisville

Follow this and additional works at: <https://ir.library.louisville.edu/etd>

Recommended Citation

Pharas, Kunal 1979-, "Thermally driven Knudsen gas pump enhanced with a thermoelectric material." (2012). *Electronic Theses and Dissertations*. Paper 1127.
<https://doi.org/10.18297/etd/1127>

This Doctoral Dissertation is brought to you for free and open access by ThinkIR: The University of Louisville's Institutional Repository. It has been accepted for inclusion in Electronic Theses and Dissertations by an authorized administrator of ThinkIR: The University of Louisville's Institutional Repository. This title appears here courtesy of the author, who has retained all other copyrights. For more information, please contact thinkir@louisville.edu.

**THERMALLY DRIVEN KNUDSEN GAS PUMP ENHANCED WITH A
THERMOELECTRIC MATERIAL**

By

Kunal Pharas

M.S. University of Louisville, 2006

A Thesis

Submitted to the Faculty of the
J. B. Speed School of Engineering of the University of Louisville
in Partial Fulfillment of the Requirements for the Degree of

Doctor of Philosophy

Department of Electrical & Computer Engineering
University of Louisville
Louisville, KY 40292

May 2012

THERMALLY DRIVEN KNUDSEN GAS PUMP ENHANCED WITH A
THERMOELECTRIC MATERIAL

By

Kunal Pharas
M.S. University of Louisville, 2006

A Thesis Approved on

January 10, 2012

by the following Dissertation Committee:

Dr. Shamus P. McNamara (Dissertation Director)

Dr. Kevin M. Walsh

Dr. Bruce W. Alphenaar

Dr. Gamini U. Sumanasekera

Dr. Palaniappan Sethu

Dr. Ellen G. Brehob

DEDICATION

I dedicate this dissertation to my parents Mr. Binod B. Pharas & Mrs. Basabi Pharas for their support throughout my life and all the sacrifices they have made to provide me with everything I need, to all my teachers for the knowledge and wisdom they gave me, and to my extended family who have made my life rich and fulfilling.

ACKNOWLEDGMENTS

I am indebted to my advisor, Dr. Shamus McNamara, for this thesis. His abundant knowledge guided me right from the start to finish making sure the project headed in the right direction and the goals were achieved. He continued to educate and support me right from my Master's degree and it was under his able guidance that I was introduced to the exciting world of MEMS and microfabrication. Whether it was theory or the practical nuances of laboratory experiments he instilled the confidence within me and made me structure my independent thought process to carry out experiments with positive results. I have learned how to be a good researcher by following his principles. I developed the insight to observe minute details which could make a difference in the outcome of an experiment. He supported me financially as a research assistant in his laboratory and gave me the opportunity to work on multiple projects which broadened my horizon, which also included the cleanroom experience.

This thesis was developed over a period of five years. The basic proof was already established by Dr. McNamara, while he was at the University of Michigan and by other researchers. I was very fortunate to have the opportunity to continue this project and to improve the performance of the project.

I would also like to thank my committee members for their time and advice and an eagerness to help me on numerous occasions. I give thanks to: Dr. Walsh for educating me on microfabrication principles and providing a state of the art cleanroom in the university, Dr. Alphenaar for building solid fundamentals in physical electronics, Dr. Sethu for ideas on microfluidics, Dr. Gamini Sumanasekera for suggestions on porous thermoelectric experiments and Dr. Brehob for enlightening me with mechanical engineering concepts.

I would like to thank all my loyal friends, both graduate and undergraduate researchers for the intellectual discussions, brainstorming sessions, and timely help. Working around these exuberant personalities was always a pleasure.

Words cannot express the gratitude I owe to all the staff members of our research facility. To name a few, Mark Crain, Joseph Lake and Don Yeager helped me with my cleanroom needs. Doug Jackson helped me with machining in the later part of my research. Joe Williams maintained the scanning electron microscopes for perfect imaging of my samples.

Last but not least, I would also like to thank the Department of Electrical and Computer Engineering for providing me with teaching assistantships to a variety of undergraduate and graduate level courses to support me financially as a graduate student. I really enjoyed the time teaching and acquiring the experience of being able to help the students.

ABSTRACT

THERMALLY DRIVEN KNUDSEN GAS PUMP ENHANCED WITH A THERMOELECTRIC MATERIAL

Kunal Pharas

January 10th, 2012

The thesis focuses on improving the flowrate of the Knudsen gas pump. The Knudsen pump uses thermal transpiration as the driving mechanism to pump gas. It is a motionless gas pump as the pump does not require any moving actuators for pumping. The thermally driven gas flow is accomplished in the molecular or transitional gas flow regime. The advantage of this pump is that without any moving parts it avoids friction losses and stiction problems which devices in micro scale are prone to suffering due to scaling issues. Thus, this pump is highly robust and reliable. Knudsen pumps in the past have suffered from the drawback of low flowrates and inability to operate at atmospheric pressure. In the early days lack of micromachining technologies limited minimum channel size which had to be operated at lower than atmospheric pressure to achieve free molecular flow. Various designs have been implemented with an impetus on increasing the flowrate of the pump.

The key to this pump is establishing a temperature difference along the length of the channel. A higher temperature difference over a shorter channel length makes the

pump more efficient. Pump channels have been made out of various materials like silicon, glass and polymer. The silicon microfabricated single channel conventional design pump suffered from the high thermal conductivity of silicon, which limited the thermal gradient that could be achieved. Silicon was replaced by glass, which has a lower thermal conductivity. The glass microfluidic pump could pump water in reservoirs but at a slow rate. Renewable forms of Knudsen pump were also made by using nanoporous silica colloidal crystals which are robust and could use solar energy and body heat to create a temperature difference and achieve pumping. The pump powered by body heat produced a maximum pressure differential of 1.5 kPa. However, the use of these pumps is restricted to certain applications due to slow pumping. The polymer material, made of mixed cellulose ester, has a very low thermal conductivity, which aids in maintaining a higher temperature difference between the ends of a channel to achieve a higher flowrate. The polymer material used is in the form of a nanoporous template which has numerous pores each of which acts as a pump and thus the pump's conductance to gas flow is also increased which makes it faster. The pore sizes range from 25 nm to 1200 nm. It has been proven that a smaller channel diameter pump is more efficient. Efficiency decreases as the channel size approaches viscous flow regime.

The initial design used a resistive heater to actively heat one end of the channel and a heat sink was used to passively cool the other end of the channel. This design was ineffective in achieving a significant temperature difference for a decent flowrate with the materials like silicon and glass. The conventional Knudsen pump design using a porous polymer matrix as channel material attained a normalized maximum no load flowrate of $135 \mu\text{L}/\text{min}\cdot\text{cm}^2$ at 3.81 Watts of input power. This number is low compared to other

micropumps. This led to the use of a thermoelectric material, which could actively heat and cool the pump channel ends and provide a much higher temperature difference over the same channel length as compared to the conventional Knudsen pumps which used only active heating of the channel's hot side. The thermoelectric strategy also eliminates the need for a heat sink in the pump. This transforms the design to bi-directional modes of operation.

The first design using thermoelectrics is a lateral design in which the pump channels closer to the thermoelectric element developed a higher temperature difference across them compared to the channels away from the thermoelectric element. Thus, the thermoelectric energy was underutilized. Changing to the radial design made the pump more efficient compared to the lateral design since the thermoelectric energy was uniformly distributed on all the pump channels. The radial design also reduced air gap resistances and minimized energy losses which enhanced the output for the same input power. At an input power of 4.18 Watts it achieved a normalized no load flowrate of 408 $\mu\text{L}/\text{min}\cdot\text{cm}^2$. It also recorded a maximum normalized flowrate of 1.5 $\text{mL}/\text{min}\cdot\text{cm}^2$ while moving a drop of water which to date is the maximum flowrate reported by any Knudsen pump. A theoretical model has been developed to compute the pump's efficiency based on the flowrate and pressure difference obtained by the pump. The efficiency of the radial design pump with the thermoelectric is higher when compared to a conventional pump using a resistive heater whose channels are also made from the same material as that of the thermoelectric pump.

Finally, initial progress has been made for a Knudsen pump utilizing a porous thermoelectric. The nanoporous thermoelectric material would reduce the pump's size and lower the power consumption, which could help increase the efficiency of the pump.

TABLE OF CONTENTS	PAGE
ACKNOWLEDGEMENTS	iv
ABSTRACT	vi
LIST OF TABLES	xiii
LIST OF FIGURES	xiv
CHAPTER 1 - INTRODUCTION	1
1.1 MOTIVATION AND APPLICATIONS	1
1.2 MICROPUMPS	1
1.2.1 Types of micro pumps	2
1.3 SALIENT FEATURES OF THE KNUDSEN PUMP	7
1.4 RELEVANCE OF THE RESEARCH	8
1.5 OUTLINE OF THESIS	10
CHAPTER 2 - BACKGROUND AND PREVIOUS WORK	12
2.1 EXPERIMENTS WHICH LAID THE FOUNDATION	12
2.2 DIFFERENT PUMPS BASED ON THERMOMOLECULAR PHENOMENON OTHER THAN KNUDSEN PUMP:	13
2.2.1 Accomodation Pump	14
2.2.2 Thermomolecular pump	15
2.3 MODERN EXPERIMENTS	16
2.4 THEORETICAL WORK	22
2.5 APPLICATION OTHER THAN A PUMP	27
CHAPTER 3 - THEORY	28
3.1 THERMAL TRANSPARATION	28
3.1.1 Molecular flux theory of thermal transpiration	30
3.1.2 Momentum theory of thermal transpiration	33
3.2 THERMAL TRANSPARATION MODELS	34
3.2.1 Maxwell's Model	34
3.2.2 Kennard's Model	35

3.2.3 Williams' Model	36
3.2.4 Knudsen's Model	36
3.2.5 Sharipov's Model	37
3.3 KNUDSEN PUMP OR COMPRESSOR	40
3.4 THEORETICAL CALCULATION OF PRESSURE DROP ON THE COLD SIDE OF THE PUMP AS A FUNCTION OF TIME	42
3.5 THERMALLY DRIVEN FLOWS IN SUB-NANO/NANOSCALE SIZE CHANNELS	49
3.5.1 Nanoscale Pore Condensation	50
3.6 IMPROVEMENT OF PUMP EFFICIENCY	51
3.7 THERMOELECTRIC CONCEPT	52
3.8 PROPERTIES OF NANO STRUCTURED THERMOELECTRIC MATERIALS	55
CHAPTER 4 - UNIDIRECTIONAL KNUDSEN PUMP	58
4.1 LATERAL DESIGN MICROFABRICATED KNUDSEN PUMP.....	58
4.1.1 GLASS AND SILICON LATERAL MICRO-MACHINE PUMP.....	58
4.1.2 Silicon micro-machined pump.....	61
4.1.3 Polymer micromachined pump.....	68
4.2 GLASS MICRO-MACHINED MICROFLUIDIC PUMP	73
4.2.1 Fabrication process development	76
4.2.2 Results	79
4.3 THERMAL TRANSPIRATION IN POROUS POLYMER MEMBRANE.....	81
4.3.1 PRESSURE DIFFERENTIAL VERSUS PORE DIAMETER.....	82
CHAPTER 5 - KNUDSEN PUMP USING PASSIVE POWER	86
5.1 PUMP DESIGNS	86
5.2 TYPES OF MATERIALS USED IN POROUS MEMBRANES.....	87
5.3 TESTING OF PUMPS	88
CHAPTER 6 - THERMOELECTRIC POWERED BI-DIRECTIONAL KNUDSEN PUMP	90
6.1 LATERAL AND RADIAL PUMP DESIGNS	90
6.2 SIMULATIONS	95
6.2.1 Lateral Pump Simulation	96
6.2.2 Radial Pump Simulation.....	97
6.3 RESULTS.....	100
6.3.1 Pressure mode testing	100
6.3.2 Flow mode testing	102

6.5 PRESSURE-FLOW CHARACTERISTICS	103
6.5.1 Experimental analysis	103
6.7 EFFICIENCY OF THE PUMP	107
CHAPTER 7 - CURRENT PROGRESS USING NANOPOROUS THERMOELECTRIC AS KNUDSEN PUMP	111
7.1 NANOPOROUS THERMOELECTRIC	111
7.2 MERITS OF USING NANOPOROUS THERMOELECTRIC	111
7.3 NANOPOROUS THERMOELECTRIC MATERIALS	114
7.4 METHODS TO MAKE NANOPOROUS THERMOELECTRIC	114
7.4.1 Porous Si as a Pump	114
7.4.1.1 Formation of porous silicon	115
7.4.1.2 Pore Morphology	117
7.4.1.3 Porous Silicon membrane fabrication	118
7.4.1.4 Results	121
7.4.2 Hot pressing to make nanoporous Bismuth	124
7.4.3 MOCVD to make nanoporous Tellurium	127
7.5 RESULTS FROM HOT PRESS AND MOCVD METHODS	129
7.5 SINTERING OF DOPED BISMUTH TELLURIDE	132
CHAPTER 8 - CONCLUSION AND FUTURE WORK	135
8.1 CONCLUSION	135
8.2 FUTURE WORK	138
8.2.1 Sintering process	138
8.2.2 Sintered bismuth telluride porous pump	139
8.2.3 Results for the sintered pump	141
REFERENCES	144
APPENDIX A	154
CURRICULUM VITAE	156

LIST OF TABLES

Table 1. Various parameters with their numerical values used in computing theoretical results	47
Table 2. Results of the simulation.....	68
Table 3. Porosity and membrane thickness for the different pore diameters of mixed cellulose ester membranes	81
Table 4. Values of thermal conductivities used in the simulations.....	95
Table 5. Measured pressure difference obtained as a function of input power for the lateral pump	101
Table 6. Measured pressure difference obtained as a function of input power for the radial pump	101
Table 7. Porous silicon classification based on the pore diameter [IUPAC].....	117
Table 8. Nanoporous thermoelectric experimental results	129
Table 9. Table summarizing the major Knudsen pumps made to date highlighting their pumping characteristics	143

LIST OF FIGURES

<i>Figure 1. Schematic illustrating working principle of a micro pump.....</i>	1
<i>Figure 2. Graph showing pressure head and flowrate data obtained by different micropumps.</i>	2
<i>Figure 3. Experimental set up with which Knudsen showed thermal transpiration effect at sub atmospheric pressure.</i>	12
<i>Figure 4. Schematic of the accommodation pump. The walls of the pipe connecting A & C are rough while those of the pipe connecting B & C are smooth.</i>	14
<i>Figure 5. Schematic of a thermomolecular pump. The heated carbonized nickel element increases the molecular flux from A to B.</i>	15
<i>Figure 6. Schematic of the aerogel machined Knudsen compressor</i>	16
<i>Figure 7. Schematic of the nanoporous matrix made of glass spheres used for Knudsen pump</i>	18
<i>Figure 8. (a) Comparison of conductances derived from experimental data for 500 μm height rectangular channel and 500 μm diameter capillary membranes. (b) Comparison of experimental $\Delta p/ p_{\text{av}}$ for 500 μm height rectangular channel and 500 μm diameter capillary membranes.</i>	19
<i>Figure 9. (a) Optical micrograph of a single chip Knudsen pump, (b) 200 μm pressure sensor membrane before power is applied, (c) pressure sensor deflected after 80mW of power is applied.</i>	19
<i>Figure 10. a) Schematic & b) exploded views of the zeolite Knudsen pump.</i>	21
<i>Figure 11. a) Schematic & b) exploded views of the 9 stages ceramic Knudsen pump. ..</i>	22
<i>Figure 12. (a) Surface of the ideal efficiency as a function of T_{cold} and T_{hot}, for dry air and using equal hot and cold pressure, (b) Plot of efficiency vs. temperature ratio for dry air and using equal hot and cold pressure.</i>	24
<i>Figure 13. DSMC simulation domain for single membrane channel Knudsen compressor with hot and cold side connectors.</i>	25
<i>Figure 14. Temperature maps in DSMC simulations for uncoupled and coupled cases.</i>	25
<i>Figure 15. (a) Channel configuration, (b) wall temperature distribution, (c) Flow velocity and isothermal lines at $\text{Kn}=0.05$ and $T_1/T_0=3$, arrows showing direction of flow, (d) massflow rate for channel in (c).</i>	26

Figure 16. Schematic of capacitive cantilever assembly, (b) The stress induced by the KF on the cantilever results in a static deflection which is sensed as a variation in the capacitance between the cantilever and the fixed substrate.	27
Figure 17. The figure shows the directions of the thermal transpiration and pressure driven flows.	28
Figure 18. Graph showing different flow regimes classified according to their corresponding Knudsen number ranges.	29
Figure 19. The net flow of molecules from cold chamber to the hot chamber when connected by a narrow channel which permits gas flow in molecular regime.	30
Figure 20. Diagram illustrating the calculation of flux of molecules striking the wall surface A.	31
Figure 21. Diagram showing momentum transfer from gas to wall of the pump channel in thermal transpiration.	33
Figure 22. Flow coefficients against a range of Knudsen numbers for circular capillary.	38
Figure 23. Pressure distributions for 5 μm long channels comparing DSMC,	40
Figure 24. A two-stage Knudsen pump cascaded in series, showing resultant pressure change.	41
Figure 25. Theoretical pressure drop plotted as a function of time for 25 nm pore size membrane.	46
Figure 26. Theoretical flowrate with time is obtained by substituting the dynamic pressure (equation 3.59) on the cold side pressure in equation 3.41.	47
Figure 27. Theoretical plot of pump pressure difference with respect to flowrate by using the data obtained from Figures 25 & 26.	48
Figure 28. Figure in (a) shows one directional Knudsen pump with asymmetric design using a resistive heater and heat sink, while the figure in (b) shows a bidirectional pump with symmetric design by using a thermoelectric.	51
Figure 29. Schematic of a peltier cooler showing the flow of charge carriers in the thermoelectric material which leads to a hot and a cold side.	53
Figure 30. The three crucial parameters of a thermoelectric shown at the vertices of a triangle.	54
Figure 31. Many of the recent thermoelectric materials have attained a higher figure of merit in nano dimensional form compared to their bulk counterparts.	55
Figure 32. Density of states for 2D, 1D and 0D materials, the dotted line shows the density of states for a typical 3D material.	56
Figure 33. (a) Schematic of the lateral microfabricated pump, (b) Lateral channel pump without the top cover in between the cold chamber opening and the metal patterned heater (c) with enclosed channel, open at the heat source end and the cold end, bonded to the bottom substrate along the edges of the channel.	59

<i>Figure 34. Process flow for the lateral design microfabricated single channel pump with bottom substrate as silicon and top cover as glass.</i>	<i>59</i>
<i>Figure 35. Infra red camera image with chip (a) OFF, (b) ON</i>	<i>60</i>
<i>Figure 36. (a) Simulation to show that a serpentine heater structure will distribute uniform heat along the width of the channel, (b) experimentally fabricated suspended heater trace in silicon using SCREAM like process.</i>	<i>61</i>
<i>Figure 37. Optical microscope image of the actual silicon-silicon chip with suspended heaters for thermal isolation, (a) the bottom silicon substrate without the top cover showing heater elements, cold side opening and support pillars, (b) showing the top silicon substrate being bonded over the etched channel.</i>	<i>61</i>
<i>Figure 38. (a) The experimental set up used to test the pump chip. Power is provided to the heater pads on the chip through the probes and the cold end of the channel is coupled to a pressure sensor not shown in the figure(a). (b) the graph obtained with pressure drop at the cold end versus time</i>	<i>63</i>
<i>Figure 39. Fabrication process for the Si-Si lateral pump, separately showing the SCREAM like process.</i>	<i>64</i>
<i>Figure 40. Longitudinal temperature distribution along the channel (a) when both top and bottom substrates are 500 μm thick, (b) when both top and bottom substrates are 5 μm thick.</i>	<i>67</i>
<i>Figure 41. (a) Effect of temperature on deformation of polymers, (b) important stages in hot embossing.</i>	<i>69</i>
<i>Figure 42. (a) Process steps for forming enclosed nano channels using hot embossing, (b) surface roughness scan of the hot embossed surface using optical profilometer.</i>	<i>71</i>
<i>Figure 43. a) Process flow for making polyimide nano channels with aluminum as sacrificial layer, b) remains of aluminum in nanochannels after a week of etching.</i>	<i>72</i>
<i>Figure 44. Schematic of the glass microfluidic pump.</i>	<i>73</i>
<i>Figure 45. Variation of threshold temperature with micro reservoir depth.</i>	<i>76</i>
<i>Figure 46. (a) Fabrication process flow for the glass pump showing both the nano channel and the micro reservoir etches and then glass to glass bonding, (b) SEM image of the nano channel fabricated in (a).</i>	<i>77</i>
<i>Figure 47. Measured temperature along the channel under thermal transpiration.</i>	<i>79</i>
<i>Figure 48. (a) As expected, the water level in the micro channels did not rise, as the connected nano channels are not in the proximity of the hot iron tip. (b) Successful pumping of the water in the micro channels when the connecting nano channels are under thermal gradient.</i>	<i>80</i>
<i>Figure 49. (a) Schematic of the experimental set up to establish the effect of channel size on thermal transpiration, (b) actual photograph of the pump used.</i>	<i>82</i>
<i>Figure 50. Plot of pressure drop on the cold side of the pump versus time measured for different pore sized membranes at 3.75 Watts of heater power.</i>	<i>83</i>

Figure 51. Plot of slope of pressure drop on the cold side of the pump versus time measured for different pore sized membranes at 3.75 Watts of heater power.	85
Figure 52. (a) Schematic of solar powered Knudsen pump, (b) schematic of human power Knudsen pump.	86
Figure 53. (a) Schematic of the bidirectional Knudsen pump using the lateral design, and (b) manufacturing steps of (a).	91
Figure 54. (a) Exploded view of the bidirectional Knudsen pump using the radial design, and (b) manufacturing steps of (a).	92
Figure 55. SEM image of the 100 nm mixed cellulose ester membrane showing nanopores.	93
Figure 56. Photographs of the actual pumps – (a) lateral pump design, and (b) radial pump design.	94
Figure 57. Simulation output from CoventorWare showing the temperature distribution of the lateral pump design with a 1 mm thick nanoporous material layer.	97
Figure 58. Comparison of the temperature distribution along the top (line HH in figure 57) and bottom (line CC in figure 57) surfaces of the nanoporous material obtained by simulation. In (a), a 1 mm thick nanoporous material is used, and in (b), a 105 μm thick nanoporous material is used.	97
Figure 59. Simulation output from CoventorWare showing the temperature distribution of the radial pump design with a 105 micrometer thick nanoporous material layer. .	98
Figure 60. The simulated temperature distribution along the top (line HH' in Figure 59) and bottom (line CC' in Figure 59) surfaces of the nanoporous material for the radial design is plotted as a function of the radial distance from the center of the nanoporous material.	99
Figure 61. Pressure differential obtained at the cold end with (a) the lateral pump design, and (b) the radial pump design.	100
Figure 62. Graph showing the measured flow rate normalized to nanoporous material area as a function of the pump power consumption, for forward and reverse flow directions. (a) Lateral pump design, (b) Radial pump design.	102
Figure 63. Schematic of the experimental set up used to measure pressure difference as a function of flowrate at a constant power.	105
Figure 64. Pressure flow characteristics of (a) thermoelectric Knudsen pump, (b) Knudsen pump made out of a resistive heater.	106
Figure 65. Pump efficiency as a function of hot and cold side temperature ratios.	107
Figure 66. TMPD comparison of the thermoelectric radial design pump for channel size of 25 nm and 100 nm against working pressure.	109
Figure 67. Ratio of flow coefficients plotted against a range of Knudsen numbers.	110
Figure 68. Diagram illustrating thermal losses in the thermoelectric pump.	111
Figure 69. Schematic showing the working of a nanoporous thermoelectric Knudsen pump.	112

<i>Figure 70. Band diagram at the interface of the silicon and the electrolyte showing different energy levels that lead to the concept of formation of porous silicon.</i>	116
<i>Figure 71. Schematic of the set up with electrical connections and the silicon chip which is made porous by anodic etching.</i>	119
<i>Figure 72. Process flow for making porous silicon membranes.</i>	121
<i>Figure 73. (a) SEM image showing pore distribution and diameter on the front side where of the nanoporous silicon (b) pore distribution and diameter on the back side. Etching was done at 40 mA/cm² in 1:1:: HF:C₂H₅OH</i>	122
<i>Figure 74. (a) Cross section of silicon wafer etched in double cell etching bath at 60 mA/cm² in 1:1:1::HF:H₂O:C₂H₅OH for 30 minutes each side, (b) cross section of wafer etched in single cell etch bath using conditions of Figure 73.</i>	123
<i>Figure 75. Fabricated pump out of porous silicon with electrical connections shown in (a), optical microscope image of one side of the membrane showing metal contact made by ebeam evaporation shown in (b).</i>	123
<i>Figure 76. (a) Schematic of the hot press method. (b) The hot press equipment setup along with temperature controller.</i>	124
<i>Figure 77. (a) Schematic of arrangement of the spheres of silicon dioxide in the silica crystal, showing octagonal and tetrahedral voids and the interconnect between the voids as δ [92], (b) SEM image of the colloidal silica crystal showing the actual arrangement of spheres.</i>	125
<i>Figure 78. (a) Photograph of nanoporous bismuth obtained from hot pressing after the silica has been etched, (b) SEM image of the nanoporous bismuth showing the voids</i>	126
<i>Figure 79. Experimental set up used for MOCVD.</i>	127
<i>Figure 80. SEM image of a MOCVD tellurium sample (a) with silica, (b) after removing the silica.</i>	128
<i>Figure 81. Illustration showing thermopower measurement set up.</i>	130
<i>Figure 82. Schematic showing densification of stages in sintering process.</i>	134
<i>Figure 83. Sintering process flow.</i>	139
<i>Figure 84. Sintered nano porous thermoelectric pump with inlet and power connectors.</i>	140
<i>Figure 85. Pressure sensor connected to the pump measured the change in pressure at the cold side of the pump as against the ambient pressure in both modes of operation.</i>	141

CHAPTER 1 - INTRODUCTION

1.1 Motivation and Applications

The microgas pump forms an integral component in MEMS and microtechnology applications ranging from gas manipulation [1], forced convective cooling in microelectronics [2], space exploration, microplasma and gas chromatography [3], to microfluidic applications such as Lab-On-A-Chip [4], protein immunoassays, drug delivery and active micromixers [5]. Much progress has been made but a complete on chip micropump suitable for the above applications is not easily available. Thus, this research has a lot of potential.

1.2 Micropumps

A micro pump or compressor – The basic design of a micropump consists of a pumping cavity where the pumping takes place and an inlet and outlet connected to that cavity with control valves to regulate the fluid flow as shown in *Figure 1*. If a chamber of fluid is connected to the inlet of the pump by which it evacuates the gas or draws in the

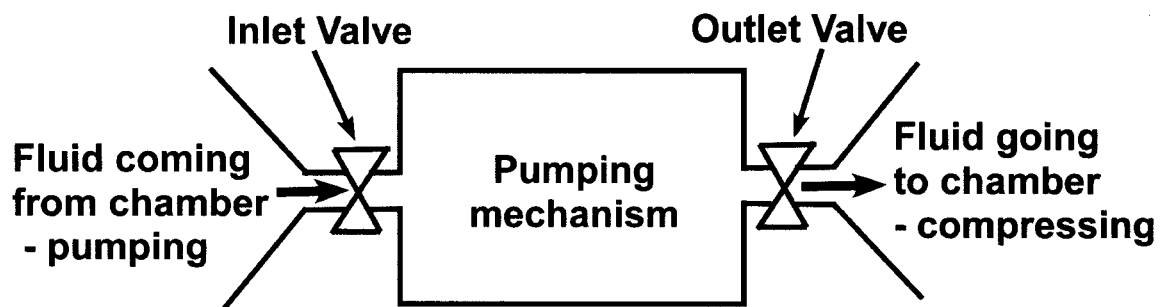


Figure 1. Schematic illustrating working principle of a micro pump.

liquid then it is termed as a pumping action whereas if the pump's outlet is connected to a chamber filled with gas or liquid which gets compressed due to pumping then it is termed as a compressor.

A brief overview of the common micro pumps with their working principle and merits and de-merits is classified below so as to figure out what could be improved in pumping criterion to make a better pump which is more versatile and overcomes the existing shortcomings.

The two main parameters which govern a pump are pressure difference generated and flowrate obtained which have been identified for the following types of pumps in *Figure 2*.

1.2.1 Types of micro pumps:

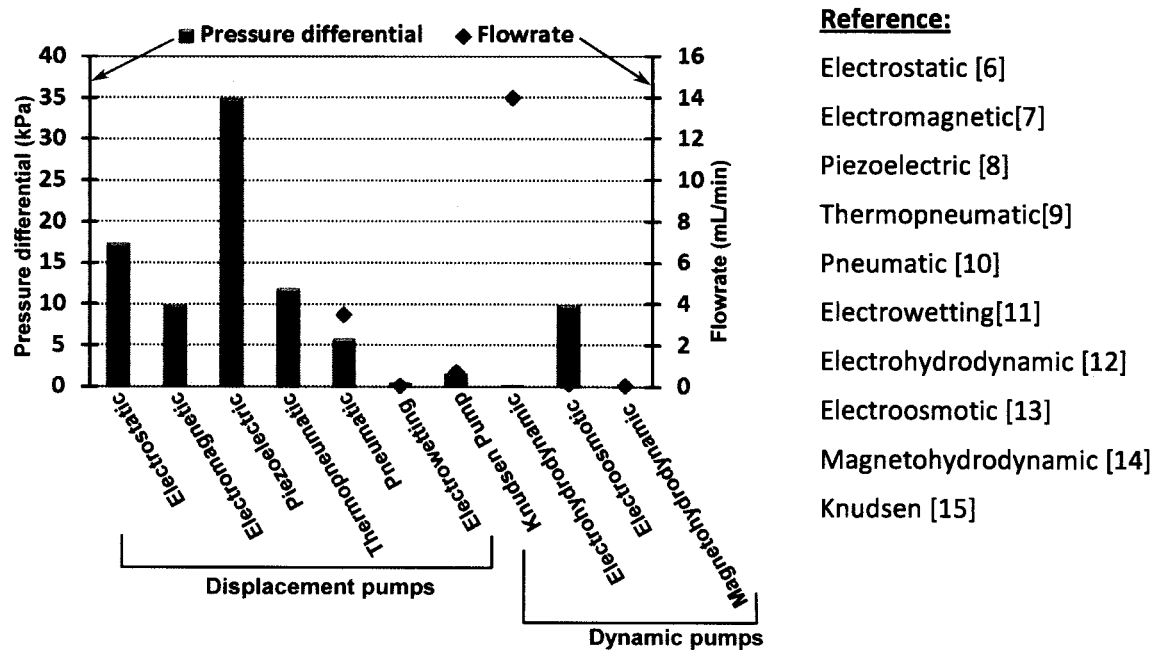


Figure 2. Graph showing pressure head and flowrate data obtained by different micropumps.

- A) Displacement pumps- Most of the micropumps reported so far are displacement micropumps. The membrane or the diaphragm is made to deflect by some actuation mechanism which compresses the fluid in the chamber and thus generates pressure by adding momentum to the fluid volume. The displacement in most cases is periodic and that periodicity is rectified into a continuous flow.
- 1) Electromagnetic – Electromagnetic actuation can be achieved by the movement of the plunger due to electromagnetic forces coupled to the solenoid coil. Since it is electromagnetic in nature the force on the plunger is proportional to the amount of current passing through the coil and the number of turns on the coil. Miniaturization is limited due to the bulky size of the solenoid coil. It's advantages are large bi-directional movement, larger volume displacement and response to a high frequency range. The force obtained reduces in the micro world due to decreased volume of magnets and turn coils. Power consumption is high since it needs larger magnitudes of current. The use of magnetic materials may interfere with fluids if they possess ferroelectric properties.
 - 2) Piezoelectric – This actuation is obtained by either bimorph or monomorph piezo elements which make use of the change in strain while actuated. The change in strain causes the membrane to deflect which is used to pump the fluid in the pump chamber. The elements could be either in the form of discs or cantilevers and could operate as a single element or in stacks of elements to increase the pressure generation. This is the most widely used in both micro and macro pumps due to its high frequency operation, precise control of motion and high stroke force. They can operate at 10 kHz

frequency regime with voltage range between 80V to 200V. The fabrication is in the complex side which makes it even harder to integrate in the system.

- 3) Electrostatic micropumps – This pump uses an electrostatic actuator in which there is one fixed electrode and another movable electrode separated by a gap. It can be easily fabricated in micro scale since a tiny gap is achievable by modern lithographic techniques, consume less power due to capacitive actuation compared to some other micropumps and is significantly fast. The disadvantage is that in the micro world friction and stiction forces on the moving electrode decrease the reliability of the pump. It also could be easily integrated with other electronics of the system due to a wide range of operable frequency.
- 4) Pneumatic micropumps – Pneumatic micropumps use external gas pressures to actuate the membrane controlled by a valve and an air compressor. The force generated has a wide operable range since an external gas pressure is used but simultaneously it becomes difficult to integrate in a system due to limitation in size reduction. The pumping system is also dependent on the response time of the valves.
- 5) Thermopneumatic pumps – Similar to the pneumatic pumps, thermopneumatic pumps work when a material used in the pump expands in volume due to heating and thus causes the deflection in the pump membrane. The membrane relaxes when the heat is transferred outside of the system. These pumps are characterized by large deflection and high force whereas the drawbacks include high response time which limits the flowrate and high power consumption due to resistive heating.

- 6) Electro wetting pumps- In this pump the fluid changes its surface gradient which moves the fluid. Pump can only work with liquids where charge redistribution can take place.
- B) Dynamic pumps –The dynamic pumps eliminate the limitation of stroke length as in the displacement pumps mentioned above since they operate by the interaction of the working fluid with the electric and magnetic fields and for a special category of pumps the interaction is temperature driven. Most of the dynamic pumps are used to pump liquids.
- 1) Electrohydrodynamic pump – The pumping is due to electrostatic forces interacting with ions in dielectric medium. Thus, these pumps can only be used with certain types of fluids. There are two different types of EHD pumps:
- a) DC injection type – The coulombic forces exerted on the charges between the pump electrodes with an applied electric field is the main pumping force. Electro chemical reaction between electrodes and the liquid which depends on the composition and geometry of electrodes determine the pump characteristics.
- b) Travelling wave voltage type –Phase shifted rectangular voltage pulses are applied in the direction of the channel. Due to temperature induced conductivity gradients, free charges are induced in the channel which interacts with the travelling field in the volume of the liquid and results in liquid movement.
- 2) Electro Osmotic pump – Electro-osmotic pumps use the motion of the ions in the liquid to generate the flow. They are easy to fabricate, simple to integrate and not limited by the pressure generation since they are independent of a membrane. The major

drawback is the bubble formation due to high voltage required for long channel flows.

The key parameters that dictate the performance of EO pumps are

- (i) the magnitude of the applied electric field and applied voltage,
- (ii) the cross-sectional dimensions of the structure in which flow is generated,
- (iii) the surface charge density of the solid surface that is in contact with the working liquid, and
- (iv) ion density and pH of the working fluid

2) Magnetohydrodynamic pumps – In these pumps current carrying ions impart a Lorentz force in the presence of a magnetic field to the liquid to induce the flow. The pump performance is limited by the magnetic flux strength achieved by micro magnets.

3) Knudsen Pump – This is a gas pump but it's dynamic in nature. It uses a temperature gradient along the pumping channel to generate the flow of the gases. The flux of molecules is higher on the cold side of the channel as compared to the hot side due to the physics of thermal transpiration and is only applicable to channels which permit gas flow in free molecular or transitional regime. Although high pressures could be obtained by increasing the temperature difference along the channel but due to the limitation of channel diameter since the flow has to be in free molecular regime (~100 nm) the pump has a low flowrate. This thesis will incorporate designs and methods to increase the flowrate and thus increase the overall efficiency of the pump.

Thermally driven gas pumps can be readily miniaturized and makes them suitable for use as a vacuum pump or compressor for MEMS applications. This thesis work

encompasses a novel method of making a thermally driven gas pump with no moving parts for potential applications ranging from mems to microfluidics and biomedical applications.

1.3 Salient features of the Knudsen pump

The key features of this pump are as follows:

- The absence of moving parts makes this pump robust, free from wear and tear which is common in MEMS pumps such as diaphragm pumps.
- Can generate a constant pressure drop and thus a continuous flowrate required for many critical biological process flows.
- Flow rate has an easily controlled, large dynamic range.
- Bi-directional flow control.
- Small size.
- It can operate at low voltages, unlike some other micropumps, such as the electro-osmotic pump [16].
- Devoid of valves to minimize leakage.
- Can be used to pneumatically pump liquids.

The potential applications of this pump could be in the following areas:

- ❖ Lab – on – Chip applications
- ❖ Drug delivery
- ❖ Biological immunoassays
- ❖ Electronic chip cooling
- ❖ MEMS compressor and vacuum pump
- ❖ Energy harvesting

- ❖ Bypass medical devices since its bidirectional [17].

The working principle of the micropump is based on the principle of thermal transpiration. Thermal transpiration based pumps are also known as Knudsen pumps after the name of the inventor of this pump – Martin Knudsen. Thermal transpiration states that a gas flow takes place from a cold chamber to a hot chamber both of which are connected by a channel which permits free molecular flow when a temperature difference is maintained along the length of the channel.

The key problems which surfaced during the making of the pump are:

- Isolation of the hot and cold ends over a small channel length to get the required pressure differential for successful operation of the pump.
- Obtaining a substantial flowrate.
- Integrating the pump to a sensor for further applications. Since, the heat from the hot end will affect both a pressure sensor and a flow sensor and give inaccurate measurements.

The above mentioned problems are approached in the following ways:

- ✓ The pump channel ends are heated and cooled by active means on the respective ends.
- ✓ A material of low thermal conductivity for the pump is found which helped in maintaining a greater temperature difference and along with it the design of multiple pump channels operating in parallel is implemented to increase the flowrate.
- ✓ Off-chip sensors are used for both pressure drop and flowrate measurements.

1.4 Relevance of the research

The pump in discussion working on the principle of thermal transpiration has achieved higher efficiency compared to other pumps operating on same principle. It is also made bi-directional which is a unique feature in thermal transpiration based pumps.

Knudsen pumps prior to this focused on only creating a temperature difference along the channel by active heating of the hot end of the channel and passive cooling of the cold end of the channel. In the present work a significant temperature difference has been generated along the channel by using a thermoelectric material to actively heat as well as cool the respective channel ends. This design could keep one end of the pump at even below room temperature while simultaneously heat the other end and thus increases the efficiency. The property of a thermoelectric material is such that with the change in the direction of current flow through it the hot and cold ends will also interchange, thus facilitating a bi-directional operation of the pump due to symmetrical design.

The advanced work incorporates improving the efficiency of the pump, making it smaller and more compact, reducing energy losses and increasing the thermoelectric figure of merit by using nanoporous thermoelectric material as compared to the bulk material presently being used. The nanopores also serve the purpose of multiple channels which permit gas flow in the free molecular regime, thus killing two birds with one stone. This eliminates device integration complexity by using the same material for thermoelectric and the pump channel as well and thus reduces energy loss in the connection between the pump channel and thermoelectric material in the present design. The nanoporous thermoelectric also aids in making the pump more suitable for onchip operation like LOC due to its reduced size and weight. Investigation is in progress to find the optimum device design for the porous thermoelectric pump.

1.5 Outline of thesis

The thesis starts with an introduction of the key features of this pump which make it a superior candidate over its competitors.

Chapter 2, “Background And Previous Work”, outlines all the successful endeavors towards attempting to make Knudsen pumps and compressors right from its inception in macro scale to the present micro scale Knudsen pumps which also includes theoretical research.

Chapter 3, on “Theory”, is broken into two parts. The first part talks about the kinetic theory of gases and the derivation leading to the thermal transpiration equations. The second part talks about the operation of a thermoelectric and how integration with the pump improves the pump performance and simultaneously makes it bi-directional in nature. It also briefly touches on the physics of nanostructured thermoelectrics since the future goal is to make a Knudsen pump out of nanoporous thermoelectric material.

Chapter 4, on “Unidirectional Knudsen Pump”, starts from the very first approach to make the pump using silicon in the lateral design and then throws light on why it failed and then moves onto making the microfluidic glass based Knudsen pump which works better than the silicon based Knudsen pump.

Chapter 5, on “Knudsen Pump Using Passive Power”, discusses how body temperature and solar energy could be used to drive thermal transpiration in nano porous material.

Chapter 6, on “Thermoelectric Powered Bi-Directional Knudsen Pump”, uses a polymer based porous material coupled with a thermoelectric to make the pump bi-directional as

well as more efficient. Pressure and flow characterization is also included which points out why the thermoelectric is so essential for a better pump.

Chapter 7, on “Current Progress Using Nanoporous Thermoelectric As Knudsen Pump”, the features of a nanoporous thermoelectric is outlined and various methods have been discussed which are tested to make a porous thermoelectric Knudsen pump.

The thesis concludes with the “Conclusion and Future Work” which summarizes the various efforts towards making a more efficient Knudsen pump and the ongoing work in progress with nanoporous thermoelectric and its future goals.

CHAPTER 2 – BACKGROUND AND PREVIOUS WORK

2.1 Experiments which laid the foundation

Osborne Reynolds was the first person to realize the phenomenon of a flow creeping from cold to hot side and he coined the term thermal transpiration [18]. During the same time, Maxwell developed independently a theory for thermal creep [19]. In 1910, Martin Knudsen built the first thermal transpiration based molecular compressor. The molecular compressor built by Knudsen [20, 21] consists of a series of tubes with constrictions arranged in between each tube. The constrictions were very small so that rarefaction effects became important in the constrictions shown in *Figure 3*. By heating the same side of these constrictions to a very high temperature of 773K, Knudsen was able to maintain considerable pressure gradients.

In another experiment Knudsen [22] used artificially porous porcelain bulb. The

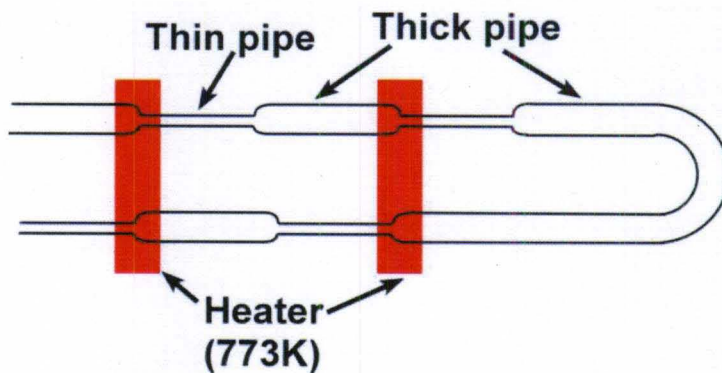


Figure 3. Experimental set up with which Knudsen showed thermal transpiration effect at sub atmospheric pressure.

air inside the bulb is heated by passing an electric current through a resistance. At steady state the inner surface of the bulb is hotter than the outer surface. A tube connected to the bulb had its other end dipped in water. Due to thermal transpiration cold air from outside came through the pores inside the bulb and augmented the air pressure which in turn formed bubbles in the water at the end of the tube. Because of the backflow mentioned in Chapter 3 the pressure difference between the inside and outside of the bulb becomes smaller.

Significant work has been carried out by various research groups in the area of thermal transpiration based pumps in micro and macro scale involving both theory and experiments.

2.2 Different pumps based on thermomolecular phenomenon other than Knudsen pump:

Two other types of thermal molecular pumps are the accommodation pump and the thermomolecular pumps. They are briefly described in the next two subsections.

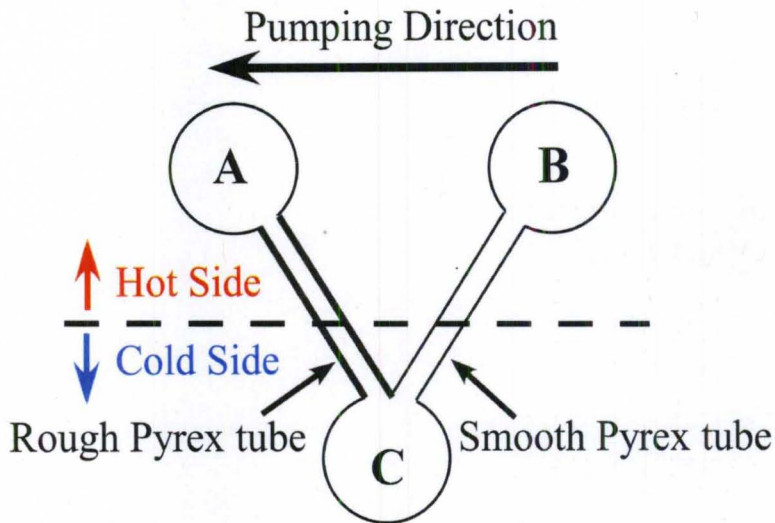


Figure 4. Schematic of the accommodation pump. The walls of the pipe connecting A & C are rough while those of the pipe connecting B & C are smooth. (Adapted from [23])

2.2.1 Accommodation Pump

The accommodation pump exploits the difference in the scattering of gas molecules at different types of boundary surfaces to generate the pumping action[23]. Two volumes of gas are connected by a channel which has alternating smooth and rough surfaces. When this set up is held at a temperature other than the room temperature then pumping of gas takes place from one volume to another. The explanation is attributed to the differences in specular reflection between hot molecules travelling toward the cold regions as compared with the cold molecules traveling toward the hot region. The specular reflection for both hot and cold molecules is suppressed by the surface roughness. *Figure 4* shows three chambers (A, B, and C) connected in series by tubes. Chambers A and B are connected through a smooth pyrex tube and chambers B and C are connected through a roughened pyrex tube. Hobson, in his experiments, demonstrated that if A and C are maintained at room temperature and B is held at liquid nitrogen temperature (that is, temperature lower than that of A and C), an effective movement of

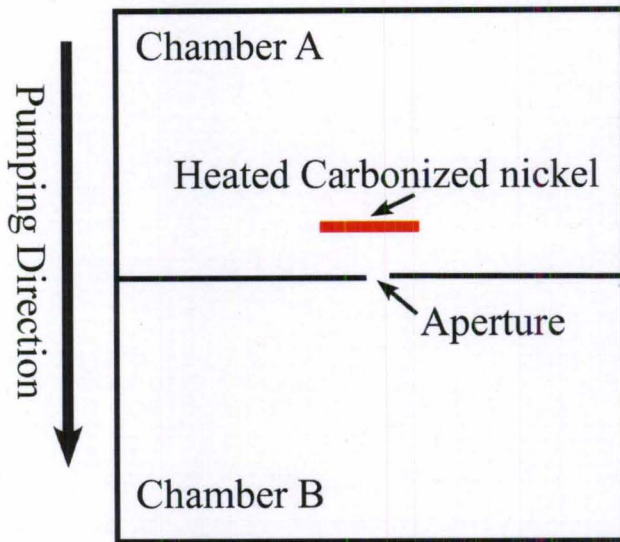


Figure 5. Schematic of a thermomolecular pump. The heated carbonized nickel element increases the molecular flux from A to B. (Adapted from [24])

gas molecules from A to C occurs. The difference in the gas-wall collision dynamics of the gas molecules moving through the smooth pyrex tube and through the roughened pyrex tube results in this pumping effect from chamber A to C. At equilibrium the ratio of the pressure in chamber A to the pressure in chamber B, P_A/P_B , is expected to be lower than the ratio of the pressure in chamber C to the pressure in chamber B, P_C/P_B .

2.2.2 Thermomolecular pump

Thermomolecular pumps work when in a non-isothermal system scattering of molecules from the wall surface do not follow cosine law which leads to anisotropic molecular fluxes, even though the molecular flux is isotropic and maxwellian [24]. In the experimental setup (Figure 5), there are two chambers connected by an aperture, maintained at same temperature T_0 , with chamber A having the director made up of carbonized nickel. If the director is heated to a temperature $T > T_0$, the molecular flux from A to B, Q_{AB} increases. The molecules which strike the director are preferentially

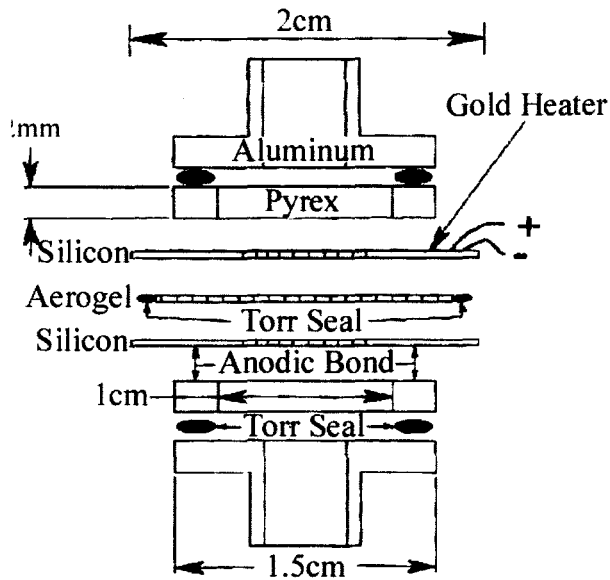


Figure 6. Schematic of the aerogel machined Knudsen compressor. (figure from [49])

scattered towards the normal and through the aperture. The angular distribution of molecules reflected off the face of the director is no longer cosine but is peaked somewhat more like Cos^2 reflection. The pressure in B is thus increased in equilibrium at which the molecular fluxes Q_{AB} and Q_{BA} are equal. The pressure ratio P_A/P_B is independent of the volume of the two chambers and is dependent on the angular distributions of molecular scattering at the surfaces, and on the geometrical arrangement of those surfaces.

2.3 Modern Experiments

Pham-Van-Diep [25] was the first one to demonstrate a (MEMS) Knudsen compressor. The compressor generated a large difference in pressure by employing a cascade of multiple stages. Each stage composed of a capillary and a connector. A temperature difference along the capillary results in pumping due to thermal transpiration

which creates a pressure difference. Vargo et al in the University of South California along with the Jet propulsion laboratory made a Knudsen compressor out of porous silica aerogels [26] extending the prior work in [26]. The aerogels have low thermal conductivity (0.02 W/mK) and the pore sizes in 10's of nm range permit gas flow in free molecular region both of which are favorable for thermal transpiration in room pressure conditions. The aerogel Knudsen pump achieved a pressure drop of 1.5kPa.

The low thermal conductivity offers the advantage of maintaining a temperature difference across the membrane with minimum energy consumption. A thin disc of silicon aerogel is used as the thermal transpiration membrane whose edges are sealed by Torr Seal epoxy. The aerogel is sandwiched between two silicon guards, with deep reactive ion etching (DRIE) holes through them. One of the thermal guards has a thin film resistive heater deposited on it. This forms the heat source of the hot end of the channel. The silicon thermal guards are anodically bonded to pyrex connector sections. The plexiglass cover and the aluminum base together constitute the connector section of the pump as shown in *Figure 6*.

If the silica aerogel is doped with carbon it can absorb radiant energy and Young et al made a radiantly driven Knudsen pump out of the aerogel by doping it with carbon [27]. They also tried a bed of glass spheres touching each other (shown in *Figure 7*) as transpirational membrane whose thermal conductivity is similar to that of the aerogels. Glass microspheres with diameters 0.75 mm and 0.344 μm are chosen as optimal pore diameters for the low pressure and high pressure cases, respectively. The spheres are blackened to minimize the radiation component of the thermal conductivity.

Han et al also made Knudsen compressor out of aerogel material operating at low pressures [28]. At low pressures the pore diameter of the aerogel can be as large as 500 μm for an operating pressure of 1 Pa. This dimension is easy to machine and also a higher conductance can be realized. Two different geometries of channels were used – capillary and rectangular.

The rectangular channel has three times more open area than the capillary channel. The membrane conductance is proportional to the membrane open area. In *Figure 8(b)*, the comparison of the maximum pressure ratios between the rectangular channel membrane (500 μm height) and the capillary membrane (500 μm diameter) indicates that the pressure ratios obtained by the capillary membrane were higher (1.8–3 times) than those obtained by the rectangular channel membrane. Theoretically, the pressure gain through the membrane channels is proportional to the flow coefficient ratio, Q_T/Q_P or M_T/M_P , for the same value of κ .

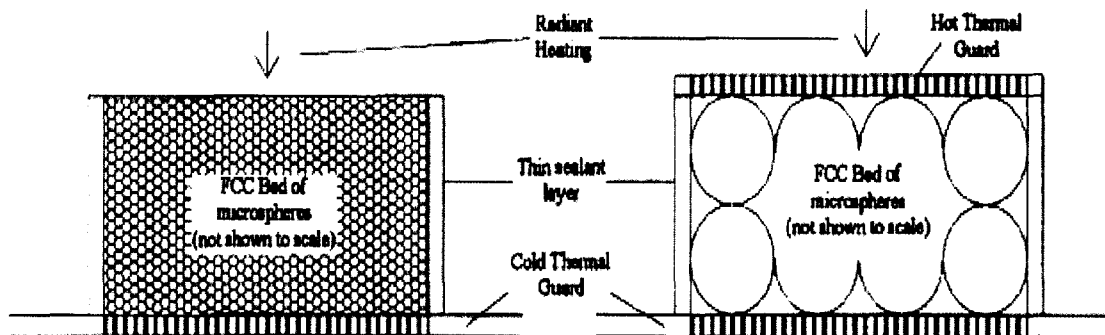


Figure 7. Schematic of the nanoporous matrix made of glass spheres used for Knudsen pump. (figure from PhD. Dissertation “Investigation of several important phenomena associated with the development of Knudsen compressors” by Marcus Young, USC, 2004)

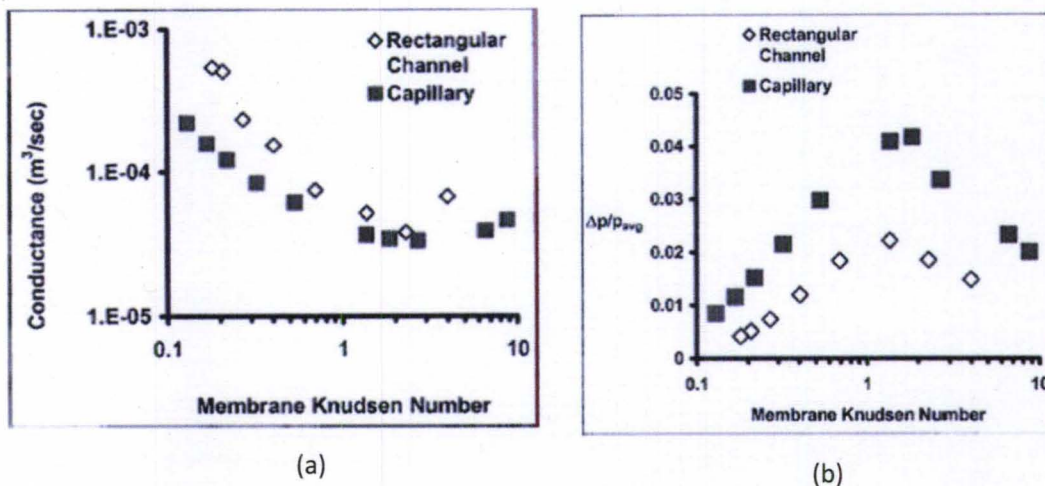


Figure 8. (a) Comparison of conductances derived from experimental data for 500 μm height rectangular channel and 500 μm diameter capillary membranes. (b) Comparison of experimental $\Delta p/p_{avg}$ for 500 μm height rectangular channel and 500 μm diameter capillary membranes. (figure from [28])

McNamara et al in the University of Michigan demonstrated the first fully microfabricated single chip Knudsen pump [29]. This pump is complete with integrated bolometers and capacitive pressure sensors for temperature and pressure characterization shown in Figure 9. This device is fabricated by separately processing a glass substrate and a silicon substrate, bonding them together, and dissolving the silicon handle wafer,

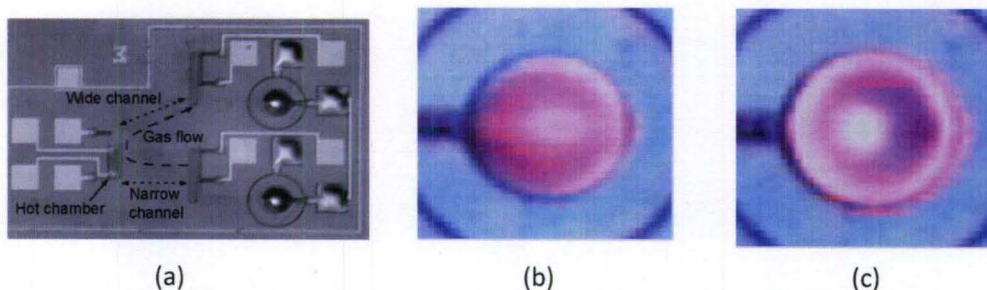


Figure 9. (a) Optical micrograph of a single chip Knudsen pump, (b) 200 μm pressure sensor membrane before power is applied, (c) pressure sensor deflected after 80mW of power is applied. The cavity pressure is measured to be 0.46 atm. (figure from [29])

leaving the pump on top of the glass substrate. The glass substrate and dielectric cover is used to minimize thermal losses. The microfabrication process is mostly on a planar surface, which facilitates other devices to be co-fabricated on the same wafer. The cold chambers are passively maintained at room temperature. A polysilicon heater located near the nano channels heats the hot chamber. The heater is suspended on a thin dielectric membrane in order to minimize heat flow from the heater to the substrate. This has achieved thermal isolation values greater than 1000 K/W. A glass substrate is used to provide thermal insulation and, thereby, improve the energy efficiency. A long channel length is used to improve thermal isolation between the hot and cold chambers. Thin film bolometers are located on the bottom of every chamber, measuring the temperature distribution and thus the degree of thermal isolation. With 35 mW of power, the cold chamber temperature increases by less than 1°C. The gas outlet of this Knudsen pump is vented to atmosphere. The high pressure drop can be observed by watching the deflection of the vacuum cavity pressure sensor (*Figure 9c*). The pressure sensor membrane is flat with no power to the Knudsen pump (*Figure 9b*), but it is deflected with the power on (*Figure 9c*). The change in capacitance measured is 2.6 fF, which corresponds to a cold chamber pressure of 0.46 atm. The input power of 80 mW provides the heater temperature of 1100 C. Based upon a visibly observed pump down time of two seconds; the mass flow rate is estimated to be $1 \times 10^{-6} \text{ cm}^3/\text{min}$.

Also, from University of Michigan, recently a Knudsen pump based on zeolite [30] was demonstrated with a flowrate of 0.12 sccm. Naturally occurring Clinoptilolite has nanoporous network structure which can be used for thermal transpiration. The zeolite material is cut in circular discs and one side is heated by means of a resistive heater and

the other side is left to attain room temperature with the help of a heat sink (*Figure 10*). Inlet pipes are attached to hot and cold ends and pressure drop and flow rate are successfully monitored. The pressure sensor attached to the cold side of the pump measured a maximum of 2.5 kPa. Flow rate is measured by using a water droplet on the hot end inlet of the pump. When the pump starts the water drop moves out of the pump and its velocity is recorded and thus flowrate is obtained. In this operation the hot side temperature is 50K above the room temperature and the cold side temperature is 17K above the room temperature.

Gupta et al also made a series cascaded Knudsen pump made of porous ceramic discs [31]. The pump is a 9 stage planar architecture providing a maximum pressure of 12kPa and a gas flow rate of 3.8 $\mu\text{L}/\text{min}$. Each ceramic disc is 2.85 mm thick and 5 mm in diameter. Brass caps with embedded microgroove channels are used to seal each ceramic disc from above and below, and direct the gas flow laterally, into/out of each

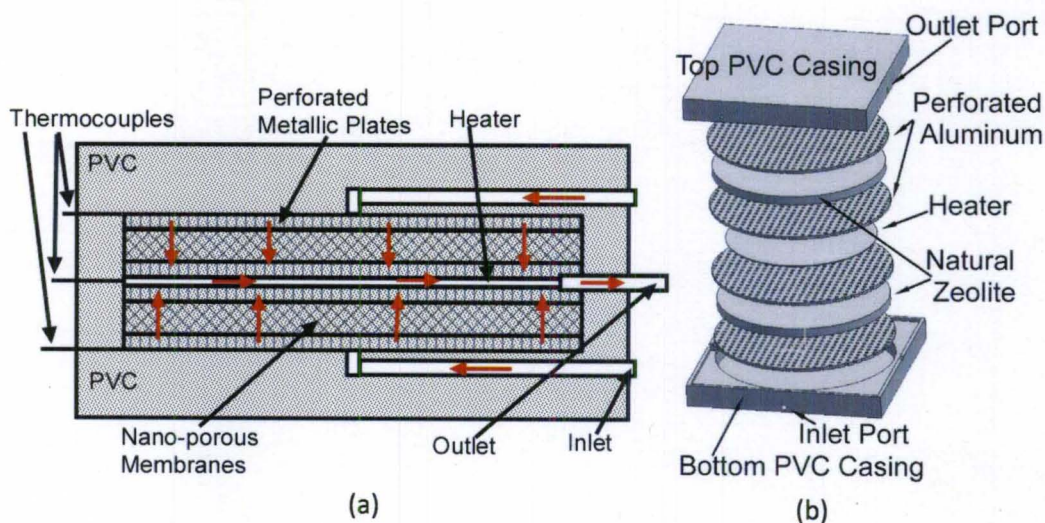


Figure 10. a) Schematic & b) exploded views of the zeolite Knudsen pump (figure from [30]).

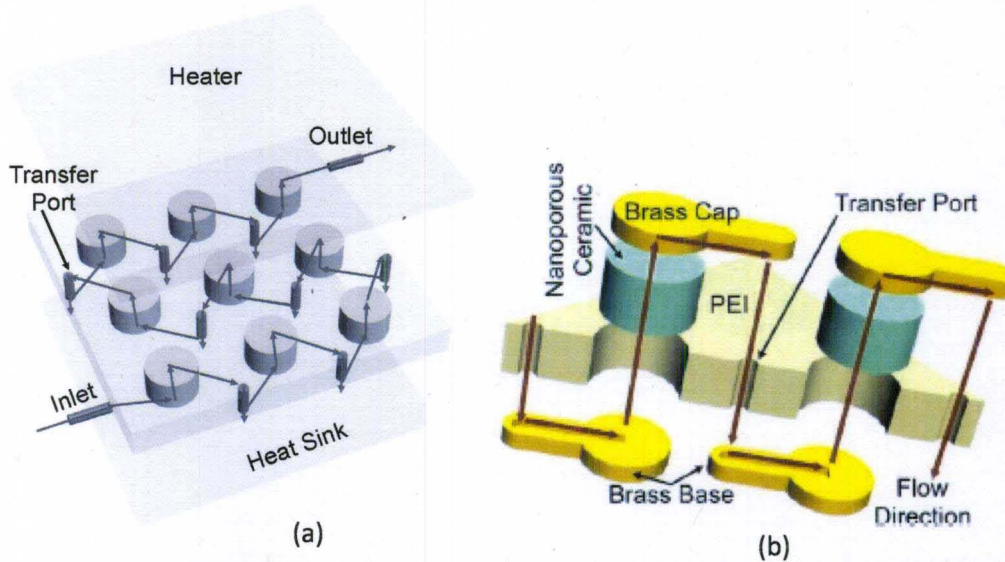


Figure 11. a) Schematic & b) exploded views of the 9 stages ceramic Knudsen pump. (figure from [31])

stage through the transfer ports (Figure 11). Thermally conducting caps minimize the possibility of parasitic heating of the transpiration elements.

2.4 Theoretical work

An extensive amount of theoretical work also has been done in the field of kinetic theory of gases related thermal transpiration and Knudsen pump. Davor et al [32] from our group calculated the theoretical efficiency of the pump with and without the thermal losses. In this derivation the flux from each side is considered as a separate pump. The efficiency is calculated in terms of power exerted by a unit of mass to flow or work exerted per unit mass, using

$$\eta_{ideal} = \frac{\dot{W}_{uesful}/\dot{m}}{\dot{W}_{input}/\dot{m}} \quad (2.1)$$

where \dot{W}_{input} is the input work usually in the form of input power from an external source like a power supply, solar power or waste heat.

$$\dot{W}_{useful} = \dot{W}_{hot} - \dot{W}_{cold} \quad (2.2)$$

where \dot{W}_{hot} is the work done by the hot flux and \dot{W}_{cold} is the work done by the cold flux. According to the formula a higher temperature on the hot side and a lower temperature on the cold side will increase the net effective \dot{W}_{useful} . After all the substitutions and neglecting thermal losses (*Figure 12*)

$$\eta_{ideal} = \frac{R}{C_p} \left(\frac{\Gamma_{cold} - \Gamma_{hot}}{\Gamma_{hot} + \Gamma_{cold}} \right) \quad (2.3)$$

where R is the universal gas constant and C_p is the specific heat of the gas. Thus different gases will have different efficiencies due to different specific heats.

Taking into account the thermal losses, using the conductance model of the pump channel the efficiency formula modifies to the following:

$$\eta = \frac{R}{C_p} \left(\frac{\frac{\sqrt{T_{hot}} P_{hot}}{\sqrt{T_{cold}} P_{cold}}}{\frac{P_{hot}}{P_{cold}} + \frac{\sqrt{T_{hot}}}{\sqrt{T_{cold}}} + (\sqrt{2\pi T_{hot}} \frac{R}{C_p} \frac{2l M G}{P_{cold}})} \right) \quad (2.4)$$

Here, $C' = \iint_{-\pi/2}^{\pi/2} \frac{1}{2} z \cos \theta d\theta ds$

where z is the chord making an angle θ with the normal to the perimeter s , G is a term used to lump together the energy losses to the environment, M is the molar mass of the gas being pumped and l is the length of the channel.

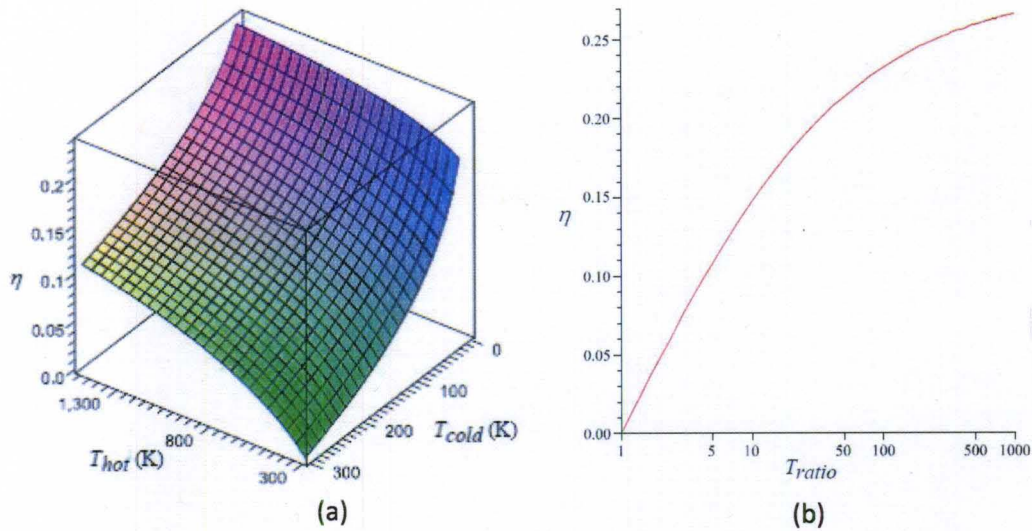


Figure 12. (a) Surface of the ideal efficiency as a function of T_{cold} and T_{hot} for dry air and using equal hot and cold pressure, (b) Plot of efficiency vs. temperature ratio for dry air and using equal hot and cold pressure. (figure from [32])

2.4.1 Simulation

DSMC – Discrete Simulation Monte Carlo simulations have also been carried in the field of thermal transpiration to fit the experimental data with theoretical model [33-35]. A real gas is modeled by a large number of simulated molecules. Each simulated molecule represents a fixed a number of real molecules. The simulation domain of the flow field is divided into small cells. Simulated molecules are indexed corresponding to the cells they occupy. Flow channels are represented by 2D straight channels in the simulations. In the 2D DSMC model, the velocity vectors retain 3D characteristics for the purpose of calculating the result of collisions.

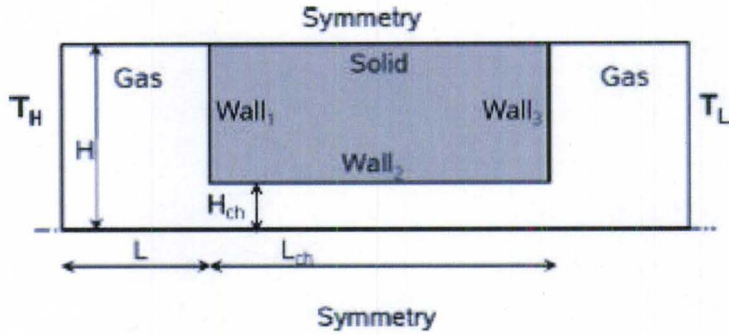


Figure 13. DSMC simulation domain for single membrane channel Knudsen compressor with hot and cold side connectors. Due to symmetry only half of the geometry is used. (figure from [33])

The 2D single membrane flow domain used in the simulations is as follows: A smaller channel (dimensions L_{ch} , H_{ch}) representing a single low-pressure membrane flow channel is placed between two larger channels (dimensions L, H), which are the cold and hot side connector sections on each side of the membrane (Figure 13).

For each time step, simulated molecules move and collide with each other or with solid boundaries; therefore, the two position components and three velocity components change accordingly. The flow properties including the number density, static temperature, and static pressure of the flow are calculated by averaging these components

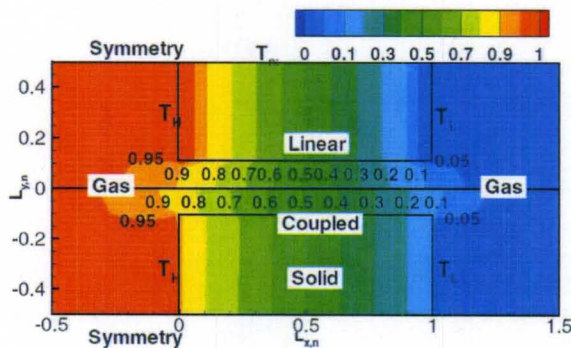


Figure 14. Temperature maps in DSMC simulations for uncoupled and coupled cases. $T_n = (T - T_L) / (T_H - T_L)$. (figure from [34])

over a certain large number of time steps (sample time) in each cell.

The thermal simulation in the *Figure 14* shows both coupled and linear models which differ significantly. The actual temperature difference of thermal transpiration in the coupled case is less in the channel compared to that of the reservoirs (*Figure 14*). This shows that a continuum description of thermal transport is not valid in the solid and that thermal contact resistance needs to be considered. The simulations also show that pressure driven flow is stronger than thermal transpiration flow at the centerline of the channel.

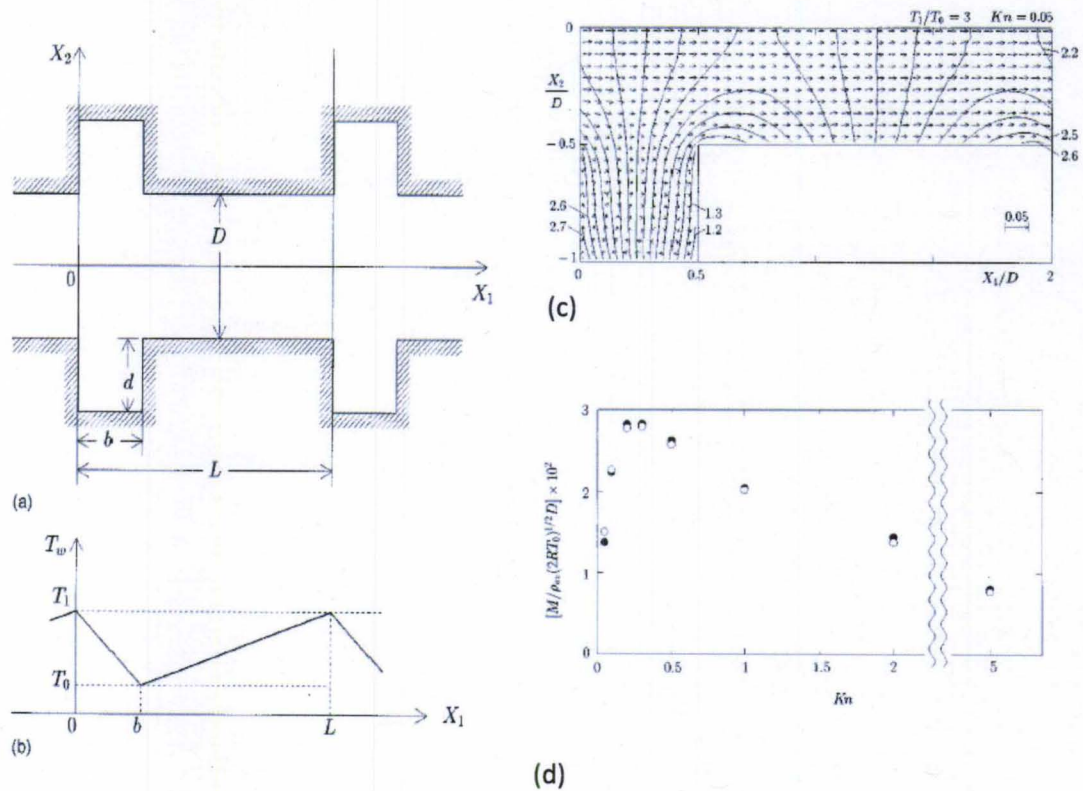


Figure 15. (a) Channel configuration, (b) wall temperature distribution, (c) Flow velocity and isothermal lines at $Kn=0.05$ and $T_1/T_0=3$, arrows showing direction of flow, (d) massflow rate for channel in (c). The white circle indicates the result computed with cell size $D/40 \times D/40$ and average number of particles per cell 100, and the black circle indicates that with $D/20 \times D/20$ and 100 [36].

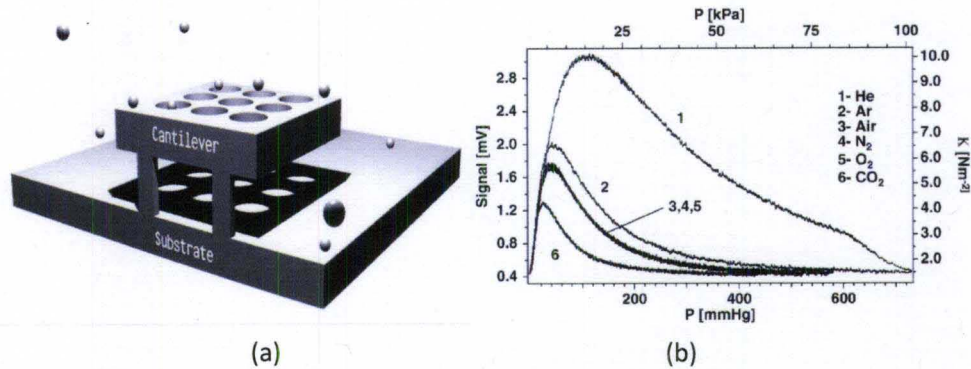


Figure 16. Schematic of capacitive cantilever assembly, (b) The stress induced by the KF on the cantilever results in a static deflection which is sensed as a variation in the capacitance between the cantilever and the fixed substrate. The left axis displays the measured signal, while the right axis gives the corresponding Knudsen pressure yielding a total force in the range $90 \text{ nN} \leq KF \leq 0.8 \text{ }\mu\text{N}$ for the cantilever used. (figure from [37])

Sone et al designed a channel with periodic grooves on both walls of the channel [36]. They imposed a periodic temperature variation, whereby the temperature decays linearly on the groove side but it increases linearly on the channel wall (Figure 15 (a&b)). This device produced a unidirectional flow with a maximum mass flow rate at $\text{Kn} \sim 0.3$.

2.5 Application other than a pump

Based on the principle of thermal transpiration, sensors have also been designed and fabricated [37]. Knudsen like forces is generated when gas or air is passed through an opening whose dimension allows for a free molecular or transition regime flow (Figure 16(a)). The pressure dependence of these forces has been studied using a microelectromechanical system composed of a microcantilever near a substrate surface. Nano-Newton scale KF is observed by the bending of the microcantilever as monitored by the charge variation on the microcantilever-substrate assembly in a capacitive mode.

CHAPTER 3 - THEORY

3.1 Thermal Transpiration

In a Poiseuille flow the velocity of flow at the walls of a channel is zero. But when the mean free path of the molecules approach the hydraulic diameter of the flow channel then this law fails since the flow velocity at the walls is greater than zero or rather the gas appears to slip as shown in *Figure 17*. Thermal transpiration is one such phenomenon which occurs in rarefied gases.

To understand the physics of thermal transpiration certain physical terms need to be explained. Flows can be categorized based on a dimensionless number called Knudsen number. Knudsen number ' K_n ' is defined as the ratio of the mean free path of the gas molecules ' λ ' to that of the hydraulic diameter ' d ' of the channel in which the flow is taking place. $K_n = \frac{\lambda}{d}$. where $\lambda = \frac{1}{\sqrt{2}\pi D_m^2 \left(\frac{\rho}{m}\right)} = \frac{TR}{\sqrt{2}\pi D_m^2 P}$ (3.1)

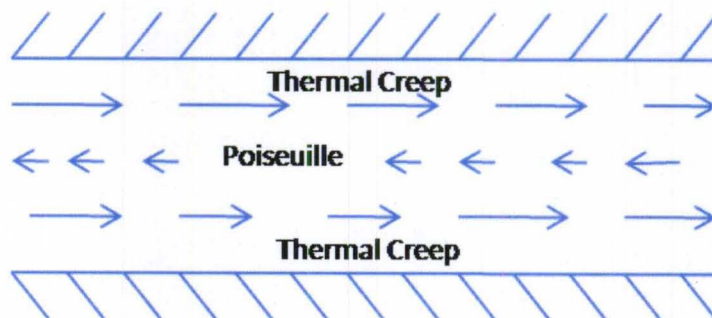


Figure 17. The figure shows the directions of the thermal transpiration and pressure driven flows.

ρ is the density, m is the molecular mass, and D_m is the radius of the influence range of the intermolecular force. Based on this formula and knowledge from kinetic theory of gases, it becomes apparent that the mean free path is directly proportional to temperature and inversely proportional to pressure. Here, R is the universal gas constant, T is the absolute temperature and P is the pressure of the gas. Thus, the Knudsen number can be increased by increasing the density or the pressure of the gas, or by decreasing the temperature of the gas.

Flow regimes have been categorized based on different ranges of Knudsen numbers (Kn) as shown in *Figure 18*: continuum flow $Kn < 0.01$, slip flow $0.01 < Kn < 0.1$,

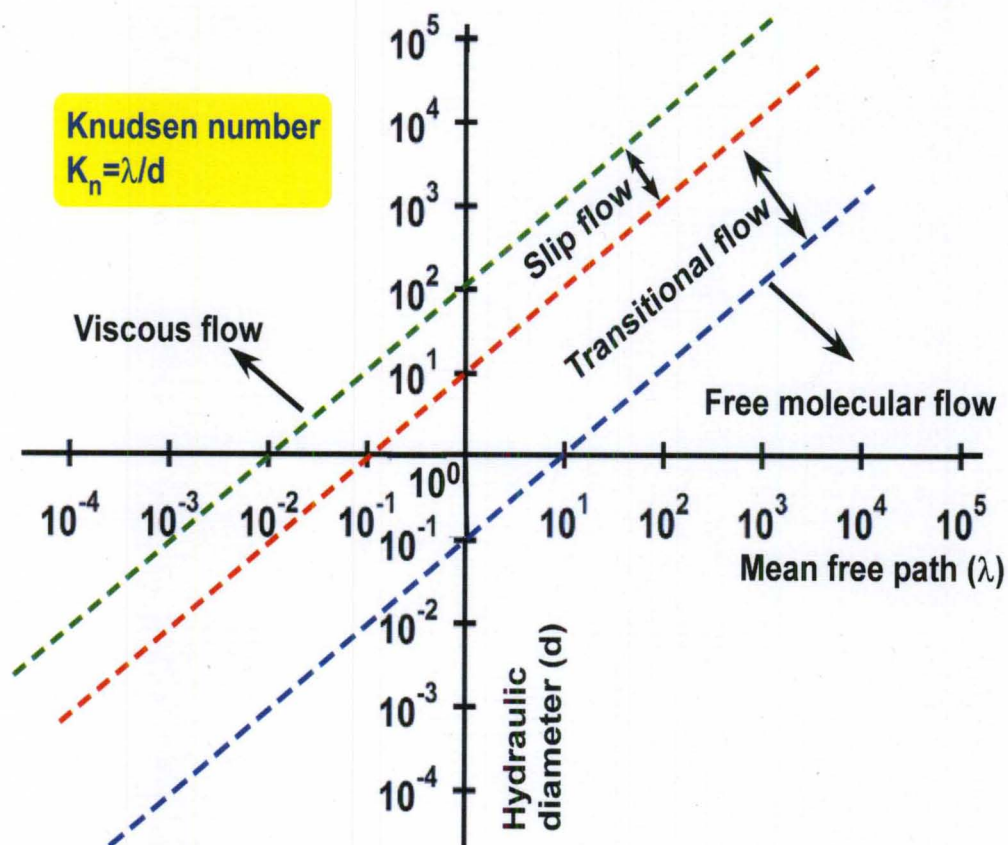


Figure 18. Graph showing different flow regimes classified according to their corresponding Knudsen number ranges. (figure adapted from [38])

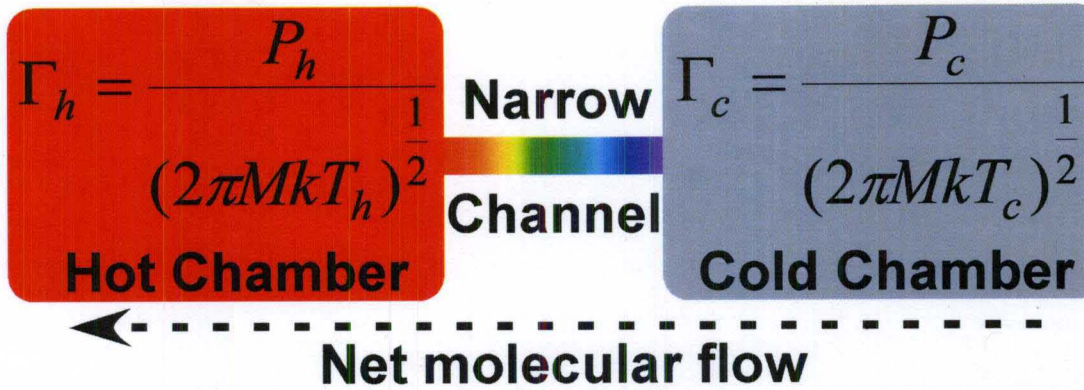


Figure 19. The net flow of molecules from cold chamber to the hot chamber when connected by a narrow channel which permits gas flow in molecular regime.

transition flow $0.1 < Kn < 10$, and free molecular flow $Kn > 10$. The formula of Knudsen number in the various regimes of gas flows assumes air at isothermal temperature of 273K. Thermal transpiration has been observed in both the transition and the free molecular flow regimes [38].

3.1.1 Molecular flux theory of thermal transpiration

If two vessels are filled with gas at atmospheric pressures but at different temperatures $T_1(T_h)$ and $T_2(T_c)$, and they are connected by a channel whose diameter is larger or comparable to the mean free path of the gas molecules (shown in Figure 19) then the following condition prevails:

$$\frac{P_1}{P_2} = \sqrt{\frac{T_1}{T_2}} \quad (3.2)$$

In a gas at rest which follows a Maxwell-Boltzmann distribution for the molecular velocities, molecular flux ' $d\phi$ ' across a plane surface element 'A' is given by the cosine law [39]:

$$d\phi = nA \frac{d\omega}{4\pi} \int_0^\infty v \cos\theta \cdot f(v) dv = nA \bar{v} \cos\theta \cdot \left(\frac{d\omega}{4\pi}\right) \quad (3.3)$$

Here, 'n' is the number of particles per unit volume, 'f(v)' is the Maxwell-Boltzmann velocity distribution function. All molecules within the solid angle 'dω' have velocity vectors 'v' whose axis makes an angle θ with normal to A (Figure 20) . 'v̄' is the average molecular velocity which is calculated as $\bar{v} = \frac{1}{n} \int_0^{\infty} v f(v) dv = \sqrt{\frac{8kT}{\pi m}}$.

Consider only those molecules which strike a plane solid or liquid surface and are not scattered backward, then the total molecular flux across or against this surface is

$$\phi = nA \int \cos\theta \cdot d\omega / 4\pi \quad (3.4)$$

$$\begin{aligned} &= nA \bar{v} \int_0^{2\pi} \int_0^{\pi/2} \cos\theta \sin\theta \, d\theta \, d\phi / 4\pi \\ &= \frac{n \bar{v}}{4} A \end{aligned} \quad (3.5)$$

Depending on the surface roughness and the intermolecular forces during the collision, some molecules are striking the solid surface are adsorbed while the remainder are scattered back in various directions.

The adsorbed molecules eventually reach accommodation with the prevailing temperature of the material at the surface. Under equilibrium conditions the sum of the distribution of the molecules leaving the surface due to various processes (adsorption-

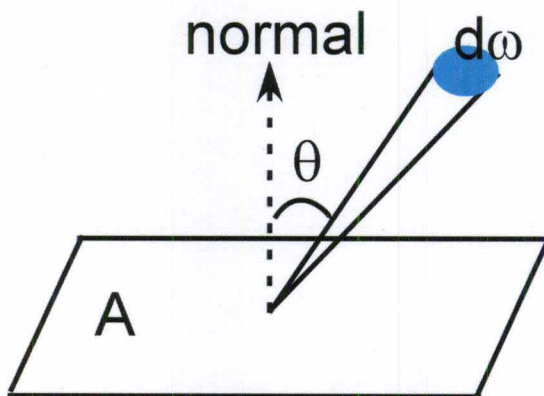


Figure 20. Diagram illustrating the calculation of flux of molecules striking the wall surface A. dw is the solid angle in the cosine formula.

desorption, reflection, diffraction and inelastic scattering) has to obey the cosine law.

From equation (3.5), the incident molecular flux per unit area is

$$\Gamma = \frac{n \bar{v}}{4} \quad (3.6)$$

In a steady state with zero net flow if we equate the fluxes from the cold chamber and the hot chamber we get to equation (3.2). The flow direction is from the region of lower to higher temperature. It could also be seen from the relations of number of molecules to the density of the gas. The subscripts 1 and 2 denote the two sides at temperatures T_1 and T_2 respectively. n_1 is proportional to ρ_1 and hence to $\frac{1}{T_1}$, while n_2 is proportional to $\frac{1}{T_2}$. If $T_1 > T_2$, $n_1 > n_2$ in the ratio $\frac{T_1}{T_2}$. The velocities \bar{v}_1 and \bar{v}_2 are in the ratio of $\sqrt{\frac{T_1}{T_2}}$, thus the product $n_1 \bar{v}_1$ is less than $n_2 \bar{v}_2$ by the ratio $\sqrt{\frac{T_1}{T_2}}$. Hence, the flow will take place from cold to hot until the pressure ratio $\frac{P_1}{P_2} = \sqrt{\frac{T_1}{T_2}}$ builds to check it.

In a round tube of radius 'a' the mass flow rate 'Q_m' in free molecular regime is given by [41]

$$Q_m = -\frac{4}{3} \sqrt{\frac{2\pi}{R}} a^3 \frac{d}{dx} \left(\frac{p}{\sqrt{T}} \right) \quad (3.7)$$

The condition for zero flow is then that $\frac{p}{\sqrt{T}}$ be constant along the tube which is same as the condition found for the thermal transpiration using the flux theory [40].

For a pump set up with "s" number of stages the above formula in equation (3.2) gets

$$\text{modified to } \frac{P_1}{P_2} = \left(\frac{T_1}{T_2} \right)^{\frac{s}{2}} \quad (3.8)$$

3.1.2 Momentum theory of thermal transpiration

At an unequally heated boundary, a rarefied gas flow is seen from cold side to hot side as the gas creeps over the channel walls. The explanation of this phenomena is as follows: when the gas is hotter over one part of the wall than over an adjacent part, molecules impinging obliquely upon it strike with a higher average velocity when they come from the hotter region than when they come from the colder region, and so they are rebounded more strongly by the wall (except in the special case of specular reflection), which imparts a tangential momentum to the gas directing it towards the hotter side. Thus, number of molecules in the hotter region is less than that in the colder region and the mass fluxes from the two regions balance in a gas at rest. A momentum in the opposite direction to the temperature gradient is transferred to the wall from the gas [41].

As its reaction, the gas is subjected to a force in the direction of the temperature gradient and a flow is induced in that direction. In a gas in motion, on the other hand, a momentum in the direction of motion is transferred to the wall (*Figure 21*). Thus, a

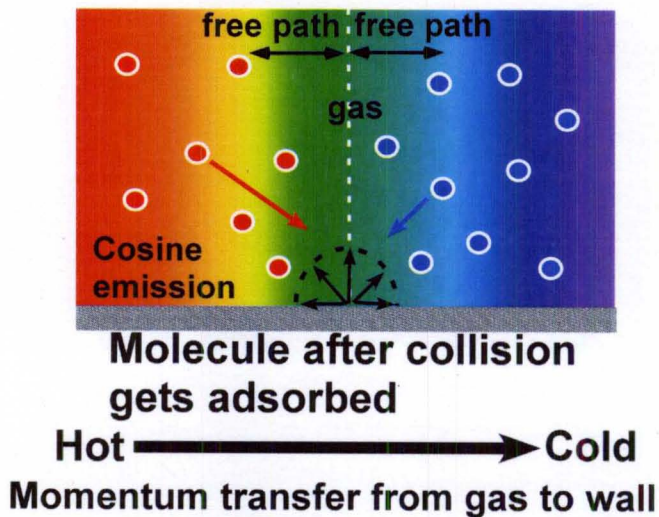


Figure 21. Diagram showing momentum transfer from gas to wall of the pump channel in thermal transpiration.

steady flow is established when the two contributions of momentum transfer balance. Thus the qualitative difference of the velocity distributive functions of the molecules impinging on the boundary and those leaving it plays an important role in thermal transpiration flow.

3.2 Thermal Transpiration models

3.2.1 Maxwell's Model

In a capillary tube of circular cross section where the assumption is that motion of gas is very slow and the temperature varies gradually along the tube so that temperature is uniform throughout any section of the tube, the condition for steady flow 'Q' parallel to the axial direction of the tube is [19]:

$$\frac{Q}{\pi \rho a^2} + \frac{1}{8\mu} (a^2 + 4Ga) \frac{dP}{dx} - \frac{3}{4} \frac{\mu}{\rho \theta} \frac{dT}{dx} = 0 \quad (3.9)$$

where, the dynamic viscosity,

$$\mu = \frac{1}{2} nm \bar{v} \lambda \quad (3.10)$$

average velocity,

$$\bar{v} = \left(\frac{8RT}{\pi} \right)^{\frac{1}{2}} \quad (3.11)$$

mean free path,

$$\lambda = \frac{kT}{\sqrt{2} \pi D_m^2 P} \quad (3.12)$$

molecular density,

$$n = \frac{P}{kT} \quad (3.13)$$

density,

$$\rho = mn \quad (3.14)$$

coefficient of slipping,

$$G = \frac{2}{3} \left(\frac{2}{f} - 1 \right) \lambda \quad (3.15)$$

where m is the mass of a gas molecule, R is the specific gas constant, D_m is the collision diameter of the gas molecules, k is the Boltzmann constant, T is the temperature along the narrow channel, P is the pressure along the narrow channel and f is a measure of

molecular reflectivity of the surface of the narrow channel ($f = 0.5$ for semi reflecting surface and $f = 1$ for a perfectly reflecting surface). In the absence of a pressure gradient, the gas flow is from the cold end to the hot end of the narrow channel.

However, in the absence of any flow, in which temperature varies from the end to end, the pressure is greater at the hot end than at the cold end. Putting $Q = 0$ in equation (3.9), indicates

$$\frac{dP}{dT} = 6 \frac{\mu^2}{\rho T} \frac{1}{a^2 + 4Ga} \quad (3.16)$$

3.2.2 Kennard's Model

The Kennard model is same as the Maxwell model except for the fact that the coefficient of slipping in the Maxwell model is replaced by the slip length ζ , which depends on the thermal accommodation coefficient of the surface. The Kennard model also assumes a near continuum ($Kn < 0.1$) flow with moderate pressures. It assumes that the gas is dense enough to extend the Poiseuille's flow equation to accommodate temperature gradient. Kennard's model for thermal transpiration driven gas flow rate 'Q' across a narrow channel with circular cross-section (radius a), under the assumption of isothermal gas flow is [40]:

$$Q = -\frac{\pi a^4 P}{8 \mu R T} \left(1 + 4 \frac{\zeta}{a}\right) \frac{dP}{dx} + \frac{3\pi \mu a^2}{4 T} \frac{dT}{dx} \quad (3.17)$$

If the two ends of the tube are sealed, the negative term showing that the Poiseuille flow and thermal creep flow are counteracting in nature, balance each other at equilibrium.

The expression for the change in pressure with temperature is

$$\frac{dP}{dT} = \frac{6\mu^2 R}{a^2 P \left(1 + \frac{4\zeta}{a}\right)} \quad (3.18)$$

3.2.3 Williams' Model

The Williams model is identical to Kennard's model except the slip length ζ , which is expressed more precisely in terms of the coefficient of accommodation of the gas molecules to the channel walls. The slip length [42] is

$$\zeta = \mu \sqrt{\frac{\pi RT}{2}} \left[\frac{2-\sigma}{\sigma} \right] \quad (3.19)$$

where σ is the accommodation factor. If the pressure and temperature are normalized (P^* and T^* respectively) with respect to the pressure and temperature at the cold end of the tube, i.e.,

$$P^* = \frac{P}{P_c} \quad (3.20)$$

$$T^* = \frac{T}{T_c} \quad (3.21)$$

The equation relating pressure and temperature becomes

$$\frac{dP^*}{dT^*} = \frac{\frac{\mu^2 RT_c}{P_c^2 D^2}}{P^* + 8 \left(\frac{\pi}{2}\right)^{\frac{1}{2}} \left(\frac{2-\sigma}{\sigma}\right) \frac{\mu \sqrt{(RT_c)}}{P_c D} T^*} \quad (3.22)$$

The two features of this equation are: First, the parameter $\frac{\mu \sqrt{(RT_c)}}{P_c D}$ is proportional to the Knudsen number since $\frac{\mu \sqrt{(R_g T_c)}}{P_c} \sim \lambda$, where λ is the mean free path of the gas molecules and $P_c D$ is essentially the inverse of the Knudsen number. Thus, the solution depends on the Knudsen number. Second, the solution is independent of the length of the tube.

3.2.4 Knudsen's Model

Unlike the Maxwell, Williams, Kennard models, the Knudsen model is an empirically corrected model that is applicable to either very small K_n or very large K_n gas

flow through narrow circular capillaries. Like all the other models discussed above, this model also assumes isothermal gas flow along a capillary with circular cross-section. In the absence of any effective flow along the channel, the equilibrium change in pressure with respect to change in temperature is [43]:

$$\frac{dP}{dT} = \frac{1}{\frac{8}{3k_1\lambda} + \frac{\pi(0.81)a^2}{16(0.49)\lambda^2 k_1}} \frac{P}{2T} \quad (3.23)$$

where, k_1 is an empirically determined factor. $k_1=1$ if K_n is large and k_1 converges between 2 and 3 if K_n is small.

3.2.5 Sharipov's model:

Sharipov's model is based on a more precise model, the S-model [44], to simplify the collision term in the Boltzmann Transport Equation. Hence, the Sharipov model is applicable to all the flow regimes ($K_n > 0$). The average mass flow rate of gas through a capillary from the cold end to the hot end is:

For a circular cross-section [45]:

$$\dot{M} = p_{av} \sqrt{\frac{m}{2kT_{av}}} \frac{\pi^3}{L} \left(\frac{\Delta T}{T_{av}} M_t - \frac{\Delta p}{p_{av}} M_p \right) \quad (3.24)$$

For a rectangular cross-section [46]:

$$\dot{M} = p_{av} \sqrt{\frac{m}{2kT_{av}}} \frac{Ah}{L} \left(\frac{\Delta T}{T_{av}} M_t - \frac{\Delta p}{p_{av}} M_p \right) \quad (3.25)$$

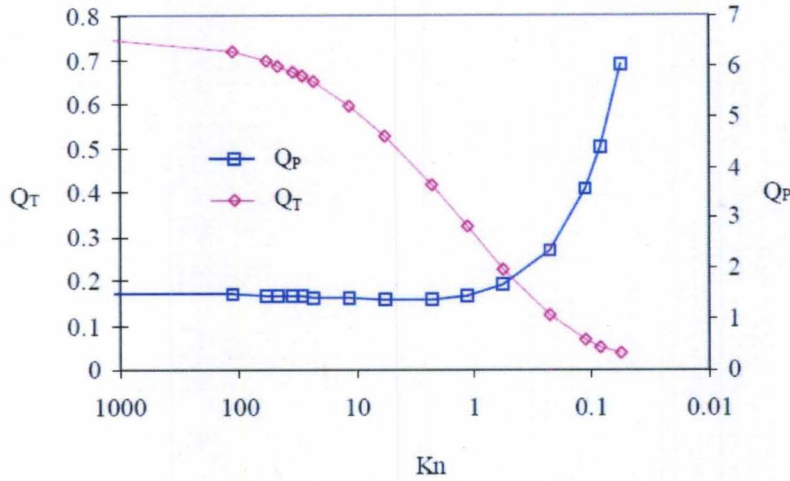


Figure 22. Flow coefficients against a range of Knudsen numbers for circular capillary. (figure taken from [49])

where Δp is the pressure difference, p_{av} is the average pressure in the capillary tube, ΔT is the temperature difference, T_{av} is the average temperature in the capillary tube, M_T is the thermally driven flow coefficient, M_P is the pressure driven return flow coefficient, A is the capillary's cross-sectional area, h is the height (hydraulic diameter) of the capillary tube, r is the radius for the circular capillary, L is the length of the capillary tube, m is the molecular mass of a single molecule of gas, and k is Boltzmann's constant.

At equilibrium flowrate is zero. Physically, the two competing flows illustrated in Figure 17 (the thermally driven flow that is described by M_T , and the pressure driven flow that is described by M_P) form the net gas flow. The visualization of the flow coefficients as a function of Knudsen number shown in Figure 22 is helpful for understanding the flow characteristics. When equation (3.25) is set equal to zero, the thermally driven upflow is exactly balanced by the pressure driven return flow. In this situation, the pressure change Δp is at its maximum value designated as Δp_{max} , and equation (3.25) reduces to

$$\frac{\Delta p_{max}}{p_{av,max}} = \frac{\Delta T}{T_{av}} \frac{M_T}{M_P} \quad (3.26)$$

where M_p and M_t are the pressure and temperature coefficients that depend on the rarefaction parameter δ_{avg} :

$$\delta_{avg} = \left(\frac{\pi^3}{2}\right)^{\frac{1}{2}} \frac{aD_m^2 P_{av}}{kT_{av}} = \frac{\sqrt{\pi}}{2K_n} \quad (3.27)$$

The poiseuille flow ' Q_{POS} ' in the center of the channel which allows gas flow in the viscous regime follows this equation:

$$Q_{POS} = \frac{\pi D_L^4}{128\mu l} \Delta P \quad (3.28)$$

where D_L is the diameter of the channel and ΔP is the pressure head across the channel, μ is the viscosity of the gas and l is the length of the channel.

This model is based on semi analytical approach and is one of the best analytical alternatives to DSMC – “Discrete Simulation Monte Carlo” techniques. This model can be applied to non-isothermal gas flows too.

In this model, it is also shown that the gas pumping rate increases as the width of the channel increases for a given height since the flowrate is proportional to the area of cross section of the channel height, and then the flowrate reaches saturation regime due to edge effects. So, this model gives alternative options to channel fabrication designs. Also, for a greater channel height the flowrate is higher but the pumping capability is lower due to reverse thermal creep.

The resulting pressure distributions from DSMC, IP-DSMC (Information Preserving DSMC) and Sharipov's Boltzmann Transport Equation models are presented in *Figure 23* for a channel length of 5 μm and various heights of (1 μm , 100 nm, and 20 nm) with a linearly varying temperature from 273°K to 573°K along the channels [47]. Considering the degree of non-idealities in short channels the graph in *Figure 23* shows that Sharipov's model is in excellent agreement to the DSMC and IP-DSMC models. In Information Preserving DSMC (IP-DSMC) method, certain macroscopic quantities are "preserved" along with the microscopic velocities used in the DSMC simulations. These preserved quantities are then transported by particle movement and modified by boundary interactions, particle collisions, and fluxal modifications.

3.3 Knudsen Pump or compressor

The phenomenon of thermal transpiration can be used for creating vacuum by

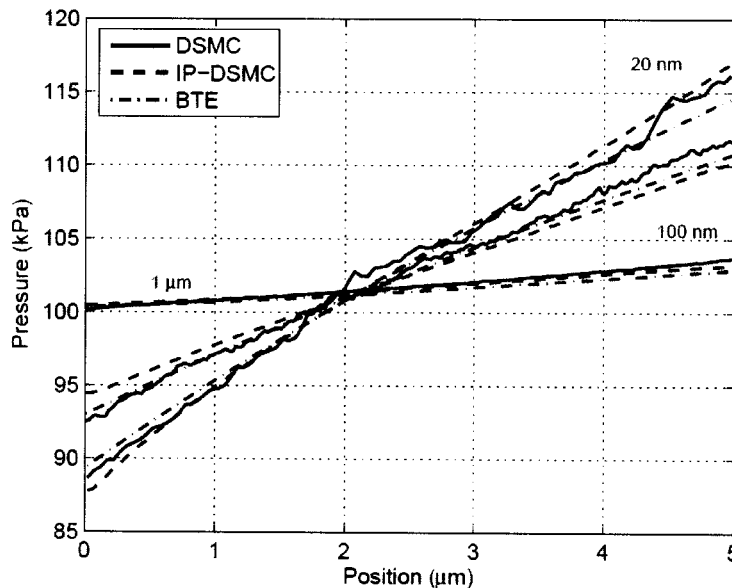


Figure 23. Pressure distributions for 5 μm long channels comparing DSMC, OSIP-DSMC, and Sharipov's BTE solutions. (figure from [47])

either sucking in air from one closed chamber or as a compressor by forcing in air into a chamber [48]. In both of these processes thermal transpiration will be used as either a vacuum pump or as a compressor. Based on requirements, single stage pumps can be cascaded in series to obtain a higher pressure difference or may be arrayed in parallel for a higher flow rate.

A pump diagram for a three chamber Knudsen pump, which is easily cascaded, is shown in *Figure 24*. The narrow channels between the cold inlet chamber and the heated chamber are where the pressure change occurs. Thermal transpiration is the dominant mass flow phenomenon in the narrow channels. The larger channels which have diameters suitable for a viscous flow are dominated by pressure flow and move the fluid from the hot to the cold exit chamber, forming a complete pump with two stages [29].

As indicated in *Figure 17*, thermal creep flow is driven from the cold end of a tube towards the hot end of the tube. For free molecular flow, thermal creep flow will fill the entire tube, becoming thermal transpiration. In the case of transitional flow, the thermal creep occurs closer to the tube's walls. As a pressure difference is established a

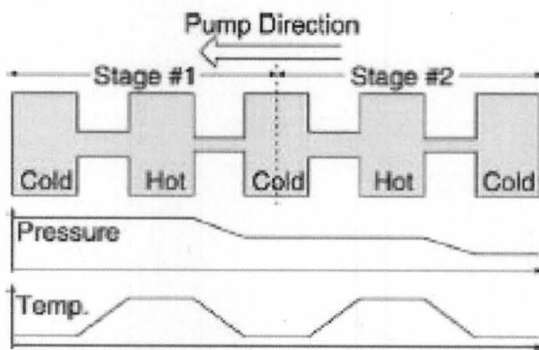


Figure 24. A two-stage Knudsen pump cascaded in series, showing resultant pressure change. (figure taken from [29])

pressure return flow will occur, partially or completely balancing the thermal creep flow. Thus, thermal creep can also produce a net gas flow and a pressure difference, which again are the requirements for a pump.

Since the thermal conductivity of the tube wall is significantly larger than the gas conductivity, the temperature distribution is determined by the thermal property of the tube. If the tube thermal conductivity is constant, the temperature distribution is linear.

3.4 Theoretical calculation of pressure drop on the cold side of the pump as a function of time:

The dynamic response of the pressure on the cold or sealed outlet is an important aspect to model for subsequent important results. The pressure drop versus time is definitely an exponential function which fits very nicely with theoretical and experimental results. Young in his thesis had proposed and derived a formula for the time constant τ which is given by [49]:

$$\tau = \frac{1}{C_m \frac{Q_P}{Q_T} \left(\frac{1}{V_H + V_C} \right)} \quad (3.29)$$

where C_m is the conductance of the membrane, Q_P and Q_T are the pressure and temperature coefficients respectively and V_H and V_C are the volumes of the hot and cold chambers respectively. In our pump's case the hot side is opened to the atmosphere and thus the term V_H drops off from the equation.

With this above constant the pressure drop with respect to time becomes:

$$\Delta p(t) = \Delta p_{max} \left(1 - e^{-\frac{t}{\tau}} \right) \quad (3.30)$$

In Han's thesis the conductance of both the cold and hot side are taken into account which modifies the above formula of the time constant to [49]

$$\tau = \frac{1 + C_m \frac{Q_P}{Q_T} \left(\frac{1}{C_H} + \frac{1}{C_C} \right)}{C_m \frac{Q_P}{Q_T} \left(\frac{1}{V_H} + \frac{1}{V_C} \right)} \quad (3.31)$$

where C_H and C_C are the conductances of the hot and cold side inlet pipes respectively. If the pressure drops in these inlets are negligible compared to that along the membrane thickness then equation (3.31) becomes same as that of equation (3.29). Han considered the conductance as only the thermally driven conductance of the gas flow

$$C_m = A \frac{h}{L} \sqrt{\frac{kT_{avg}}{2m}} M_T \quad (3.32)$$

This conductance formula used is for transitional flow regime. In the model for our thermoelectric pump the conductance accounts for both thermally driven and pressure driven flow conductances.

Using the ideal gas law

$$PV = NkT \quad (3.33)$$

where N is the number of particles of the gas, P = pressure, V = volume, k = Boltzmann constant and T = absolute temperature.

$$N = \frac{PV}{kT} \quad (3.34)$$

Time rate of change of N

$$\dot{N} = \frac{dN}{dt} \quad (3.35)$$

$$\dot{M} = \frac{dM}{dt} \quad (3.36)$$

where \dot{M} is the flowrate of the gas

$$\dot{M} = m \frac{dN}{dt} \quad (3.37)$$

$$= m\dot{N} \quad (3.38)$$

$$= m \frac{V_h}{kT} \frac{dP_h}{dt} \text{ (for hot side chamber, in our pump's case the hot side is open to atmosphere so } V_h \sim \infty \text{)} \quad (3.39)$$

$$= -m \frac{V_c}{kT} \frac{dP_c}{dt} \text{ (for cold side chamber)} \quad (3.40)$$

(negative signs is for opposite direction of flow. The gas fills in the hot chamber whereas it empties out of the cold chamber)

We also know that sharipov's equation of flow in transitional regime through a rectangular capillary where $l \gg w$

$$\dot{M} = \frac{P_h + P_c}{2} \sqrt{\frac{m}{k(T_c + T_h)}} \frac{Ah}{l} \left[2 \frac{T_h - T_c}{T_h + T_c} M_t - 2 \frac{P_h - P_c}{P_h + P_c} M_p \right] \quad (3.41)$$

$$= \sqrt{\frac{m}{k(T_c + T_h)}} \frac{Ah}{l} \left\{ \left[\frac{T_h - T_c}{T_h + T_c} M_t - M_p \right] P_h + \left[\frac{T_h - T_c}{T_h + T_c} M_t + M_p \right] P_c \right\} \quad (3.42)$$

$$= \alpha + \beta P_c \quad (3.43)$$

$$\text{where } \alpha = \sqrt{\frac{m}{k(T_c + T_h)}} \frac{Ah}{l} \left[\frac{T_h - T_c}{T_h + T_c} M_t - M_p \right] P_h \quad (3.44)$$

$$\text{and } \beta = \sqrt{\frac{m}{k(T_c + T_h)}} \frac{Ah}{l} \left[\frac{T_h - T_c}{T_h + T_c} M_t + M_p \right] \quad (3.45)$$

In the above analytical derivation the number of pores has to be considered since the net conductance of all the pores pumping in parallel will sum up. Flowrate is directly proportional to the number of pores in the membrane. The number of pores can be approximated based on the porosity of the membrane. If the channel material is P% porous, R is the radius of the membrane and r is the radius of the pore, then the number of the pores

$$N_p = \left(\frac{R}{r}\right)^2 \frac{P}{100} \quad (3.46)$$

For a porous membrane with 'N_p' pores or channels \dot{M} becomes $N\dot{M}$

Equating (3.40) and (3.43)

$$\Rightarrow -\frac{mV_c}{kT} \frac{dP_c}{dt} = N_p \alpha + N_p \beta P_c \quad (3.47)$$

$$\Rightarrow \frac{dP_c}{dt} + \frac{kT}{mV_c} N_p \beta P_c = -\frac{kT}{mV_c} N_p \alpha \quad (3.48)$$

$$\Rightarrow \frac{dP_c}{dt} + p(t)P_c = q(t) \quad (3.49)$$

$$\text{where } p(t) = \frac{kTN_p\beta}{mV_c} \quad (3.50)$$

$$\text{and } q(t) = \frac{-kTN_p\alpha}{mV_c} \quad (3.51)$$

Using first order linear differential equations

$$\mu = \exp\left(\int p(t)dt\right) \quad (3.52)$$

$$= \exp\left(\frac{kT}{mV_c} N_p \beta t\right) \quad (3.53)$$

$$P_c = \frac{1}{\mu} \int \mu q(t) dt + \frac{1}{\mu} C \quad (3.54)$$

Here, C is a constant of integration

$$= \frac{1}{\exp\left(\frac{kT}{mV_c} N_p \beta t\right)} \left[\int -\frac{kT}{mV_c} N_p \alpha \exp\left(\frac{kT}{mV_c} N_p \beta t\right) dt + C \right] \quad (3.55)$$

$$= C \exp\left(\frac{-kT}{mV_c} N_p \beta t\right) - \frac{\alpha}{\beta} \quad (3.56)$$

Applying boundary conditions, at t=0, pressure on the cold side of the pump P_c=0

$$P_c(0) = C - \frac{\alpha}{\beta} \quad (3.57)$$

$$C = \frac{\alpha}{\beta} + P_c(0) \quad (3.58)$$

$$P_c(t) = \left[\frac{\alpha}{\beta} + P_c(0) \right] \exp\left(-\frac{kT}{mV_c} N_p \beta t\right) - \frac{\alpha}{\beta} \quad (3.59)$$

Thus, the pressure difference obtained by the pump at any given time 't' is

$$\Delta P(t) = P_c(0) - P_c(t) = \left(\frac{\alpha}{\beta} + P_c(0) \right) (1 - e^{-\frac{t}{\tau}}) \quad (3.60)$$

$$\text{where } \tau = \frac{mV_c}{kTN_p\beta} \quad (3.61)$$

The number of pores is very difficult to estimate especially when the porous membrane is like a sponge where the pores are in a network rather than straight hollow cylinders. Also, there could be imperfections or leakage due to damage in the membrane in case of which the pores of the affected area will not contribute to gas pumping. The exponential decay is the time it takes to evacuate the cold side chamber. In these experiments it comprises of the pressure sensor's dead volume which is about 0.8 cm³ and the air in the inlet pipes from the membrane to the sensor which in total comes out to be approximately 1 cm³. The time constant will also depend on the thermal mass of the system since that will determine how fast the system attains the temperature difference. The plots of *Figure 25*, *Figure 26* & *Figure 27* are obtained by using the data from

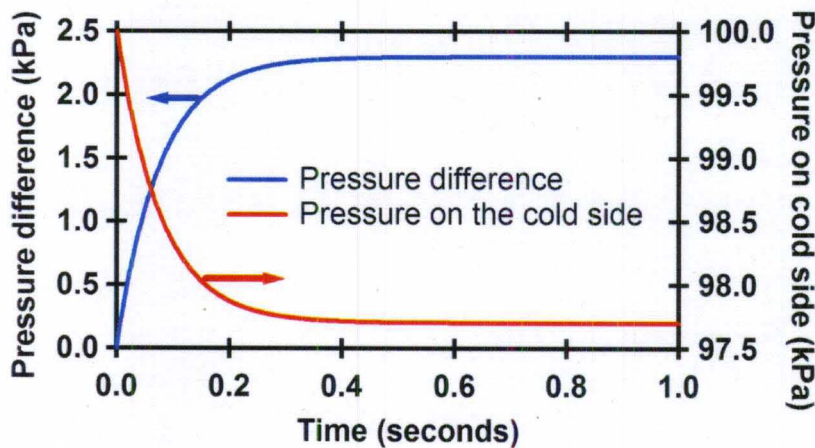


Figure 25. Theoretical pressure drop plotted as a function of time for 25 nm pore size membrane. The hot and cold side temperatures used in equation (3.59 & 3.60) is 353 K and 324 K respectively.

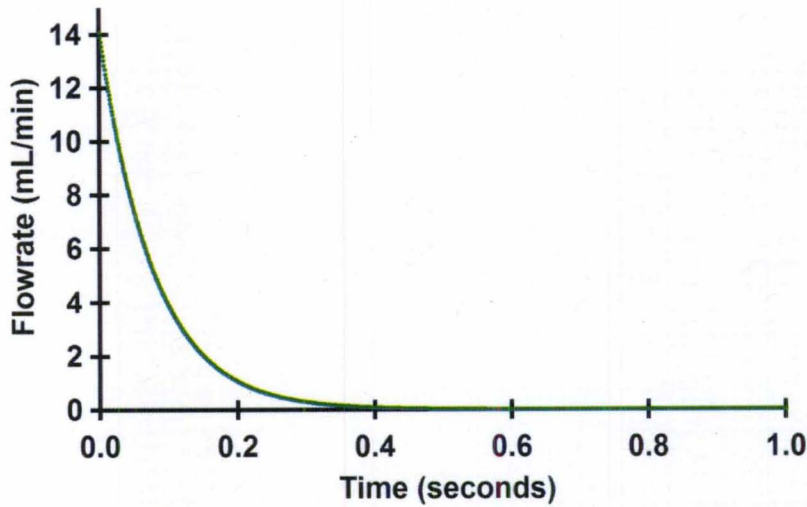


Figure 26. Theoretical flowrate with time is obtained by substituting the dynamic pressure (equation 3.59) on the cold side pressure in equation 3.41.

Table 1 which are obtained from the experimental conditions in Section 6.5.1 of Chapter 6 for the case of radial design thermoelectric pump using cellulose ester membrane as the channel material, in the theoretical equations.

Table 1. Various parameters with their numerical values used in computing theoretical results.

Parameter	Value
Hot side temperature (T_h) = 353K	353 K
Cold side temperature (T_c) = 324K	324 K
Length of pump channel (L) = 105 μ m	105 μ m
Radius of capillary ($h/2$)	25/2 nm
Number of pores (N_p)	7e11
Molecular mass of air (m)	28*1.67e-27 kg
Volume of cold side chamber (V)	1 cm ³
Temperature flow coefficient (M_t)	0.38
Pressure flow coefficient (M_p)	1.4

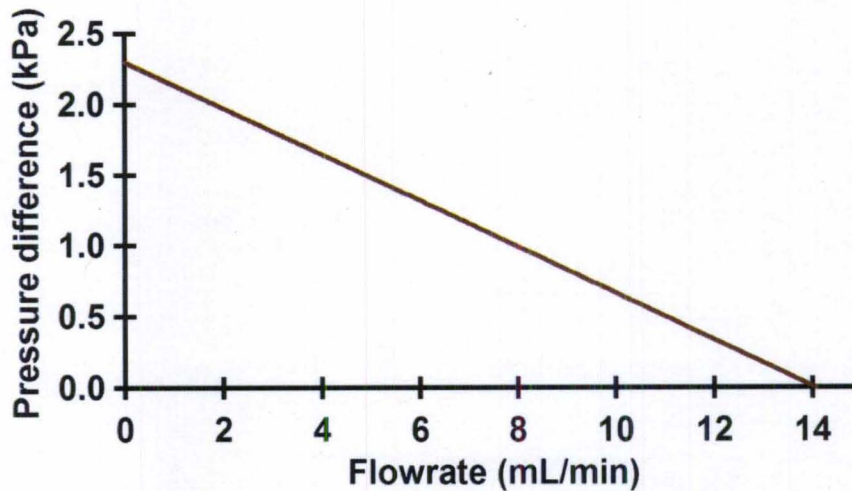


Figure 27. Theoretical plot of pump pressure difference with respect to flowrate by using the data of flowrate and pressure drops obtained from Figures (25 & 26).

In this theoretical model the time required for the pressure drop is less than a second and that is attributed to the more number of pores in the theoretical model compared to the actual pores contributing to thermal transpiration in the experiments.

The exponential decay is explained as follows. The curve has a higher slope to start with where the thermal transpiration is at its peak with very little of the back flow. At this point the pump has the maximum flowrate. Slowly with building up of pressure on the hot side the pressure driven flow negates the transpirational flow. When the curve stabilizes that time the flow rate is zero and the pressures on the cold and hot sides settle at the square root of their absolute temperatures. The flowrate of the gas evacuated from the cold chamber is proportional to the derivative of the pressure versus time graph at a constant power. The reverse flowrate is proportional to the hydraulic conductance times the pressure differential.

The net flowrate against time is plotted in *Figure 26* by substituting the dynamic pressure (equation 3.59) on the cold side in equation 3.41. A maximum flowrate of 14 mL/min is obtained theoretically when the pressure difference term in equation (3.41) is 0 which is the condition for computing maximum flowrate.. The pressure differential versus flowrate graph is obtained in *Figure 27* by combining *Figure 25 & Figure 26* to compare with experiments in Section 6.5.1 of Chapter 6.

3.5 Thermally Driven Flows in Sub-Nano/Nanoscale Size Channels

At channel dimensions in the order of sub nano meter range the attractive forces like Van der Waals forces between the channel walls and the molecules is more pronounced compared to that in larger dimensions which results in an increased thermally driven flow due to higher density of molecules near the wall.

Also, when the mean travel distance for collision of the molecule to that of the wall is of the order of the phonon mean free path then phonon coupling takes place. Phonon coupling is defined as the coupling of gas flows near the wall to the phonon flux in the wall material [50, 51]. The coupling occurs when the mean travel distance of the molecules along the tube axis between collisions with the channel's wall is on the order of the phonon mean free path in the solid, leading to an enhancement of the collisional coupling between phonon and molecule flows. Phonon coupling will be most feasible for crystalline structures and diminish in random amorphous materials such as aerogel.

The drag caused due to phonon-molecule coupling, increases gas density near the wall and counteract the potential for the increased efficiency mentioned above for thermally driven flows. For low enough temperatures, which enhance the coupling, the phonon drag could even drive the flow in the opposite direction.

Thus, phonon drag effects may become important at low temperatures and at pore sizes below 5 nm.

3.5.1 Nanoscale Pore Condensation

The narrower the constriction of the flow channel the more is the gas adsorption on the channel walls [35]. This effect can lead to flow channel blockage through gas condensation. It also may lead to flow enhancement in pressure-driven flows [52]. The increased adsorption in the capillaries is from the high curvature of the smaller diameter channels. The potential energy inside a nano channel behaves like the Lennard Jones potential model [53].

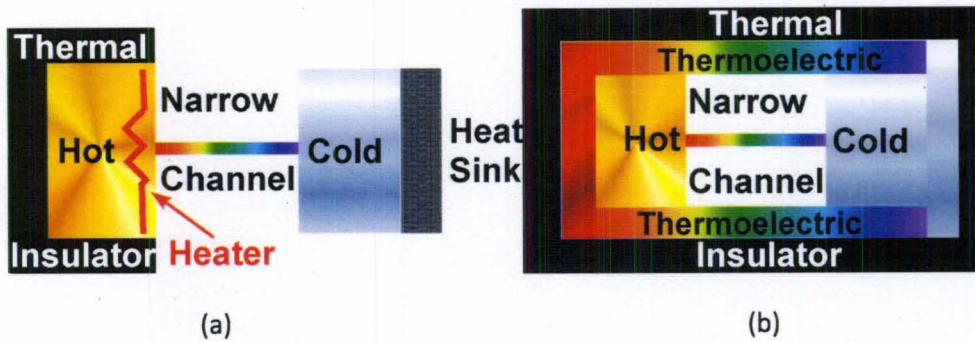


Figure 28. Figure in (a) shows one directional Knudsen pump with asymmetric design using a resistive heater and heat sink, while the figure in (b) shows a bidirectional pump with symmetric design by using a thermoelectric.

3.6 Improvement of pump efficiency

To maintain a temperature gradient one end of the channel has to be kept at a higher temperature compared to the other end. Materials with sufficiently low thermal conductivities (order of 10's of mW/m·K) are required to minimize the energy required to maintain the temperature difference across the transpiration membrane efficiently. This could be achieved by active heating of the hot side and passive cooling of the cold side which so far has been the design of most Knudsen pumps or compressors [29, 30, 35, 48]. But if instead the temperatures of both ends are actively controlled by active heating and active cooling the respective ends of the channel then a higher temperature difference can be obtained along the same length of the channel compared to that of only actively heating the hot side [15] compared in *Figure 28*. This in turn should boost the efficiency of the pump since a higher temperature difference will have a higher pressure drop along the channel which will enhance the flowrate. Also, in the flux theory of thermal transpiration the flow from cold to hot side is due to a higher flux of gas molecules on the colder side compared to that of the hotter side. In the formula for flux, it is easily seen that a lower cold side temperature facilitates higher flux of molecules approaching from

the cold side and thus there will be a net increase in the flux moving from the cold to the hot side. By using active temperature control only on the hot side and passively cooling the cold side the temperature on the cold side is limited to a maximum of room temperature which ultimately limits the flux on the cold side and thus the net gas flow.

Thus, a new design has been proposed in this research where the hot side of the channel is heated as usual but simultaneously the cold side of the channel is cooled too maintaining it below or at about the room temperature, thus obtaining a higher temperature difference and higher net flow.

The above operation was implemented by using a thermoelectric material which acts like a heat pump when current is passed through it. With current the charge carriers in the material flow in a direction either same or opposite to that of the current depending on their polarity and thus carry the heat generated with them from one side (cold side) to another side (hot side). This property of a thermoelectric material also makes this Knudsen pump bi-directional, since the hot and cold sides can be reversed just by changing the direction of the current flow. This is the first ever bi-directional Knudsen pump to date.

3.7 Thermoelectric concept

The thermoelectric effect was first discovered by T. J. Seebeck in 1821, where he showed that an electromotive force could be produced by heating the junction between two different electrical conductors. Years later Peltier made his discovery where he found passage of an electric current through a thermocouple produces a small heating or cooling effect depending on its direction. Both the Seebeck effect and the Peltier effect are related to each other. When a current passes from one material to another, the energy transported

by the electrons is altered, from one material to another, the difference appearing as heating or cooling at the junction – Peltier effect. Likewise, when the junction is heated, electrons are enabled to pass from the material in which the electrons have the lower energy into that in which their energy is higher, giving rise to an electromotive force. It was only in the 1950s that the advent of semiconductor materials as thermoelectrics led to the development of practical Peltier refrigerators and also led to construction of thermoelectric generators with high enough efficiency for power harnessing applications.

When a current 'I' is passed through the couple there is peltier cooling at the source equal to $(\alpha_n - \alpha_p)IT_1$, where T_1 and T_2 are source and sink temperatures respectively and α_n and α_p are the Seebeck coefficients of the two branches with opposite sign shown in *Figure 29*. The cooling effect is opposed by the heat conduction at the rate $(T_2 - T_1)(K_p + K_n)$, where K_p and K_n are the material thermal conductivities of the two branches. The cooling is also opposed by the joule heating due to the contact resistances R_p and R_n within the p and n thermoelements respectively. Half of the joule heating passes to the

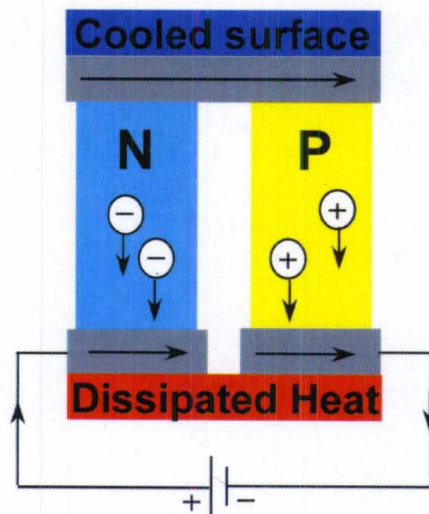


Figure 29. Schematic of a peltier cooler showing the flow of charge carriers in the thermoelectric material which leads to a hot and a cold side.

source and half of it goes to the sink. The maximum heat flux pumping capability for a thermoelectric device 'q' is given by [54] :

$$q = (\alpha_p - \alpha_n)IT_1 - (T_2 - T_1)(K_p - K_n) - I^2 \frac{(R_p + R_n)}{2} \quad (3.62)$$

A variety of metals and semiconductors can in principle be used as thermoelectric materials. However, the figure of merit for metals is very small due to their small Seebeck coefficient and large thermal conductivity. Semiconductors offer much greater control because one can control the transport properties by doping and alloying semiconductors. The figure of merit of a thermoelectric determines how good its characteristics are. The lower the thermal conductivity and higher the electrical conductivity the better is the thermoelectric since figure of merit Z is given by:

$$Z = \frac{S^2 \sigma}{K} \quad (3.63)$$

where σ is the electrical conductivity, K is the thermal conductivity and S is the thermopower of the material. But the parameters in Z are interdependent so it is not so easy to control one without affecting the other. A major research in the field of energy is to engineer these parameters for a high Z. These parameters could be depicted at the tips

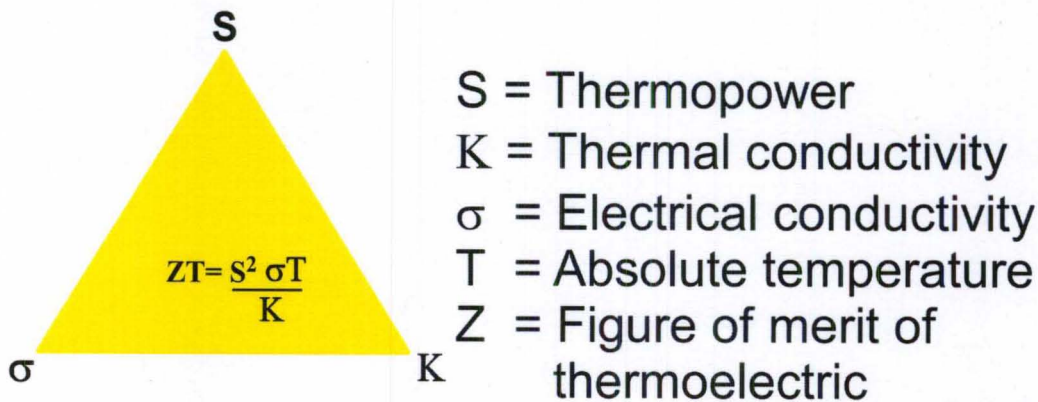


Figure 30. The three crucial parameters of a thermoelectric shown at the vertices of a triangle, showing how crucial it is to optimize them so as to get a highly efficient thermoelectric.

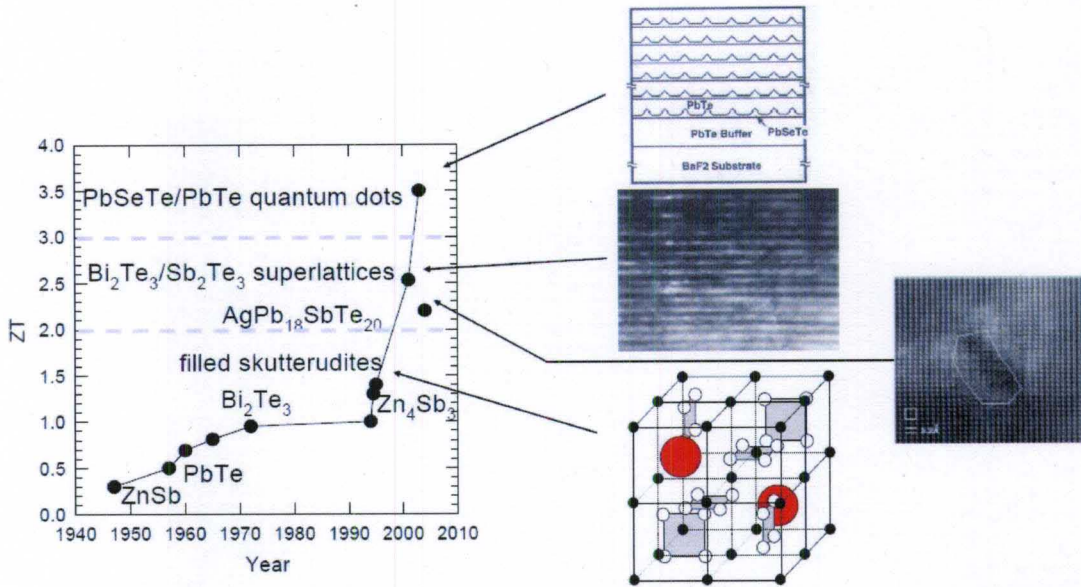


Figure 31. Many of the recent thermoelectric materials have attained a higher figure of merit in nano dimensional form compared to their bulk counterparts. (figure from "Vehicular Thermoelectrics Applications Overview" presented at DEER 2007)

of a triangle to show their contribution to the thermoelectric figure of merit shown in Figure 30.

3.8 Properties of nano structured thermoelectric materials

The advanced version of this project deals with nanoporous thermoelectric as a pump. A brief discussion about the properties of nano structured thermoelectric will benefit the reader. These properties will throw light on the fact why the nanoporous thermoelectric would suit the pump better compared to a peltier module. Nanoporous thermoelectric is essentially a form of nano structured thermoelectric. The graph in Figure 31 shows the improved figure of merits of nanostructured thermoelectrics. The approach of increasing ZT through reducing the thermal conductivity, has greatly benefitted from recent advances in semiconductor nanostructure synthesis. For example, while considered a poor TE material in the bulk phase ($ZT < 0.01$ at 300 K), Si was recently shown experimentally to have significantly increased ZT values in the form of

nanowires ($ZT \sim 0.6$ at 300 K) [55, 56] largely due to the sharp decrease in κ (from 150 W/mK in the bulk to 0.76–1.6 W/mK in the nanowires). The first proposal to increase the figure of merit by nanostructuring was made by Hicks *et al.* [57, 58]. It was suggested that as the dimensionality of a material is decreased by nanostructuring a new variable (length scale) becomes available for the control of materials properties.

In semiconductors, the thermal conductivity has contributions from both electrons and phonons, majority coming from phonons [59]. Phonon thermal conductivity can be reduced without causing too much reduction in electrical conductivity. Phonon surface and interface scattering can lower thermal conductivity in sub 100nm range by a factor of 2-5. In case of matrix of quantum dots electrons have to move between the dots in order to transfer heat from one location to another. If the electronic bands in the dots are very narrow, then electrons are highly confined and it is not easy to take them out of

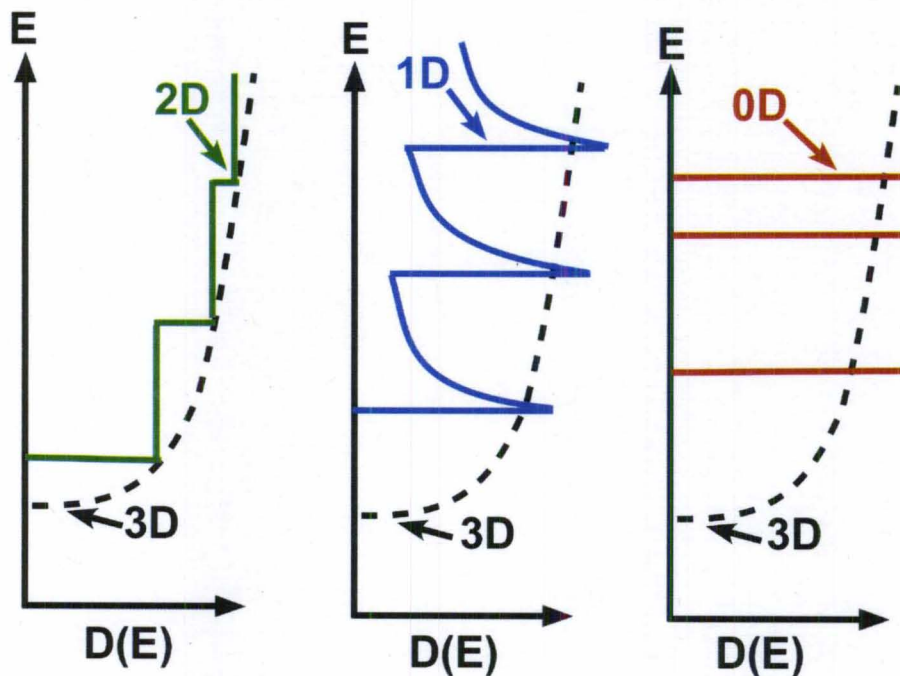


Figure 32. Density of states for 2D, 1D and 0D materials, the dotted line shows the density of states for a typical 3D material.

the dots. This change in the density of states with nanostructuring arises due to quantum-confinement effects, which arise when the length scale is made small enough as the number of atoms in any direction (x, y, or z) becomes small. In these low dimensional materials the density of states show a rapid variation with energy for example, in the 2D system the density of states show step like changes as shown in *Figure 32*. If the chemical potential is positioned close to these steps or regions with rapid variation of the density of states one can theoretically tune the thermoelectric properties to achieve a large value of $S^2\sigma$, which is in the numerator of the figure of merit ZT . Furthermore, in a nanostructured material the introduction of many interfaces, leads to a reduction in thermal conductivity due to the scattering of phonons at the interfaces. This has been studied theoretically by various groups and has been experimentally demonstrated by Kim *et al.* [60] in nanostructured materials. It is also possible to selectively scatter phonons without affecting electrons if the length scales associated with phonons and electrons are different. For example, if the phonon mean free path is larger than the electron mean free path one can nanostructure a material with interfaces having a periodicity smaller than the mean free path of phonons Porosity is one of the strategies to parse the electron and phonon mean free path differences [61]. By creating porous structures with pore sizes falling between the native electron and phonon mean free paths, it is possible to disturb phonon transport more than electron transport to increase $\frac{\sigma}{\kappa}$ ratio and thus the ZT .

CHAPTER 4 – UNIDIRECTIONAL KNUDSEN PUMP

4.1 Lateral design microfabricated Knudsen pump

A lateral design was implemented for the Knudsen pump which was fully micromachined. The nanochannels for thermal transpiration are wide channels and the enclosing cover is supported by pillars to prevent it from collapsing. The wide channel design was implemented to obtain a higher flowrate. The wide channel will still favor thermal transpiration because of the cosine law most molecules will travel the distance to reach the height of the channel and collide with the channel wall first and a very few of them which will travel the distance along the width of the channel will collide with each other first before hitting the channel wall. This is even verified by the definition of hydraulic diameter which has to be of the order of the mean free path of the gas for thermal transpiration to take place. Since, hydraulic diameter $d = \frac{4 \cdot \text{area}(w \cdot h)}{\text{perimeter}(2w + 2h)}$, if width(w) \gg height(h), $d \sim 2h$. The height of the wide channel is designed for the gas to flow in transition regime.

4.1.1 Glass and silicon lateral micro-machine pump

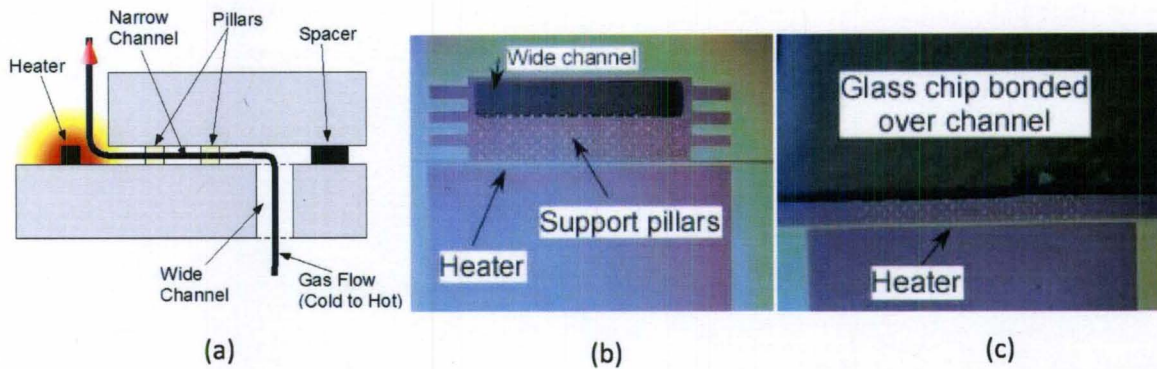


Figure 33. (a) Schematic of the lateral microfabricated pump, (b) Lateral channel pump without the top cover in between the cold chamber opening and the metal patterned heater (c) with enclosed channel, open at the heat source end and the cold end, bonded to the bottom substrate along the edges of the channel.

The substrate forming the channel is silicon and the channel cover is made up of glass in one design and silicon in another design. The fabrication involved a 3 mask process. A schematic of the lateral design pump with the gas flow direction is shown in

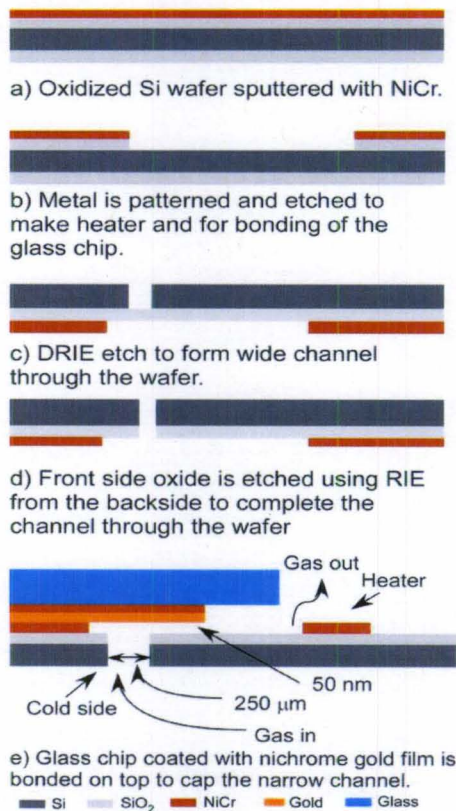


Figure 34. Process flow for the lateral design microfabricated single channel pump with bottom substrate as silicon and top cover as glass.

Figure 33a. A resistive heater is used to heat the hot side of the channel. The heater is in the form of a line trace with bond pads at the ends for probing. Nichrome is chosen as the heater material [62]. The channel cover is formed by flip chip bonding glass or silicon to the silicon substrate [63, 64]. The optical images of the fabricated chips are shown in *Figure 33 (b&c)* and the process flow is shown in *Figure 34*.

Both silicon and glass are used for their respective advantages. The glass being less thermally conductive will allow the heat transfer less from the hot end to the cold end of the channel while with a silicon cover heat dissipation to the ambient will be better than compared to a glass cover. Both of these designs proved inefficient since silicon being highly thermally conductive, a significant temperature gradient could not be maintained along the channel length. The failure of the channel to attain the temperature difference is shown in the IR images in *Figure 35*. When the chip is powered ON the Infra red image shows no variation in temperature contours along the length of the channel which proves that the channel is longitudinally at almost similar temperature and there is absence of temperature gradient. The metal patterned heater trace on the channel

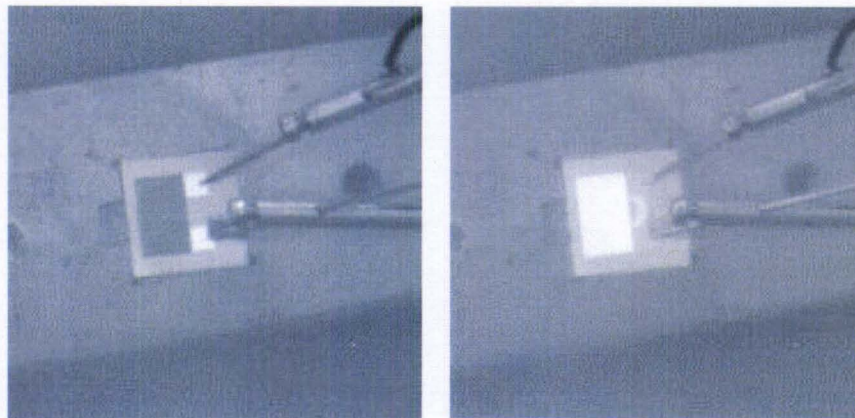


Figure 35. Infra red camera image with chip (a) OFF, (b) ON

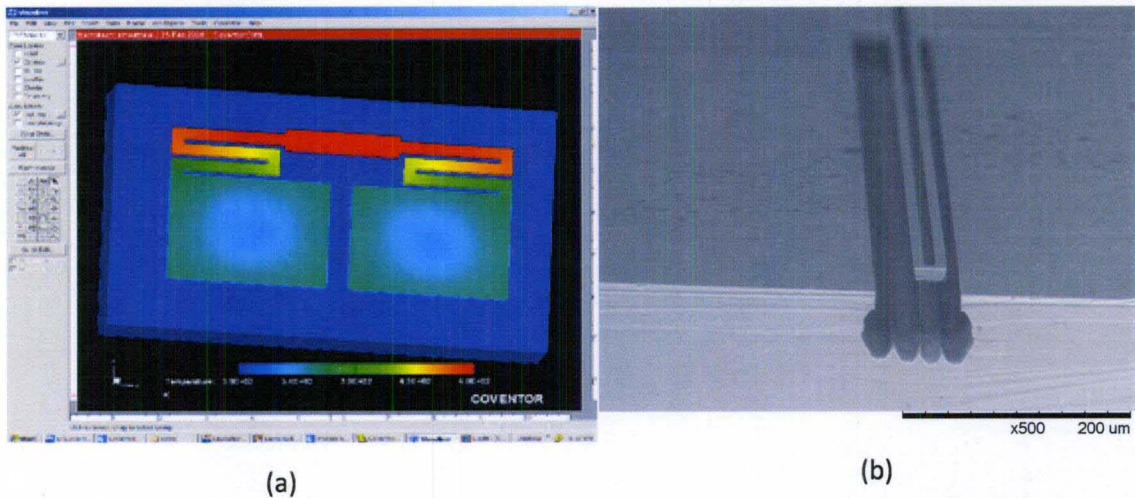


Figure 36. (a) Simulation to show that a serpentine heater structure will distribute uniform heat along the width of the channel, (b) experimentally fabricated suspended heater trace in silicon using SCREAM like process.

substrate was definitely a prime reason for the failure.

4.1.2 Silicon micro-machined pump

Due to the shortcomings of the design in section 4.1.1, the next design implemented an isolated heat source from the channel substrate by fabricating suspended

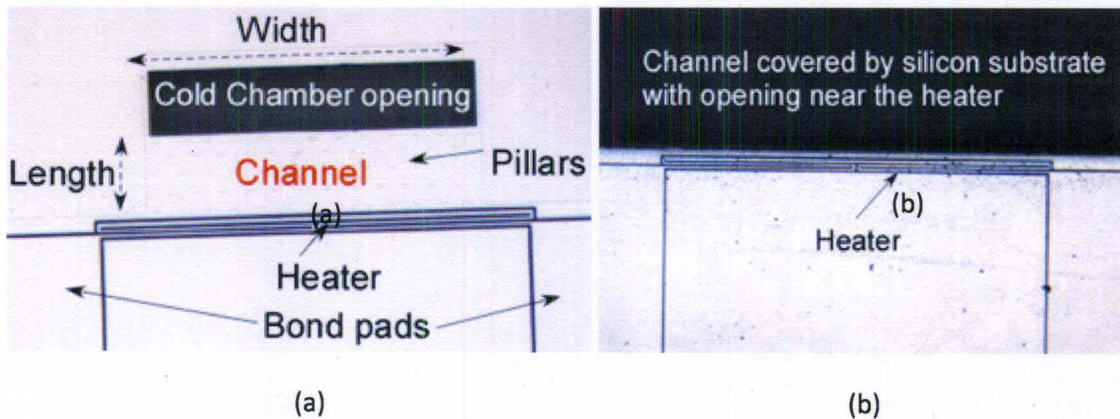
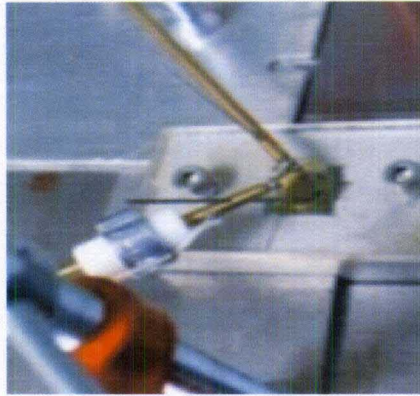


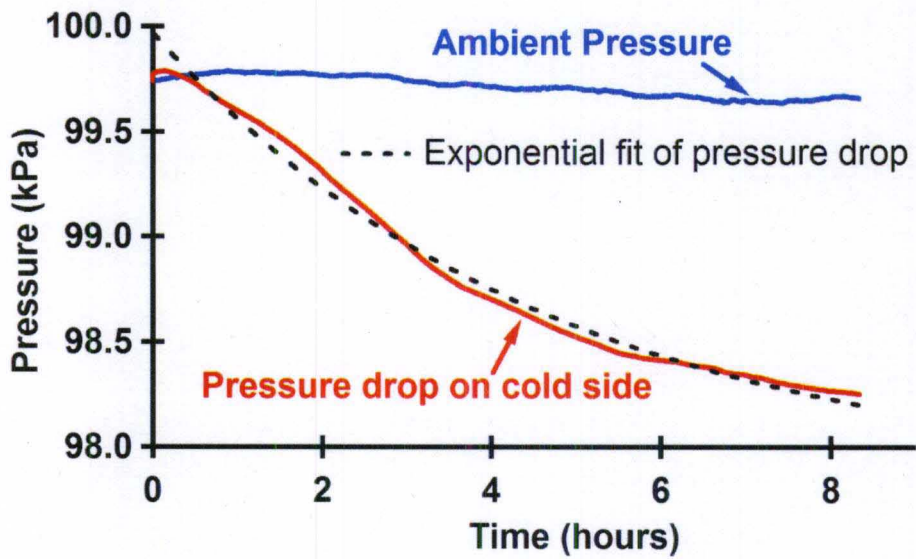
Figure 37. Optical microscope image of the actual silicon-silicon chip with suspended heaters for thermal isolation, (a) the bottom silicon substrate without the top cover showing heater elements, cold side opening and support pillars, (b) showing the top silicon substrate being bonded over the etched channel.

heater surrounded by air [65-67]. In this case, the whole pump was made out of silicon including the heater and the top cover. The suspended heaters were made of boron doped silicon and etched by SCREAM process in the DRIE [68]. The heater geometry was also revised from the previous design by making it serpentine rather than straight bars. Ordinary differential equation with imposed boundary conditions shows that in a straight bar resistive heater the heating is not uniform rather it follows a bell curve with higher temperature in the center and lower on the ends. This will cause unequal heating of the channel's hot side and will hinder in thermal transpiration and flowrate. This problem was eliminated with the serpentine design since the straight bar is folded in the form of serpentine structure with the fold carrying the maximum temperature facing the channel opening for uniform heating of the hot end, shown in *Figure 36(a)*. The fabricated heater trace SEM cross sectional image is shown in *Figure 36(b)*. The channel length is several hundred micrometers in each of these designs. The optical images of the chip are shown in *Figure 37*. Like the earlier process in 4.1.1 this process flow is similar except that bonding is on a wafer level and both the top and bottom substrates are made of silicon. The high thermal conductivity of silicon material could not maintain a significant temperature gradient for efficient pumping as is seen in the graph of *Figure 38b*. The pump suffers in flowrate and takes a long time to evacuate the dead volume of the sensor. The pump has been tested only in the pressure mode by using two sensors one to measure the ambient pressure and the other to monitor the pressure at the cold side of the pump. The net difference of these two sensor readings indicates the actual pressure drop obtained by the pump. In *Figure 38b* the sensor graph follows and exponential decay fit of the same. Due to small conductance to gas flow in the channel, the time it took to

attain the stable point is very long during which the variation in the ambient pressure causes the pressure sensor curve to deviate from a smooth exponential decay curve.



(a)



(b)

Figure 38. (a) The experimental set up used to test the pump chip. Power is provided to the heater pads on the chip through the probes and the cold end of the channel is coupled to a pressure sensor not shown in the figure(a), (b) the graph obtained with pressure drop at the cold end versus time.

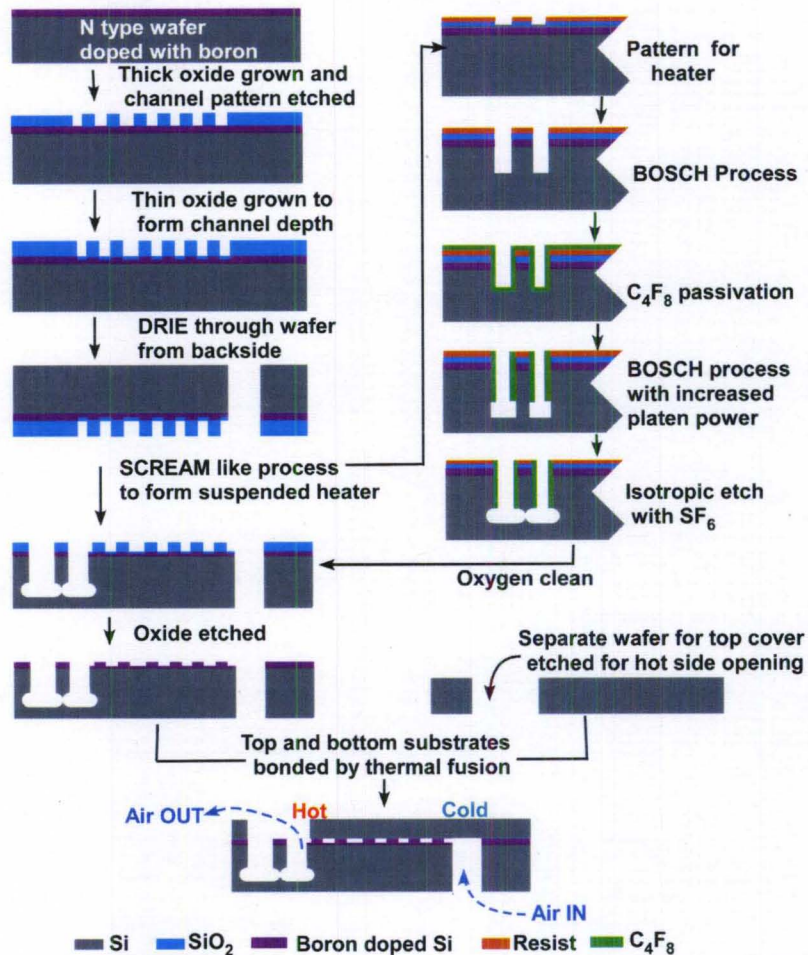


Figure 39. Fabrication process for the Si-Si lateral pump, separately showing the SCREAM like process.

The fabrication process development involved four masks shown in Figure 39. An n type wafer was selected and then one side was made p type by using spin on dopant. PB 20 F was spun at 3000 rpm and then baked at 200C for 15 min. The wafer was then put in the furnace at 1000C for limited source diffusion for 2 hours. Then a thick oxide was grown by performing a wet oxidation and simultaneously patterned for channel region and supporting pillars. This oxide layer will serve as a sacrificial layer and help in keeping the wafer surface clean for bonding. The intermediate processes of etching using DRIE will otherwise leave a polymer coating which is difficult to remove from silicon

[69]. The wafer was then subjected to dry oxidation where a 100 nm thin oxide film was grown. By the principle of oxidation, this oxide growth will use up the silicon in the open places to form silicon dioxide and thus reduce the height of the silicon in those areas by around 50 nm. The other places silicon will not be attacked due to thick oxide protection. Thus a channel height of around 50 nm was formed. The backside of the wafer is patterned using photoresist for the opening of the pump channel to the cold side. The opening was made by etching through the wafer using DRIE from the backside.

A SCREAM -Single crystal reactive etching and metallization, like process [68] was used in the DRIE to etch the free standing heater elements. This process uses normal BOSCH process to etch down the heater height, and then uses only passivation, gas C_4F_8 , to coat the sidewalls and the bottom floor, then uses a higher platen power BOSCH process to etch deeper and not affect the sidewalls, finally it uses only SF_6 to make an isotropic etch to free the structures. The bond pads due to larger dimensions in the mask layout do not free totally but get undercut. The p-doped wafer form p-n junctions at the bond pads. When the pads are supplied with voltage the p-n junction is in reverse biased condition and thus allows current flow only through the heater geometry in the p layer and not the n layer, thus electrically isolating the heater from the rest of the device. The top cover for the channel enclosure is prepared on another wafer by patterning and etching through the depth of the wafer to open the channel end at the hot side. The active bonding surface on both the wafers is protected by oxide layers till all the above mentioned DRIE processes are finished. Thus the oxide acts as a sacrificial layer which can be etched away after the DRIE and with it will be removed all the organic deposition from the wafer after the DRIE. Now, the wafer surfaces are ready for bonding after the

RCA clean. The bottom and the top wafers are aligned using the bond aligner and then the set is clamped and pre bonded in the wafer bonder. After the pre-bond the wafer set is permanently bonded by silicon fusion bonding in the furnace at 1000C for 1 hour [70]. The spacing of the supporting pillars was designed so as to prevent the collapsing of the top substrate onto the bottom substrate [71]. The wafer is then diced to get individual pumps.

It is apparent after both the results from Sections 4.1.1 and 4.1.2 that silicon is not the right material for the channel. If a material which has lower thermal conductivity than silicon and could be easily micro-machined is adopted then chances of increasing the efficiency of the pump using the lateral design become much higher as shown in the simulated graphs *Figure 40* for three different materials with two different substrate thickness using the similar lateral design as that of Section 4.1.2.

It is quite evident that the lower the thermal conductivity and thinner the substrates the higher is the temperature gradient along the channel. Also, the thickness of the top substrate or the channel cover plays an important role in maintaining the temperature difference. All these points were put together and analyzed in the following simulation model to come up with the right material and better design.

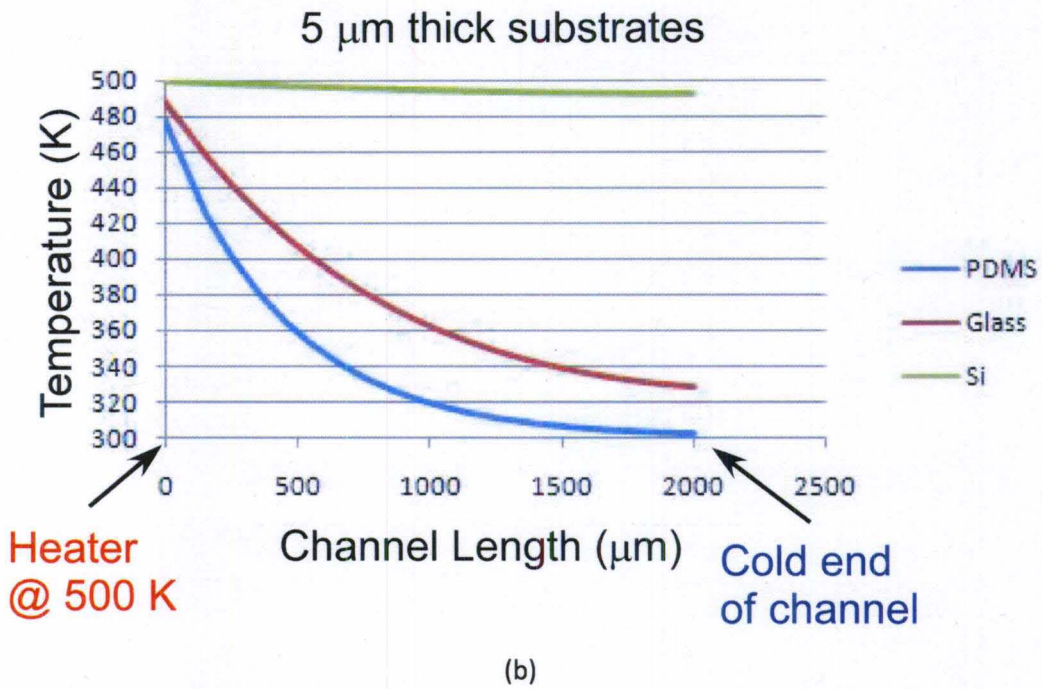
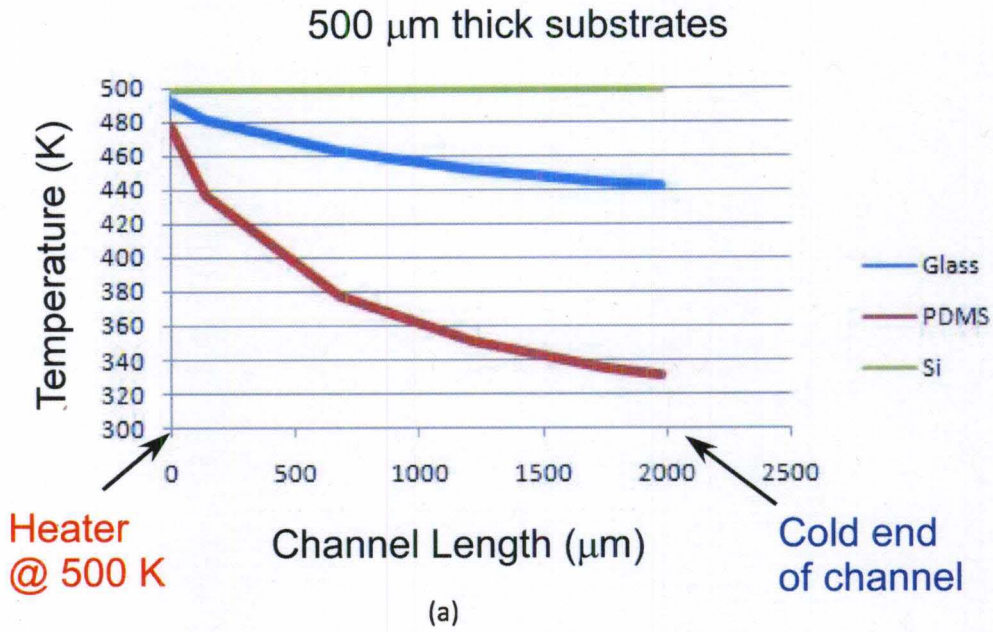


Figure 40. Longitudinal temperature distribution along the channel (a) when both top and bottom substrates are 500 μm thick, (b) when both top and bottom substrates are 5 μm thick.

Table 2. Results of the simulation:

Top-bottom substrates	Temperature hot side (K)	Temperature cold side (K)	Pressure ratios	Differential Pressure($P_{hot}=1atm$)
Si-Si (500 μm)	499.9	499.2	1.0007	0.0006
Si-Si (5μm)	499.6	491.6	1.0081	0.0008
Glass-Glass(500μm)	492.4	441.5	1.056	0.053
Glass-Glass(5μm)	488.7	328.4	1.219	0.18
PDMS-PDMS(500μm)	476.7	331.7	1.198	0.165
PDMS-PDMS(5μm)	477.9	302.8	1.256	0.204

The results in Table 2 summarize that a material with low thermal conductivity along with a thin top substrate is the best design for obtaining a high temperature difference along the channel. The silicon in *Figure 38b* gives a higher pressure drop compared to the simulated number in the above table, the reason behind that is in the simulation model the width of the channel is 1/50th that of the actual pump due to computer memory usage. The wide channel helps in better heat dissipation and thus attained a higher temperature gradient. Still, the pump is very slow compared to existing micro gas pumps and will not suit any potential applications.

4.1.3 Polymer micromachined pump

Based on the simulation results nanochannels made of polymer were found to be the suitable approach. Recent developments in NIL-nano imprint lithography has been

used by different research groups to make nanofluidic channels [72-79] and subnanometer features for IC industry.

Nano channels made of Polymer using nanoimprint lithography by hot embossing – Hot embossing processes include three steps, the first is heating and applying pressure step, the second is remaining temperature and pressure step and the third is de-molding step. Hot embossing can be performed isothermally or non-isothermally. The isothermal hot embossing means the substrate and mold will be heated to the same temperature during embossing process. In contrast, the non-isothermal embossing means the mold and the substrate will be heated to different temperature. 100 nm high channel moulds were made in silicon wafer using DRIE and then the same was coated with FDTS to make the surface hydrophobic for easy release of the mold at a later step and polycarbonate wafers

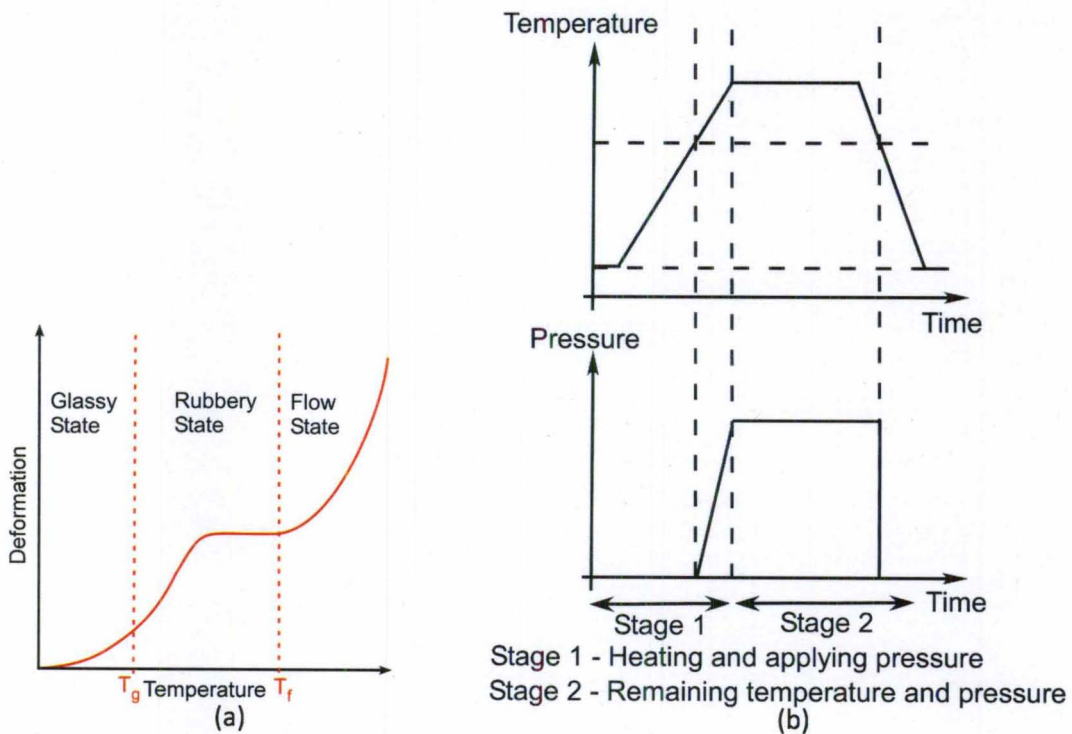


Figure 41. (a) Effect of temperature on deformation of polymers, (b) important stages in hot embossing.

were imprinted by the same in the SUSS bonder under vacuum in a temperature range above the T_g (glass transition temperature) of the Polycarbonate which is 150 C. Normally, a temperature around 50C higher than the T_g temperature was chosen. Above T_g , local motion of chain segments takes place and the modulus of the material drops by several orders of magnitude. However, the entire chains are still fixed by the temporary network of entanglements. A rubber-elastic plateau region exists beyond T_g , where a relatively large deformation may occur due to extension of chain segments fixed between entanglement points (*Figure 41a*). The modulus stays relatively constant in the rubbery state, and the deformation will recover after the force is released. Next is the rubbery flow region for linear amorphous polymers, but it does not occur for cross-linked polymers. Finally, with a further increase in temperature, the viscous liquid flow state is reached. In this regime motion of entire chains takes place and the polymer flows by chain sliding. The modulus and viscosity are further reduced in this region and the deformation is irreversible, which makes it the right temperature range for NIL patterning. A constant pressure was also applied during the bonding. The two stages of first applying the temperature over the T_g of the polymer and then the application of pressure forms the two important steps of hot embossing shown in *Figure 41b*. The nano imprint lithography on Polycarbonate was successful, the process steps of which are shown in *Figure 42a*. Then to enclose the channel on the top side PMMA was spun on a separate wafer. The wafer with PMMA spun on it and the imprinted polycarbonate wafer were aligned to each other with PMMA facing the polycarbonate and then a thermo-compression bonding technique was used to bond PMMA to polycarbonate. The bonding did not take place uniformly as some areas bonded while others did not

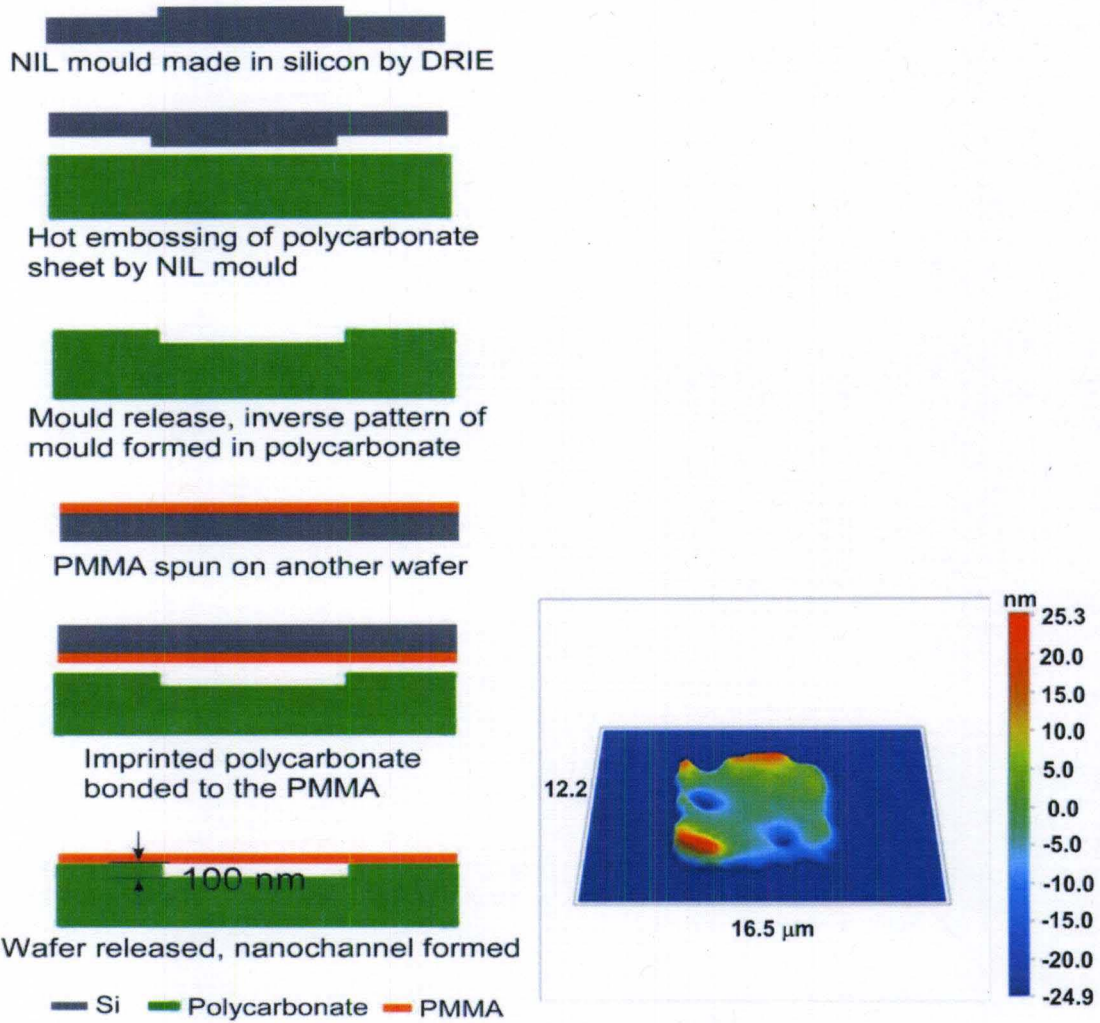


Figure 42. (a) Process steps for forming enclosed nano channels using hot embossing, (b) surface roughness scan of the hot embossed surface using optical profilometer.

bond. The reason was due to surface roughness during NIL which was determined by the optical profilometer image in Figure 42b.

Nanochannel made out of polyimide using aluminum as a sacrificial layer [80] – Polyimide PI 2611 processing was done on a wafer to form the base of the channel, process steps of which are shown in *Figure 43a*. Then aluminum was sputtered and patterned to define the channel geometry on it. Then another layer of polyimide was coated and processed. Then again aluminum film was sputtered as a masking layer to etch the polyimide and patterned at the channel openings. Dry etching was used to

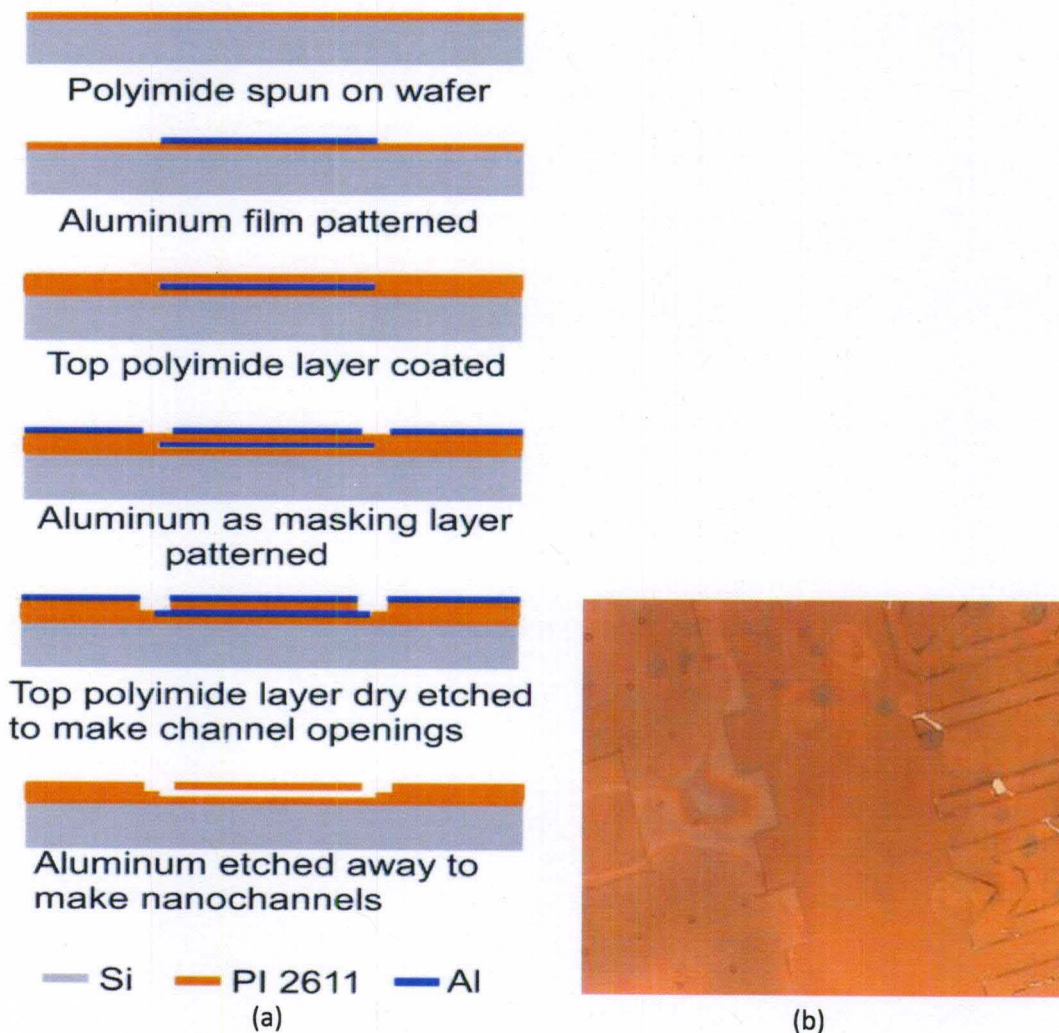


Figure 43. a) Process flow for making polyimide nano channels with aluminum as sacrificial layer, b) remains of aluminum in nanochannels after a week of etching.

perform the polyimide etching of the top layer near the channel openings to expose the aluminum forming the nanochannel. Then the whole wafer was left in aluminum etchant to etch away the aluminum and form the enclosed nanochannels whose height will be the thickness of first deposited aluminum film. This aluminum etch process takes a long time to etch away all the aluminum. The optical image of the polyimide channel shown in *Figure 43b* is after 7 days of etching and still some aluminum remains could be seen trapped inside the nanochannels. By the time all the aluminum is etched away the etchant finally starts attacking the polyimide too. Thus, this process was not successful.

4.2 Glass micro-machined microfluidic pump

With thermal conductivity of silicon as high as 150W/mK , a material which could be micromachined as well as has a low thermal conductivity value is glass. This pump design incorporates a nanochannel in conjunction with a micro channel shown in *Figure 44*. The heat source is not fabricated on chip rather supplied externally during the pump operation. Both the channels are etched on the bottom glass substrate and then the top lid

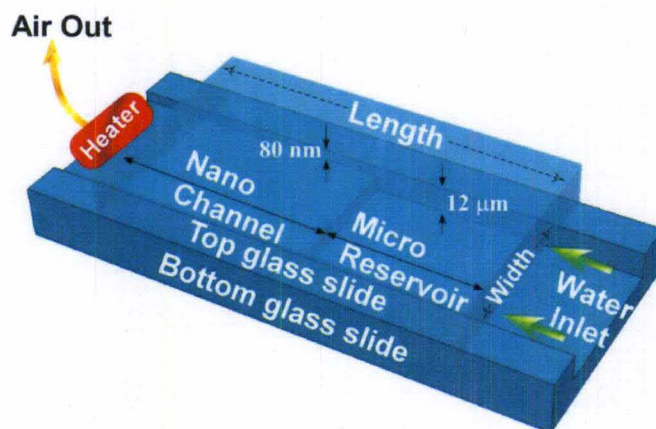


Figure 44. Schematic of the glass microfluidic pump. The nano channel used for thermal transpiration is in conjunction with the micro reservoir into which water is being pumped.

is thermo-compression bonded. The reasons behind choosing glass for this design are low cost, ease of fabrication, easier inspection, good thermal isolation between hot and cold sides and flexibility in its integration with other lab-on-a-chip devices. The height of the nanochannel is 80 nm and the height of the micro channel is 12 micrometers. The nano channels are under thermal transpiration when a temperature gradient is applied across them. The water flows in the micro channels, not the nano channels. A hydrophobic treatment is used to repel water from the channels, which would otherwise fill due to the capillary forces. The pumping of liquid into the micro channels is attributed to thermal transpiration occurring in the nanochannels which generates a pneumatic pressure responsible for drawing the liquid into the channels. Thus, pneumatic pumping of liquids can be achieved using this pump which is the first of its kind for a Knudsen pump [81]. An on-chip micropump for pumping liquids has abundant applications ranging from its use on a lab-on-a-chip, mixers, biological assays, HPLC, PCR analysis, picoliter drug delivery and many others [82-86]. In the micro scale there are other forces that have to be balanced in order to obtain favorable pumping action [87-89]. The dynamic behavior of the meniscus is acted upon by gravitational force, viscous force, interfacial force, the inertial force and the force due to the pressure difference caused by thermal transpiration. The force due to inertia can be neglected for the water-glass system which is true in our case. The inertial force is accountable when the capillary radius is around 0.480 mm [90] which is a couple of orders in magnitude greater than the radius of the capillary we have used. The height of water that can be supported by the capillary forces is given by (4.1).

$$h = \frac{2\gamma\cos\theta}{\rho g d} \quad (4.1)$$

where ' γ ' is the surface tension of the liquid, ' θ ' is the contact angle with the wall, ' ρ ' is the density of the liquid, ' d ' is the hydraulic diameter of the capillary and ' g ' is the gravitational constant. The Knudsen pump will generate a pressure within the channel. Taking the ambient pressure at ' p_{amb} ' and the pressure in the channel as ' p_{ch} ' the following relationship can be found

$$P_{ch} = P_{amb} \sqrt{\frac{T_{ch}}{T_{hot}}} \quad (4.2)$$

where ' T_{ch} ' is the temperature at the boundary between a deep channel and a shallow channel etched into the glass and ' T_{hot} ' is the temperature of the hot end of the nano channel. The pressure on the water in the channel due to the Knudsen pump is the difference between the ambient pressure on the water reservoir ' p_{amb} ' and the pressure in the channel ' p_{ch} '. This is given by (4.3).

$$P_{pump} = P_{amb} - P_{amb} \sqrt{\frac{T_{ch}}{T_{hot}}} \quad (4.3)$$

At equilibrium, the sum of all the pressures on the liquid is zero. This is shown in (4.4).

$$\sum P = 0 = P_{pump} + P_{cap} - P_{grav} \quad (4.4)$$

where ' p_{cap} ' represents the capillary pressure and ' p_{grav} ' represents the gravitational pressure acting on the liquid. A hydrophilic surface cannot be used as the capillary forces and the forces generated due to thermal transpiration act in same direction. Thus a hydrophobic treatment was preferred on the glass channel surface in order to reduce the capillary forces. With a hydrophobic surface, the capillary height is still beyond that which will be achieved with a microfabricated device. Using a channel length that is less than the capillary height determined by (4.1) will result in all the water being repelled

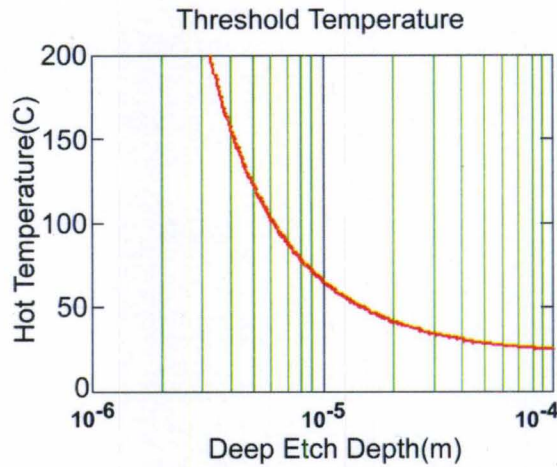


Figure 45. Variation of threshold temperature with micro reservoir depth.

from the channel. Thus initial 'h' may be assumed to be the (negative) depth that the channel is submerged in the liquid reservoir. The minimum temperature required to equate the capillary force with the pneumatic force can be found, using (4.4). It is given by (4.5). It can be termed as threshold temperature ' $T_{threshold}$ '.

$$T_{threshold} = \frac{P_{amb}^2}{\left(P_{amb} + \frac{2\gamma\cos\theta}{\rho g d} - \rho g h\right)^2} T_{ch} \quad (4.5)$$

Assuming that the cold temperature is room temperature, and assuming 'h' is nearly zero, Figure 45 may be obtained. A temperature higher than the threshold temperature will start to pump the water through the channel. From Figure 45, it is apparent that a threshold temperature of 65°C is required in order to raise the water through a micro reservoir of depth 10 μm .

4.2.1 Fabrication process development

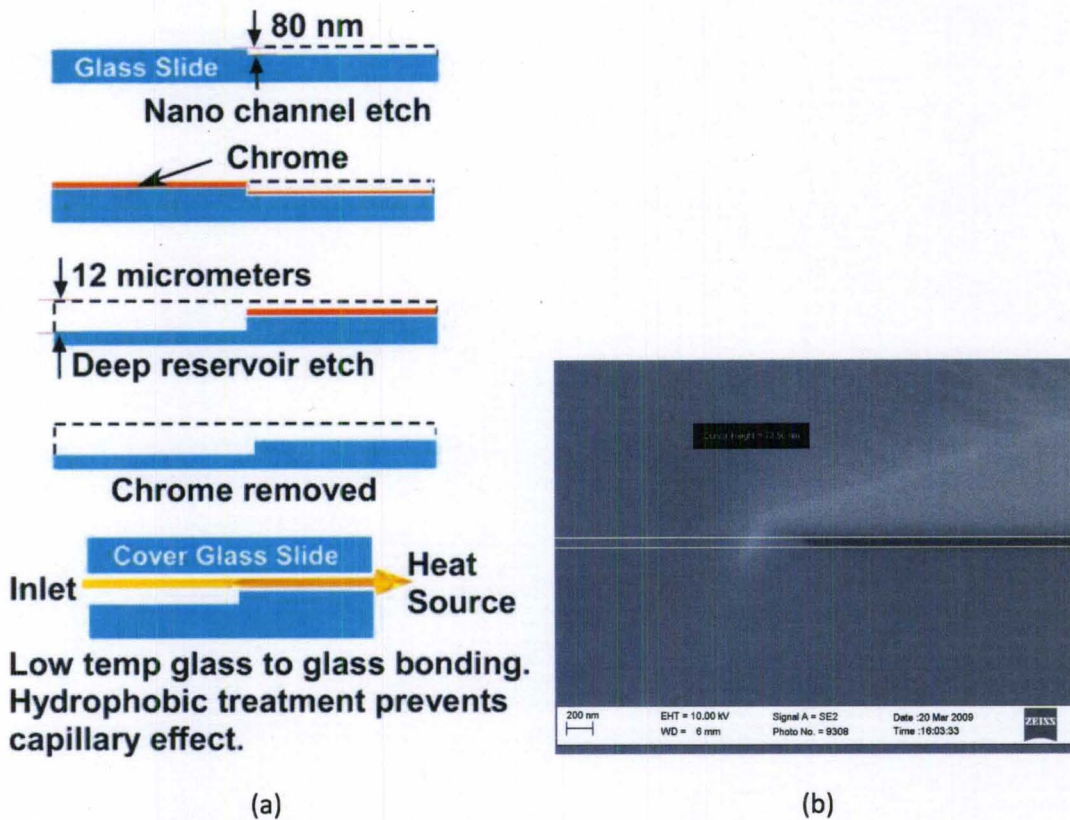


Figure 46. (a) Fabrication process flow for the glass pump showing both the nano channel and the micro reservoir etches and then glass to glass bonding, (b) SEM image of the nano channel fabricated in (a).

The fabrication process development of the Knudsen pump using microscopic glass slides involved two masks shown in *Figure 46a*. The microscopic glass slides were pre cleaned using acetone and methanol in order to remove any organic contaminants. The slides were rinsed in DI water followed by the nanostrip (Cyantek corporation) treatment at 90°C for 15-20 min. This step ensures that the slides are devoid of any organic contaminants that have survived acetone bath. The nanostrip treated slides were DI water rinsed and spin dried. Dehydration baking at 150°C for 30min would ensure that the slides are moisture free. S1813 photoresist was spin coated on the glass slides. The slides were exposed with the first mask. It defines the nano channel regions. A short oxygen plasma descum was carried out in order to remove any organic residue from the

nano channel defined regions. A dilute BOE treatment of these glass slides creates the nanochannels with 75 nm - 80 nm step height. This is shown in *Figure 46b*. The glass slides with the nano channels were subjected to acetone and methanol rinse followed by the nanostrip treatment. This removes the residue from the hard baked photoresist from the first mask process. After the dehydration bake the slides are sputtered with Cr. A second mask step is implemented on the patterned glass slides with the etched nano channels. The second mask defines the regions of the deep micro reservoirs. Chrome is etched from these regions with the photoresist as the mask exposing the underlying glass for the prolonged BOE etch. Microreservoir with 12 μm depth is formed during the prolonged BOE etch. Nanochannels are protected by the hardbaked photoresist and Cr. The hardbaked photoresist and Cr are completely removed for the subsequent glass-glass bonding. The glass slide with shallow nano channels and deep micro reservoirs are coated with hydrophobic coating in the molecular vapor deposition system. The monolayer coating was performed using FDTS (Perfluorodecyltrichlorosilane) at a pressure of 0.5 Torr along with water maintained at the pressure of 18 Torr. The total time of deposition is 300 sec. The temperature of the chamber is maintained at 35°C during the deposition. A low temperature glass-glass bonding was adopted in order to obtain the embedded nano channels. The bottom glass slide with the etched channels and reservoirs is bonded to the top glass slide, which acts as the cover glass. They undergo the calcium acetate pretreatment in order to activate the surface before bonding. The details of the pretreatment procedures are explained elsewhere [91]. The pretreated slides are hand pressed against each other and placed on the hot plate for 2 hours maintained at a temperature of 60°C. The temperature of the hot plate was then raised to 300°C with the

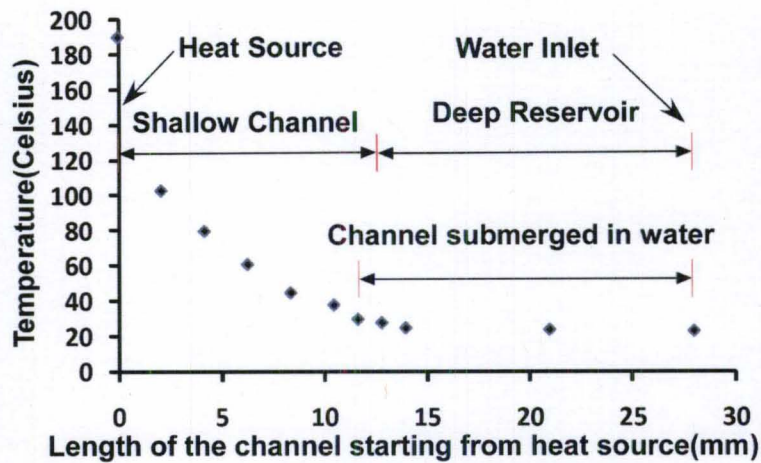


Figure 47. Measured temperature along the channel under thermal transpiration.

ramp up rate of 100°C/Hr. The dwell time at 300°C was 2hrs followed by the ramp down rate of 100°C/Hr. The cross section of the schematic of the bonded glass slides is shown in Figure 46b.

4.2.2 Results

The fabricated Knudsen pump was tested by keeping one end of the nano channel within the close proximity of the iron tip maintained at 550°F. The open end of the micro reservoir was immersed in water at room temperature. The outer side of the glass slide was contact probed using thermo couple tip along the length of the channel. Figure 47 shows the measured thermocouple readings which clearly depicts the established thermal gradient across the nano channel. From Figure 47, the temperature at the hot channel end on the glass slide is 190°C, but drops to 100°C at approximately 2mm from it. The temperature further drops to 20°C at the intersection of nano channel and micro reservoir. The temperature difference of $\Delta T = 170^\circ\text{C}$ between the two ends of the shallow channel

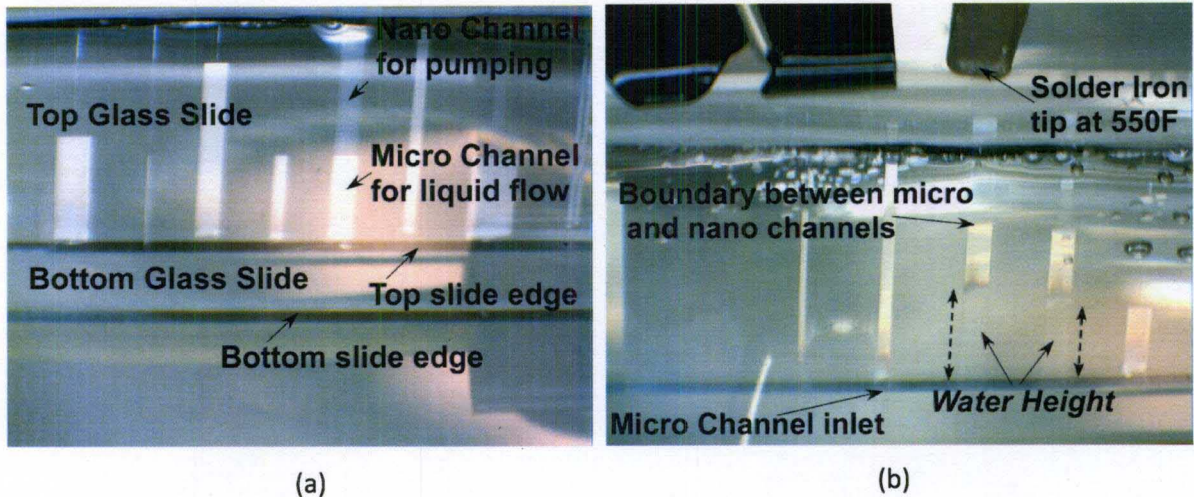


Figure 48. (a) As expected, the water level in the micro channels did not rise, as the connected nano channels are not in the proximity of the hot iron tip. (b) Successful pumping of the water in the micro channels when the connecting nano channels are under thermal gradient.

generates a pressure difference due to thermal transpiration. This ultimately causes the increase in the level of the water in hydrophobic coated micro reservoir.

Figure 48 (a&b) show the optical microscope pictures of the bonded glass slides immersed in water with the embedded channels between them. The channels are clearly visible due to the light interference between the top glass and the bottom etched glass. Figure 48a shows the edge of the glass slides not within the proximity of the hot iron tip. It is apparent that the hydrophobic coating on the micro reservoirs did not let the water flow inside them. Hence there is no change in the level of water. However, from Figure 48b, when hot iron tip was in close proximity to the nano channels, the level of water in the connecting micro reservoirs has increased.

The time required for the water in the micro reservoir to reach a certain height is influenced by gravity, capillary force, inertial force, viscous force and the force generated by the pressure difference of the pump. The experimental setup was left overnight with

the pump ON and next morning the water height in the microfluidic channels was observed due to pumping. So, the exact time it took for the water to rise in the channels was unknown. However, after a certain height there was no more increase in the height of the water in the channels even with the pump ON. At the steady state when all the forces are balanced there should be unrestricted pumping. The water height stagnating after reaching a certain level led to the conclusion that as the water was getting closer to the heat source it started evaporating and thus it was limited in further travel.

4.3 Thermal transpiration in porous polymer membrane

In Section 4.2 with the glass microfluidic pump, the rate of pumping has been observed to be very slow. As shown in Table 2, a polymer material is the best candidate to make the pump channels. In this section Knudsen pumps have been made out of mixed cellulose ester filter membranes obtained from Millipore Corporation. These membranes have 70-75 % porosity which is favorable for a high gas flow rate. Each pore forms an

Membrane pore size (nm)	Porosity (%)	Thickness (μm)	Knudsen Number (K_n) @ $\lambda = 60 \text{ nm}$
25	70	105	2.4
50	72	105	1.2
100	74	105	0.6
220	75	150	0.27
300	77	150	0.2
450	79	150	0.13
650	81	150	0.09
800	82	150	0.075
1200	82	150	0.05

Table 3. Porosity and membrane thickness for the different pore diameters of mixed cellulose ester membranes used.

individual pump and thus there is an increased conductance to gas flow since the filter membranes have numerous pores in them. The thickness of the membrane is 105 μm for the membranes with pore sizes 25 nm, 50 nm and 100 nm. The low bulk thermal conductivity of 0.16-0.36 W/m-K of cellulose esters can achieve a higher temperature gradient along the channels which enhances the flowrate of the pump. These membranes are flexible and robust and it is therefore easy to seal these membranes in place.

4.3.1 Pressure differential versus pore diameter

Knudsen pumps with different pore diameters are tested at constant power. The objective of this experiment is to find out how the pressure differential obtained at the cold end of the pump and thereby the flowrate varies with respect to the pore diameter of the thermal transpiration channel. A larger Knudsen number reduces the reverse pressure driven flow and is more favorable for achieving higher pressure ratio (P_H/P_C) for a given temperature ratio (T_H/T_C). Higher Knudsen number is obtained by making the pore diameter smaller compared to the mean free path. In physical terms this condition will

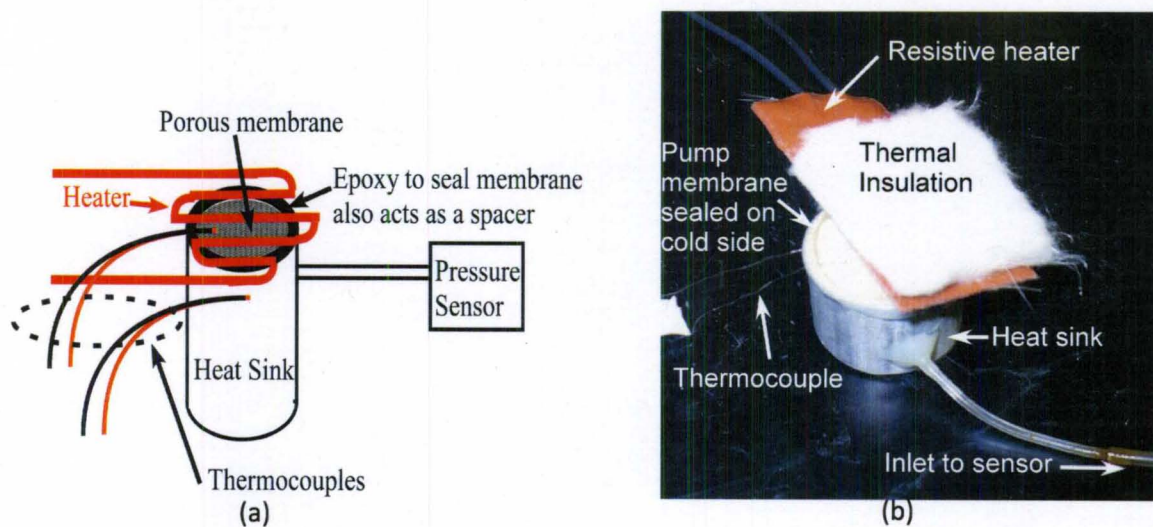


Figure 49. (a) Schematic of the experimental set up to establish the effect of channel size on thermal transpiration, (b) actual photograph of the pump used.

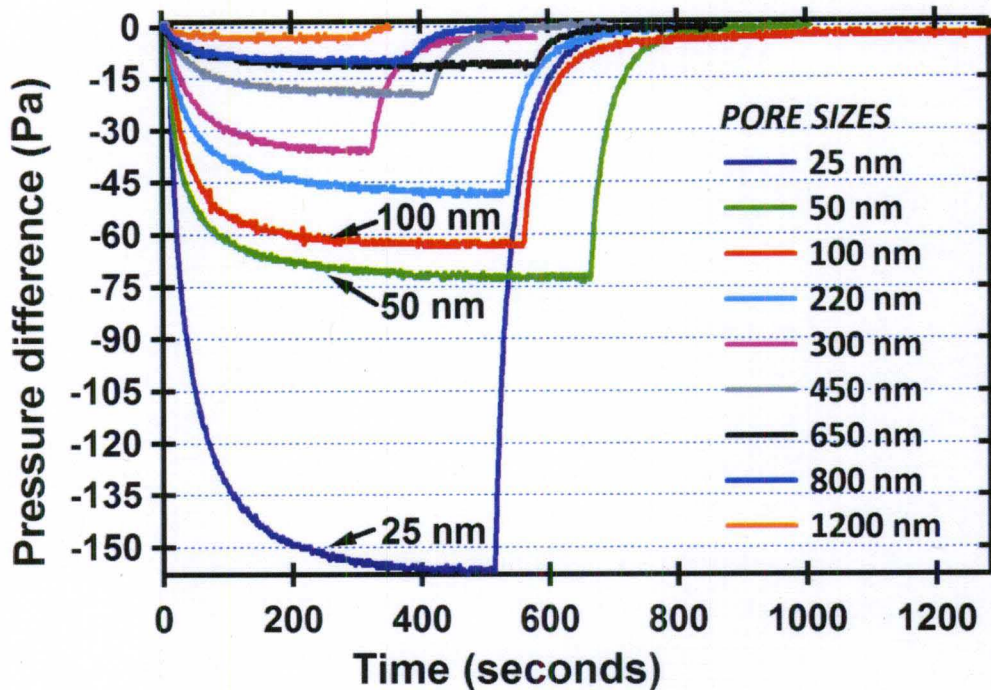


Figure 50. Plot of pressure drop on the cold side of the pump versus time measured for different pore sized membranes at 3.75 Watts of heater power. The pressure drop increases with decrease in pore diameter.

just have the gas molecules colliding with the channel walls and there will be minimum spacing for intermolecular collisions.

The setup to test different pores has been made by constructing a Knudsen pump using a resistive heater to heat the hot side as shown in Figure 49. The cold side is connected to the pressure sensor and another pressure sensor measures the ambient pressure. A Labview data acquisition program calculates the difference between the two sensors. To test each pore size, the membrane is changed on the pump and all other experimental conditions are kept the same.

All the membranes used in the experiment are 10 mm in diameter but the thickness of the membranes vary with their pore sizes. See Table 3. The membranes used are obtained from Millipore Corporation. The smallest pore sizes of 25 nm, 50 nm and

100 nm are all 105 μm thick. The larger pore size membranes are thicker than all 150 μm thick. At 1200 nm, the Kn is 0.05 which is near to the viscous flow regime.

The pressure difference as a function of time is plotted in *Figure 50* for all nine pore diameters investigated. The maximum pressure difference obtained follows descending order with an increase in pore size. The thicker membranes should have a higher temperature difference across them but due to larger back pressure flow the pressure difference obtained is lower than the smaller pore size membranes. So, even though the membranes are not of same thickness but still the experiment is able to prove the concept of variation of pressure ratio with respect to pore diameter. The measurements are done at a constant heater power of 3.75 W for which the hot side temperature of the membrane is 65.3 C and the cold side temperature on the sink is 49.3 C. These temperature measurements are approximate and not precise since the thermocouple on the cold side does not touch the membrane rather measure the sink temperature. So, with a thicker membrane due to the thermal resistance of the material the cold side temperature will be less compared to that of a thinner membrane. The sink temperature is same for all measurements since the heat convection from the heater to the sink dominates the heat conduction through the membrane. The maximum pressure differential is obtained with the 25 nm pore size membrane and is well explained by the theory. The pressure drop due to thermal transpiration at lower Knudsen numbers is smaller compared to those with higher Knudsen numbers as is shown in *Figure 50*. Thermal transpiration is found to be present for much larger channel diameters than expected. This can have important implications for MEMS devices that have temperature variations on them.

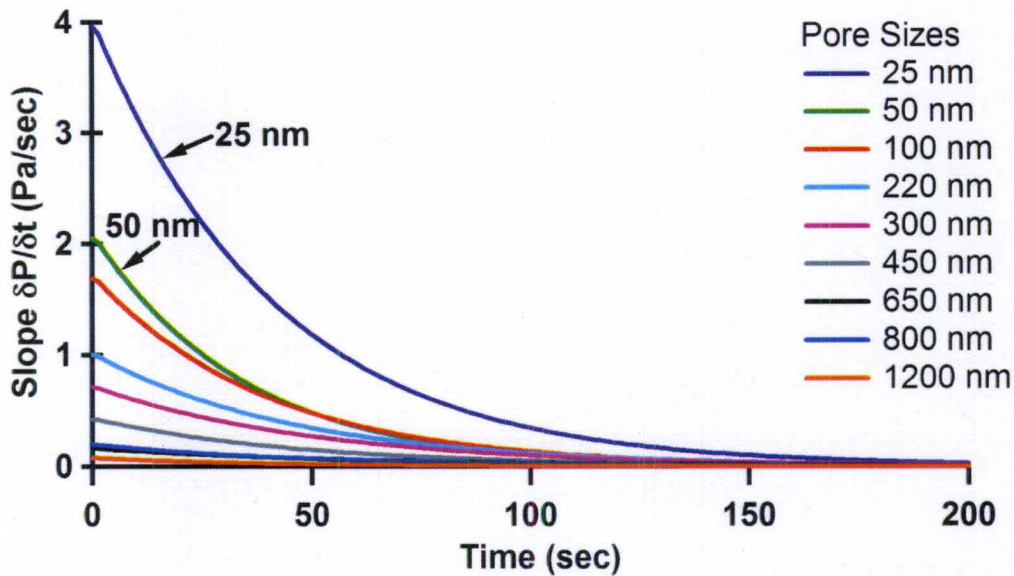


Figure 51. Plot of slope of pressure drop on the cold side of the pump versus time measured for different pore sized membranes at 3.75 Watts of heater power. The slope increases with decrease in pore diameter, which means the pumping is faster with smaller diameter channels.

This validates the theory that as the pore size reduces the pressure driven flow is more restricted and thus the net flow is dominant by thermal transpiration driven flow which produces a higher differential pressure. For smaller pore sizes with higher Kn there is a very little pressure driven flow. The slope of the pressure differential curve, which is proportional to the flow rate, is shown in *Figure 51*. This graph shows that 25 nm pore will produce the largest flowrate.

CHAPTER 5 – KNUDSEN PUMP USING PASSIVE POWER

5.1 Pump Designs

This Knudsen pump was designed to operate using either human body heat or solar heat to maintain the temperature difference along the nano channels. Without using any active heating element, the renewable energy from solar power or body heat is used to heat the hot side of the pump channel. A nanoporous channel matrix made up of different thermally conductive materials has been examined to determine the best performance for this type of operation. The design of the pump is very simplistic in nature. It consists of a thermal mass which acts as a heat collector for the solar powered pump and as a heat sink for the human powered pump. *Figure 52a* shows the schematic

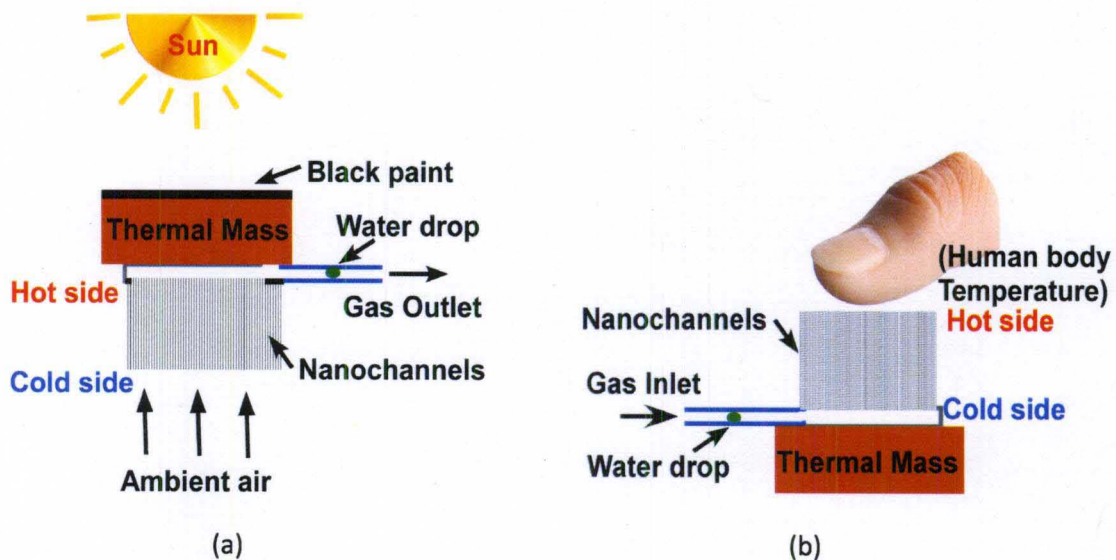


Figure 52. (a) Schematic of solar powered Knudsen pump, (b) schematic of human power Knudsen pump.

of the solar Knudsen pump. The sun heats up the thermal mass which develops a hot side of the nano channels, and gas is pumped from the cold side to the hot side, which is directionally away from the pump. *Figure 52b* represents the human powered Knudsen pump. On this pump body heat creates the hot side on one end of the channels and the heat sink keeps the other end at a lower temperature than the body temperature. The gas flows toward the pump with this setup.

5.2 Types of materials used in porous membranes

Three different types of nano channels were investigated: mixed cellulose ester membrane filters, silica aerogel from Aerogel Technologies, and silica colloidal crystals. For an efficient Knudsen pump, a low thermal conductivity is desired. The temperature difference is $\Delta T = \dot{Q}t/\kappa$, where \dot{Q} is the heat flux, t is the thickness of the nanoporous material, and κ is the thermal conductivity of the nanoporous material. For small temperature differences, the pressure and flow rate are both proportional to the temperature difference. Aerogel has the lowest thermal conductivity at 0.017 W/m-K [120], while bulk silica's thermal conductivity is about 1.4 W/m-K [122], and the mixed cellulose ester's thermal conductivity is about 0.16-0.36 W/m-K [121]. The aerogel is purchased from Aerogel Technologies, the mixed cellulose ester filter membranes from Millipore and the colloidal silica crystal samples are obtained from Dr. G. Sumanasekera at the University of Louisville. The colloidal silica crystal samples have been made by Zakhidov et al, at University of Texas at Dallas. They are grown using slow sedimentation of monodispersed aqueous silica colloids in a glass cylinder, followed by sintering at 700°C – 750°C for several hours [92]. The resulting crystal consists of closely packed, interconnected silicon dioxide spheres arranged in a face centered cubic

lattice with interconnected octahedral and tetrahedral voids between spheres. The silica colloids used in this experiment have average sphere diameters of 300 nm and octahedral and tetrahedral voids of approximately 120 and 60 nm in diameter, respectively. The voids are interconnected by narrow regions that are 10–20 nm in diameter. These voids form the channels for thermal transpiration gas flow.

The length of the nano channels is also an important consideration. The longer the channel, the greater is the temperature difference that can be obtained for a given heat flux, which creates a greater pressure difference. The cross sectional area of the nanoporous material used affects the flow rate of the pump, due to the increased number of nano channels within the area. Both aluminum and copper, which have high thermal conductivities, have been used as thermal masses for use as a heat sink with the human powered pump and as a heat collector for the solar powered pump. For the solar powered pumps the performance of the pump is also tested by using solar heat collecting black paint on the thermal mass, because the paint is believed to harness more solar radiation and create a greater temperature difference. The black paint Thermalox® Solar Collector Coating, 250 selective black is used. The paint is meant to collect heat more efficiently, by collecting wavelengths of light with the most heat content.

5.3 Testing of Pumps

The pumps are tested in both pressure and flow mode. Pressure mode testing method is similar to that described in Chapter 4. For the flow mode testing the velocity of a water droplet is monitored in the inlet of the pump. For the human powered pump the inlet is connected to the cold side of the pump which means the water droplet moves towards the pump when body heat is applied to the pump whereas for the solar powered

pump the inlet is connected to the hot side of the pump which means which means the droplet moves away from the pump when subjected to solar power. Due to fragile nature of aerogels the human body power test could not be carried out on them. The short channel length of the 105 μm cellulose ester membranes did not make efficient pumps and thus could not be tested in flow measurement mode. It is still probable that the pumps worked, but at a scale below the measurement minimum detection level. The results from pressure and flow measurements show that the silica colloidal crystal performed the best as both a solar and human powered pump. The maximum pressure drop obtained is 414 Pa for the solar powered pump and 1500 Pa for the human powered pump. With flow rate measurements the solar powered pump measured a maximum flow of 136 $\mu\text{L}/\text{min}$ while the human powered pump measured 17 $\mu\text{L}/\text{min}$.

CHAPTER 6 – THERMOELECTRIC POWERED BI-DIRECTIONAL KNUDSEN PUMP

This design uses a thermoelectric material in the form of a peltier module to create a temperature difference between the hot and cold ends of the channel. This design due to symmetry eliminates the need of a heat sink for the cold side and thus makes the pump bi-directional in operation [15]. In many applications, such as filtration, by-pass medical devices, and micro total analysis systems, it is desired to have a pump that is bidirectional [17]. The cold side temperature of the channel could be actively controlled and thus a more efficient pump is made by obtaining a larger temperature difference over a smaller channel length. The cold end of the channel could be kept colder more than normal unidirectional pumps and thus the net flux of molecules moving from the cold to the hot side of the pump is more in this design compared to others. Two different geometries are demonstrated, the lateral and the radial pump.

6.1 Lateral and radial pump designs

In *Figure 53a*, a thermoelectric module is thermally coupled to a nanoporous material with the use of a top and a bottom copper plate. The temperature difference across the nanoporous material causes a gas flow due to thermal transpiration. An inlet and outlet are formed on either side of the nanoporous material. This design will be referred to as the *lateral pump design*. The manufacturing process is shown in *Figure 53b*. In *Figure 54a*, a thermoelectric module in the shape of a ring is thermally coupled

to a nanoporous material with the use of a top and bottom plate. This design will be referred to as the *radial pump design*. The manufacturing steps are shown in *Figure 54b*. For both of the designs, when the thermoelectric is powered on, one face gets hotter and the other face gets colder. The plates serve as heat spreaders to transfer thermal energy from both faces of the thermoelectric module to either side of the nanoporous material, and thus control the hot and cold end temperatures of the channels. Gas is pumped from the cold side inlet to the hot side outlet due to thermal transpiration. For a 100 nm pore size channel over a temperature range of 280°K-380°K, the K_n is between 0.53 and 0.72 while for a 50 nm pore size channel over the same range of temperature the K_n is between 1.07 and 1.45. Thus all the experiments were conducted in the transition flow regime.

Insulating the pump with a low thermally conductive material will help lower the heat losses to the environment. The radial pump design has no thermal

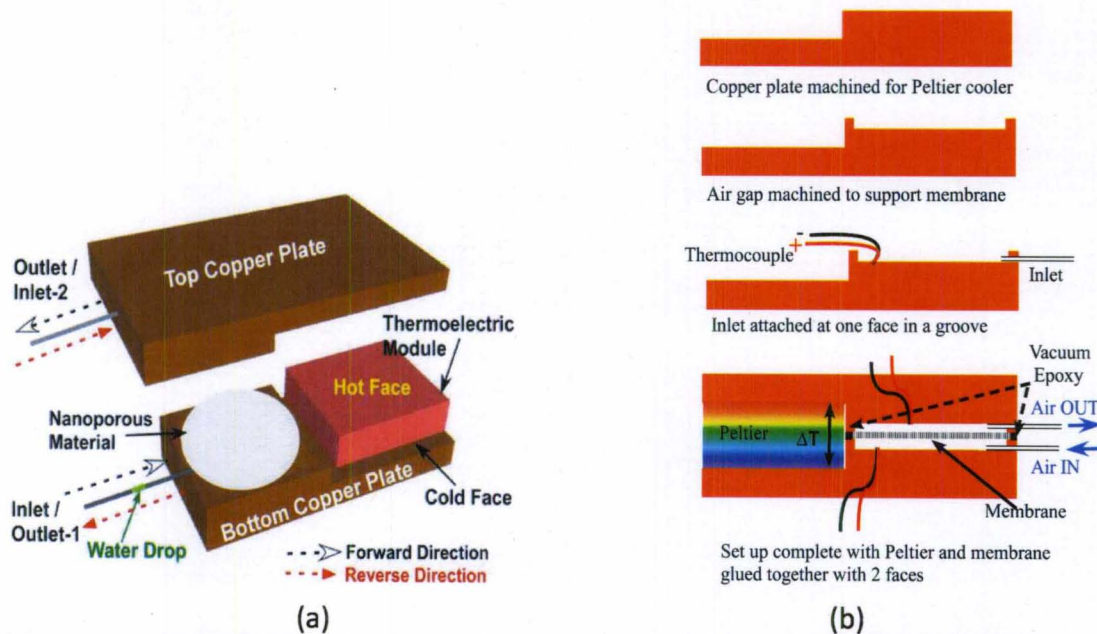


Figure 53. (a) Schematic of the bidirectional Knudsen pump using the lateral design, and (b) manufacturing steps of (a).

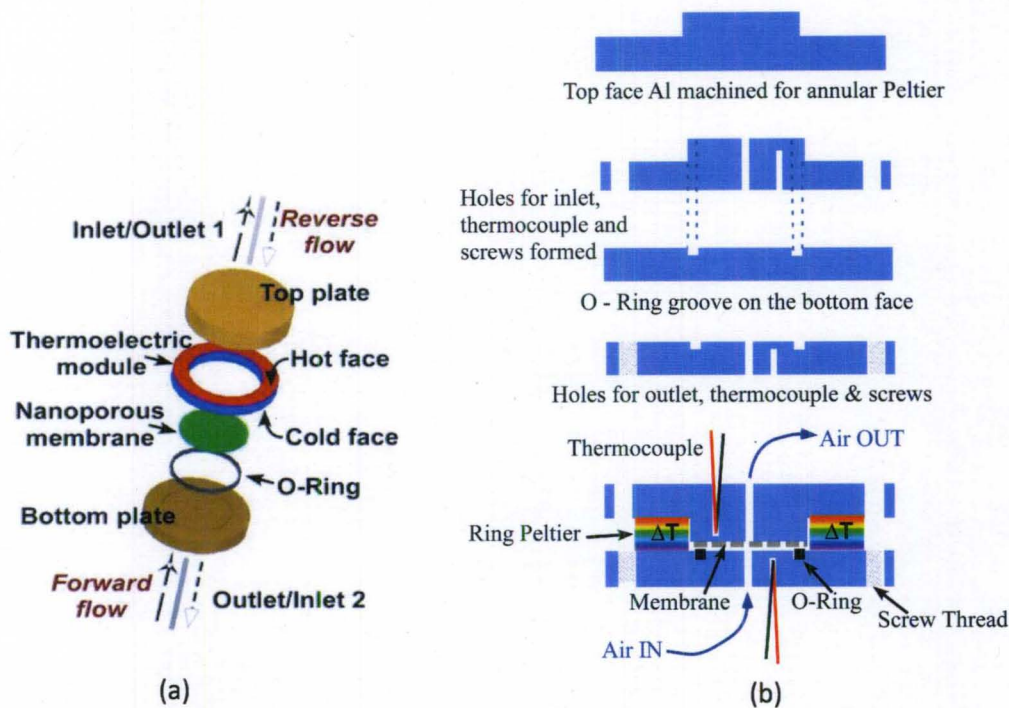


Figure 54. (a) Exploded view of the bidirectional Knudsen pump using the radial design, and (b) manufacturing steps of (a).

insulation and the lateral pump design has plastic sheets that help insulate it. Each device has two thermocouples (Omega Engineering, Inc- part# CHAL-005) embedded in them; one for the hot side and one for the cold side. Plastic tubes with ID 1/32 inches from Tygon Microbore Tubing, USA are used for the inlet and outlet of the pump.

In the lateral pump design, the copper plates are 5 mm thick, the nanoporous material is 1 mm thick, the air gap between the nanoporous material and copper is 100 micrometers, and there is a 500 micrometer wide ring of copper supporting the nanoporous material that also acts as a gas seal. The nanoporous material is Mixed Cellulose Ester obtained from Millipore Corporation, USA. The nanoporous material comes as 105 micrometer thick sheets, has a 50 nm pore size, and was cut to the desired shape and stacked to obtain 1 mm total thickness. The dimensions of the thermoelectric

module (Custom Thermoelectric, USA) is 8.4 mm on each side and 2.3 mm in height. The ZT value of the material used in the thermoelectric at 300K is 0.804.

In the radial pump design, the shape of the thermoelectric module (TE Technology, USA) is an annular ring which encloses the nanoporous material. The thermoelectric module used has an outer diameter of 24 mm, an inner diameter of 9.8 mm, and is 3.1 mm thick. The ZT value of the material used in the thermoelectric at 300K is 0.795. The nanoporous material is Mixed Cellulose Ester obtained from Millipore Corporation, USA. The nanoporous material is 5/16" in diameter, 105 micrometers thick, and has a 100 nm pore size shown in *Figure 55*. The maximum operating temperature of this polymer material is reported to be between 75°C and 130°C [93, 94]. The maximum operating temperature limits the maximum achievable pressure drop and flow rate of the pump. To simplify the machining in a machine shop, the top plate is flat, the bottom plate has most of the topography variation, and the top and bottom plates are made from 1/4" thick aluminum sheets because aluminum is

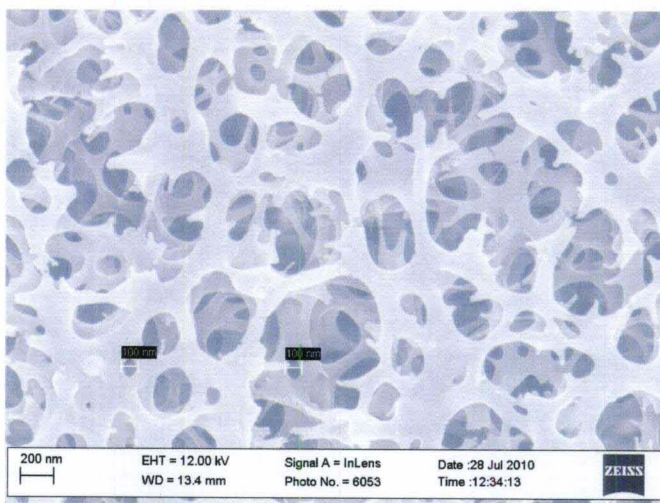
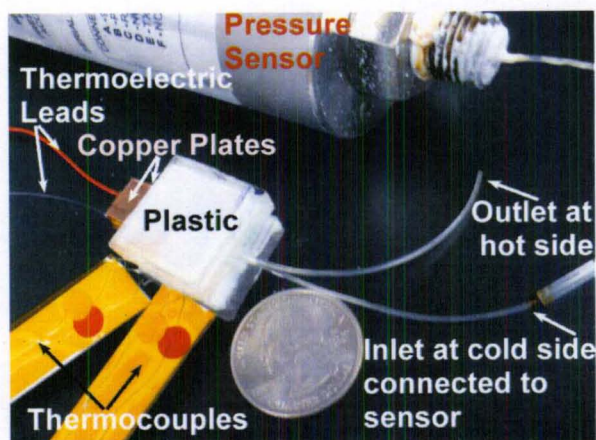
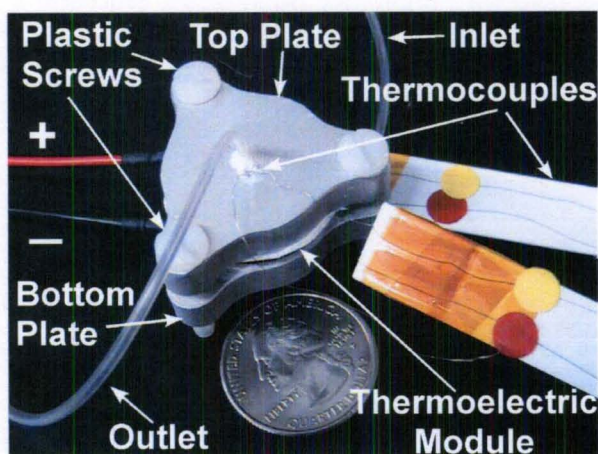


Figure 55. SEM image of the 100 nm mixed cellulose ester membrane showing nanopores.



(a)



(b)

Figure 56. Photographs of the actual pumps – (a) lateral pump design, and (b) radial pump design. A United States quarter (approximately 24.3 mm in diameter) is used for size comparison.

significantly easier to machine than copper. The bottom plate includes a groove to hold an O-ring. The O-ring creates a small air gap between the nanoporous material and the bottom plate. The size of the gap depends upon the tightness of the screws. The design depends upon the roughness of the top aluminum plate to permit gas to flow above the nanoporous material. Holes 1.5 mm diameter were drilled in the center of the aluminum plates for gas flow. Thermal grease from TE Technology, USA is used between the plates and the thermoelectric faces to maximize heat transfer to the plates. The two plates

are connected by plastic screws to seal the nanoporous material. The plastic screws minimize heat conduction from the hot plate to the cold plate. The photograph of lateral pump is shown in *Figure 56a* and that of radial pump in *Figure 56b*.

6.2 Simulations

Simulations of the devices were performed using CoventorWare to model the temperature distribution of the devices. Thermal conduction was used to simulate the thermal transport in the solid materials. Thermal transport due to free convection of air at a pressure of 10^5 Pa was simulated using a built-in computational fluid dynamics (CFD) module. The heat flow due to the gas pumping was neglected in the simulations because the gas flowing through the nanoporous material is in the transition flow regime, which is difficult to properly simulate. The boundary conditions for the simulations use a temperature of 285°K on the cold side of the thermoelectric, 355°K on the hot side of the thermoelectric, and 298°K on the outer-most air boundary. The fixed temperature boundaries alleviate the need for accurate modeling of the thermoelectric. The thermal conductivities of the materials used in the simulation are listed in Table 4.

Table 4. Values of thermal conductivities used in the simulations.

Material	Thermal Conductivity ($W/m \cdot K$)
Aluminum	273
Air	0.02
Thermoelectric	1.2
Nanoporous material	0.15
Copper	398
Polymer cladding in lateral simulations	0.12

6.2.1 Lateral Pump Simulation

Figure 57 shows the simulated temperature distribution of the lateral pump design. The dimensions of the membranes used in the simulations match the membranes used in the actual devices. In *Figure 58a*, a large temperature change can be seen for the top copper plate, while the bottom copper plate remains nearly uniform in temperature. Also shown is the temperature distribution along the top (HH', from *Figure 57*) and bottom (CC', from *Figure 57*) surfaces of the nanoporous material, and the temperature difference at each point. The air gap between the copper and nanoporous material helps maintain the temperature difference by reducing the rate of heat flow through the nanoporous material. The dip in the temperature difference at the 1 mm and 10 mm mark from the thermoelectric edge is due to the copper support ring, where there is no air gap between the copper and nanoporous material. Where there is no air gap, the hot side temperature is reduced and the cold side temperature is increased resulting in a smaller temperature difference. The effect is more pronounced in *Figure 58b* since the membrane separating the hot and cold side plates is just 105 micrometers thick. The temperature difference varies by a factor of 2.5, ranging from 50 K near the thermoelectric to 20 K at the farthest point from the thermoelectric. In *Figure 58b*, the temperature distribution along the nanoporous material is plotted for a substantially thinner, 105 micrometer thick, nanoporous material. Here, the temperature difference across the nanoporous material ranges from 20 K to nearly zero K, with an additional temperature difference dip to nearly zero K at the 1 mm mark due to the copper ring. Comparing *Figure 58 (a&b)*, it is clear that a thick nanoporous material is required to maintain a large temperature difference, and the fabricated device uses a thickness of 1 mm.

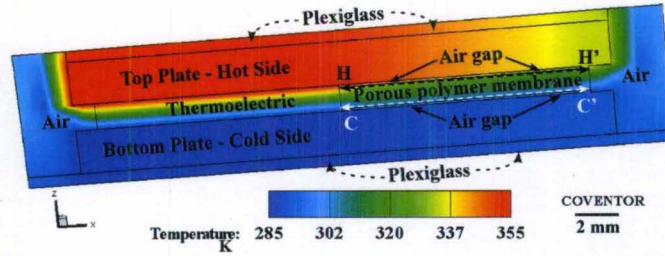


Figure 57. Simulation output from CoventorWare showing the temperature distribution of the lateral pump design with a 1 mm thick nanoporous material layer. The simulation modeled thermal conduction through the copper and nanoporous material layers, and used CFD to simulate convective thermal transport through the air layers. A 2D slice is shown from the 3D model. HH' and CC' are the traces where the temperature has been extracted on the hot and cold faces respectively for the data of Figure 58.

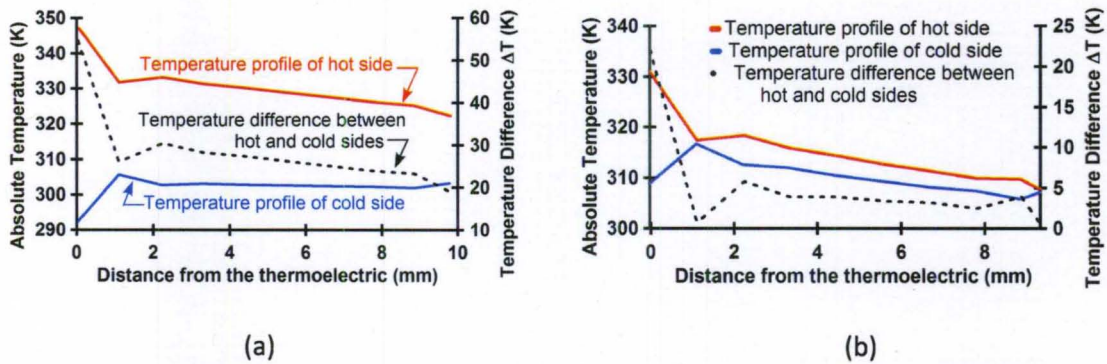


Figure 58. Comparison of the temperature distribution along the top (line HH in figure 57) and bottom (line CC in figure 57) surfaces of the nanoporous material obtained by simulation. In (a), a 1 mm thick nanoporous material is used, and in (b), a 105 μm thick nanoporous material is used. The 1 mm thick nanoporous material shows a substantially greater thermal difference. For the 105 μm thick nanoporous material, the temperature difference drops to nearly zero near the points at $x = 1$ mm and 10 mm where the nanoporous material is supported.

6.2.2 Radial Pump Simulation

Figure 59 shows the simulated temperature distribution of the radial pump design. Because the air gap between the nanoporous material and the aluminum plates is set by

the compression of an O-ring and is therefore unknown, an air gap of 1 μm was used in the simulation. The air gap set by the material roughness was simulated by assuming contact is made everywhere. The temperature is fairly uniform except at the center, where the holes are drilled. *Figure 60* shows the temperature distribution along the top (HH', from *Figure 59*) and bottom (CC', from *Figure 59* surfaces of the nanoporous material. The temperature difference is greater than 60 K for the entire nanoporous material, except where the holes are drilled in the aluminum, where the temperature difference drops to zero. The radial thermoelectric dimension used in the simulation is less than that used in the actual device to reduce memory consumption during simulation as the lateral thermoelectric dimensions do not significantly influence the outcome of the simulation.

Overall, the radial pump design supports a higher temperature difference across the nanoporous material than the lateral pump design, even with a much thinner nanoporous material (105 micrometers versus 1 mm). The temperature uniformity of the

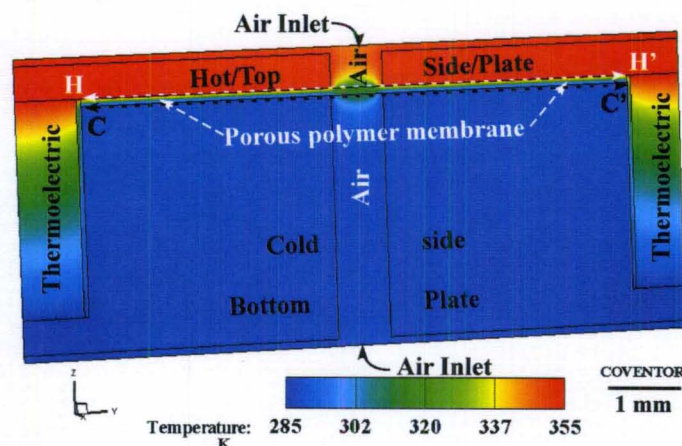


Figure 59. Simulation output from CoventorWare showing the temperature distribution of the radial pump design with a 105 micrometer thick nanoporous material layer. The simulation modeled thermal conduction through the copper and nanoporous material layers, and used CFD to simulate convective thermal transport through the air layers. A 2-d slice is shown from the 3-d model. HH' and CC' are the traces where the temperature has been extracted on the hot and cold faces respectively for the data of Figure 60.

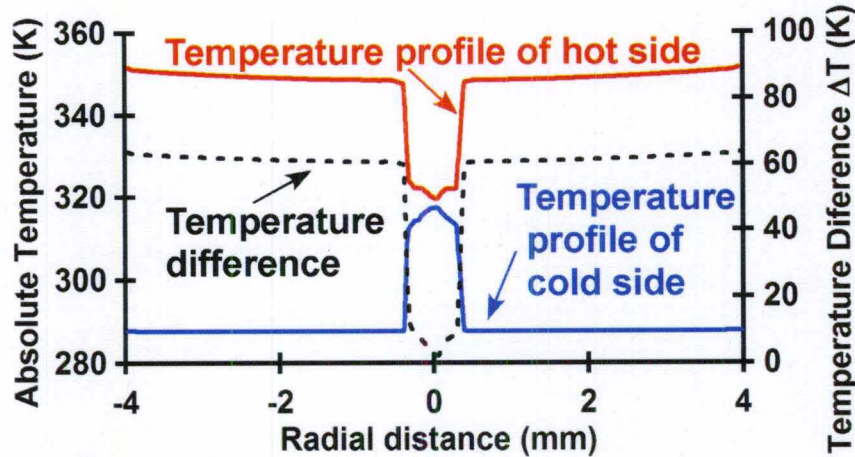


Figure 60. The simulated temperature distribution along the top (line HH' in Figure 59) and bottom (line CC' in Figure 59) surfaces of the nanoporous material for the radial design is plotted as a function of the radial distance from the center of the nanoporous material. The temperature difference is also shown. This plot shows a fairly uniform temperature difference except at the center where a hole is drilled in the aluminum heat spreading plates.

radial pump design is also significantly better. A larger temperature difference will result in a larger temperature ratio, which will result in a larger pressure difference, as shown by equation (3.2). The larger temperature difference and thinner nanoporous material (smaller L) will result in a larger mass flow rate, as shown in equation (3.41). Also, the nanoporous material in the radial pump design does not suffer from sidewall convection and radiation heat loss to the environment since the nanoporous material is guarded on all sides by the thermoelectric device, which may be contrasted with the lateral design in which only one of four sides of the nanoporous material is protected from convection and radiation losses. Thus the radial pump design is expected to perform better than the lateral pump design.

6.3 Results

6.3.1 Pressure mode testing

To measure the pressure difference that may be obtained with the pump, a digital pressure sensor from Mensor, Inc., with a dead volume of 0.8 cc, is connected to the cold side of the pump using tubing, and the hot side of the pump was left open to the ambient air. An identical pressure sensor is used to monitor the room pressure. The difference in the pressure readings provides the pressure difference generated by the pump. *Figure 61* (a & b), shows the pressure difference as a function of time when subjected to the sequence of input powers provided in Tables (5&6) for lateral and radial design pumps respectively. The power to the pump is incremented in steps and the pressure difference is recorded using a custom Labview program. The pressure is permitted to stabilize, meaning that the flow rate becomes zero, before incrementing the power level to a new constant value. The maximum pressure difference obtained is 1.686 kPa using the radial pump design. Tables (5&6) provide the input power values corresponding to each pressure step in *Figure 61a* and *Figure 61b*, respectively. Thermocouples attached to metal plates are used to measure the temperature of the hot and cold sides as a function of thermoelectric power. The thermocouples are located within the aluminum in the radial

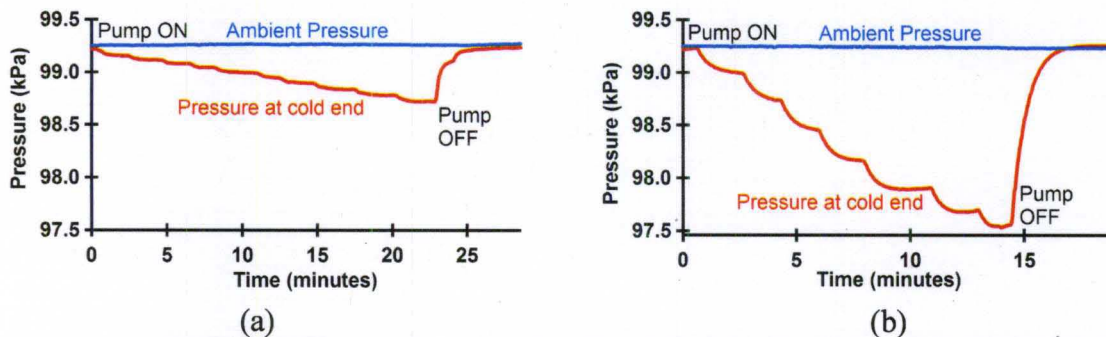


Figure 61. Pressure differential obtained at the cold end with (a) the lateral pump design, and (b) the radial pump design. For each value of input power the pump was allowed to stabilize before the power was increased to the next higher value.

Table 5. For the lateral pump design, this table shows the measured pressure difference obtained as a function of the input power. Each line of the table corresponds to a step in the pressure curve shown in Figure 9(a).

Power (Watts)	Pressure Difference (Pa)
0.18	96.53
0.04	137.9
0.70	172.4
1.1	213.7
1.5	273.0
2.0	315.8
2.5	369.6
3.1	428.2
3.8	482.6
4.5	539.9

Table 6. For the radial pump design, this table shows the measured pressure difference obtained as a function of the input power. Each line of the table corresponds to a step in the pressure curve shown in Figure 9(b).

Power (Watts)	Pressure Difference (Pa)
0.23	250.2
1.9	510.2
1.9	786.7
3.3	1076
4.7	1334
6.6	1544
8.5	1686

design and do not touch the nanoporous material, so the actual temperature difference across the nanoporous material is expected to be smaller. In the lateral design although the thermocouples are in the air gap between the membrane and the plates, still they are not touching the actual membrane sides firmly rather they are glued on the plates, so the actual temperature difference is expected to be smaller than that measured due to air gap resistances. Based on equation (3.2), the temperature ratio of the hot side to the cold side as a function of input power may be obtained, but the actual hot and cold temperatures cannot be calculated. The calculated temperature ratios across the nanoporous material are thus smaller than the temperature ratios obtained from the thermocouples. The hot side of the membrane is expected to be at a lower temperature and the cold side is expected to be at a higher temperature from the observed thermocouple readings. At high

pump power, the cold temperature increases above room temperature even while providing a larger temperature difference.

6.3.2 Flow mode testing

The flow rate is measured by recording the velocity of a water drop inside the inlet pipe for both the forward and reverse modes of operation. When the droplet is in the pipe connected to the cold face of the pump it was pulled towards the pump and with the change in voltage polarity when the same face of the pump turns hot, the droplet is pushed away from the pump. Capillary action does not influence the speed of the droplet, as there are symmetric capillary forces on either side of the droplet. The droplet velocity was measured with a ruler and a stopwatch. The flow rate was normalized with respect to the nanoporous material cross-sectional area so that the two pump designs may be compared. The normalized flow rate as a function of pump power is shown in *Figure 62*. The maximum normalized flow rate for the lateral pump design is $0.03 \text{ cm}^3/\text{min}/\text{cm}^2$, and the maximum normalized flow rate for the radial pump design is $2.3 \text{ cm}^3/\text{min}/\text{cm}^2$, which is a flow rate of $0.74 \text{ cm}^3/\text{min}$. The maximum input power permitted is different for the

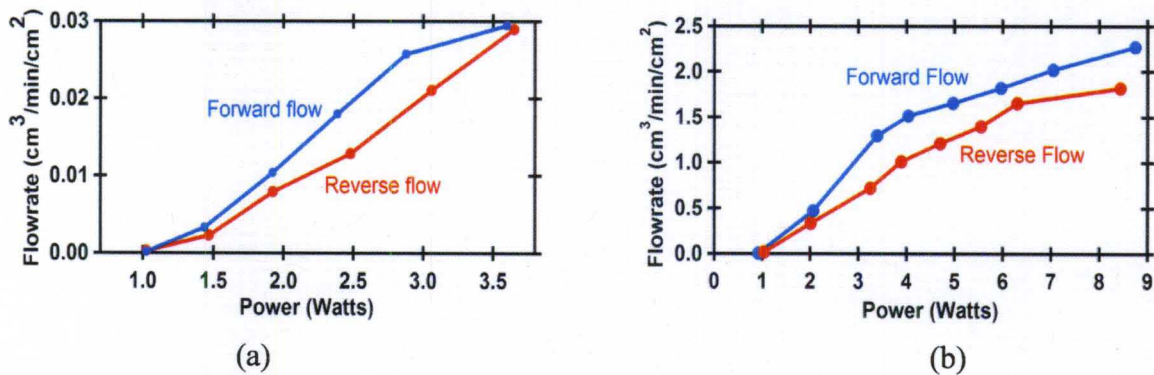


Figure 62. Graph showing the measured flow rate normalized to nanoporous material area as a function of the pump power consumption, for forward and reverse flow directions. (a) Lateral pump design, (b) Radial pump design.

two devices because there are different specifications for the thermoelectric modules. In addition, the criteria for maximum power input to these devices depend upon the thermal load of the thermoelectric device and the melting temperature of the nanoporous material. When both devices are operated at a power of 3.4 Watts, the radial pump design produced a normalized flow rate that is 50 times greater than the lateral pump design. The reverse flow rate for the radial pump design is expected to differ from the forward flow rate because of the asymmetry of the design. The top of the nanoporous material is more closely coupled to the thermoelectric than the bottom of the nanoporous material.

6.5 Pressure-flow characteristics

At constant power pressure differential is measured for a range of flow rate values to generate the pump pressure head versus flowrate curve. By constant power it is implied that the hot and cold side temperatures of the pump are constant which means the temperature difference along the pump channel is maintained the same for all the measurements.

6.5.1 Experimental analysis

The experimental setup uses a syringe pump in conjunction with the Knudsen pump connected by a T joint shown in *Figure 63*. The syringe pump is used to supply various flowrates and the corresponding pressure drop on the cold side of the Knudsen pump is measured using the pressure sensor for one particular pore size and a particular input power to the pump. Both the flows from the syringe pump and Knudsen pump balance each other at equilibrium. At equilibrium the rate at which the syringe pump pumps air into the system, the Knudsen pump pumps the air out of the system at the same

rate. As per the setup the steady state pressure drop is obtained where the syringe pump is flowing gas in to the pump and the Knudsen pump is pumping gas out. These rates become equal and constant at steady state.

The data points for different flowrates with corresponding pressure drops at the cold side is a linear fit and the slope of the straight line is proportional to the power applied to the pump shown in *Figure 64a* for the radial design thermoelectric pump. *Figure 64b* is for the resistive heater pump whose active pump area is 10 times that of the radial thermoelectric pump. Both the pumps have been tested with a 25 nm pore diameter polymer membrane made of mixed cellulose ester. At a power of 4.18 Watts the maximum flowrate obtained by the thermoelectric pump is 204 mL/min. This is the no load case. So, the experimentally determined flowrates with the droplet velocity in section 6.3.2 is in a way under reported from the actual maximum flowrate achievable by the pump because with the droplet the flowrate suffers due to viscous forces in the water droplet and adhesion forces against the wall of the pipe. The datapoint of flowrate and pressure for this particular power of 4.18 Watts with the droplet velocity measurement technique should satisfy the equation of the line in *Figure 64a*. This graph in *Figure 64a* is compared to the *Figure 27* from Chapter 3, which has been derived from the theoretical model.

The theoretical model predicts much higher flowrate of 14 mL/min because the theoretical model of Section 3.4 assumes the following conditions: a) No imperfections in channels and they are all straight channel pores, b) negligible contact resistance between the porous membrane and the metal plates, c) the surfaces of the membrane on both sides are at a uniform temperature.

In actual experiments with the membranes used from Millipore the number of pores is unknown. In the theoretical model the number of pores is estimated based on the porosity of the membrane as per the specifications of the company. This as described above assumes no leakage and straight cylindrical pores which is not the case with practical experiments. There would be leaks and bigger pores due to manufacturing tolerances and also the SEM image of the membrane in *Figure 55* shows a sponge like structure which means the pores are not cylindrical all the way from one side to another. The membrane's pore orientation is like random interconnected paths. Also, the thermocouples measure the temperature on the heat spreaders not on the actual membranes. The temperatures on the heat spreaders are different than those on the actual membrane templates. These, two above reasons form the main criterion for discrepancy in theoretical and experimental results.

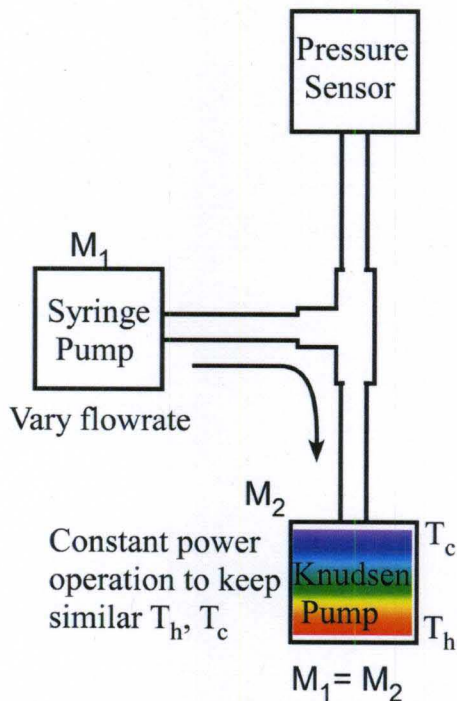


Figure 63. Schematic of the experimental set up used to measure pressure difference as a function of flowrate at a constant power.

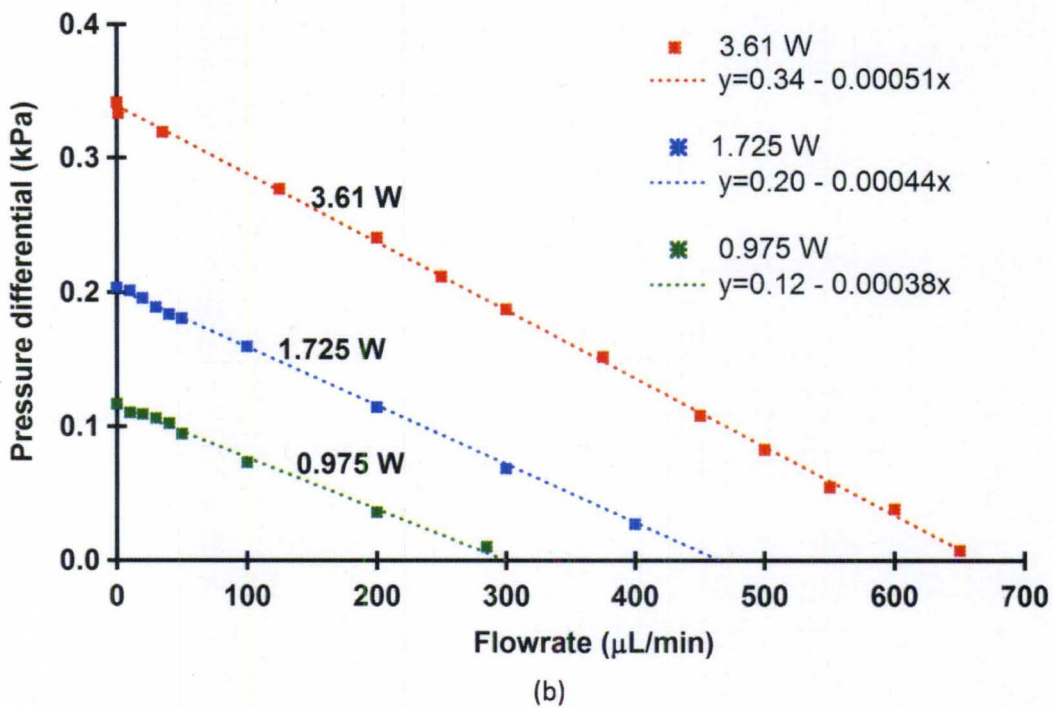
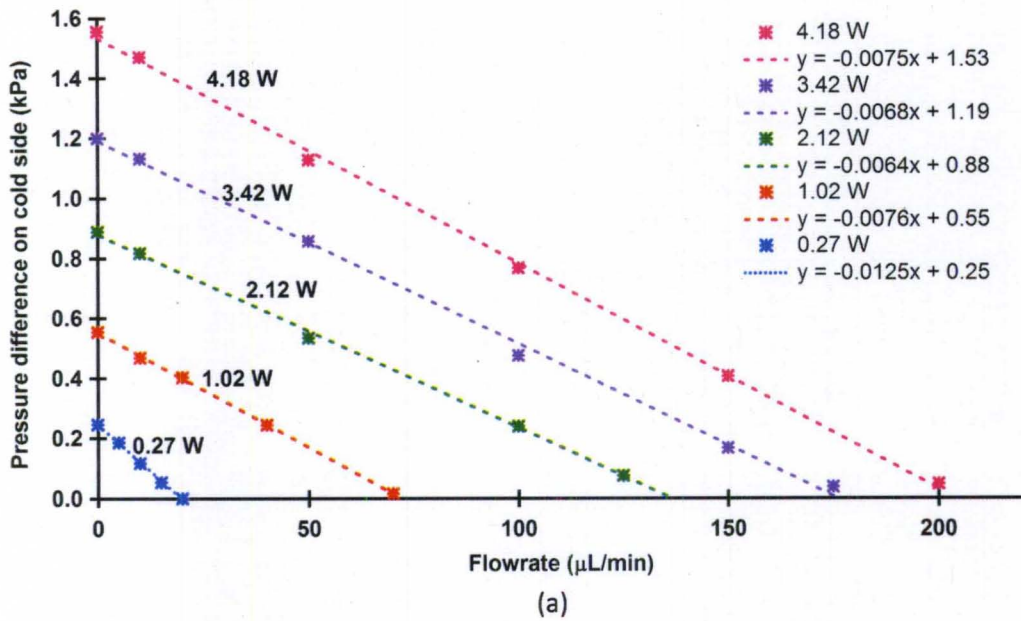


Figure 64. Pressure flow characteristics of (a) thermoelectric Knudsen pump, (b) Knudsen pump made out of a resistive heater. Both the pumps use 25 nm pore size membranes. The active pump area used in the resistive heater pump is 10X the active pump area of the thermoelectric pump.

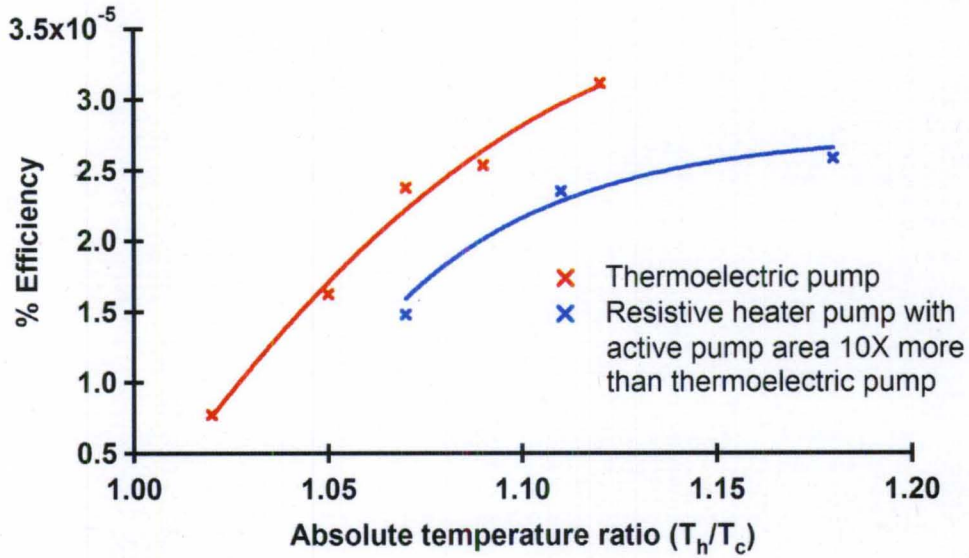


Figure 65. Pump efficiency as a function of hot and cold side temperature ratios. The comparison shows that the thermoelectric pump has a better performance.

6.7 Efficiency of the pump

The theoretical efficiency of the pump is calculated by the experiment in section 6.5.1. The output power delivered by the pump is the area under the pressure – flow graph. The point on the pressure-flow graph corresponding to maximum pressure difference is $\Delta p/2$ and maximum flowrate is $\dot{M}/2$. Thus, the output power delivered by the pump is $\frac{1}{4}\Delta p\dot{M}$. The input electrical power to the pump is the power consumption by the thermoelectric or the resistive heater which is VI .

So, efficiency ' η ' becomes $\frac{\text{output power}}{\text{input power}} = \frac{\Delta p\dot{M}}{4VI}$

$$\eta = \frac{\Delta p * \dot{M}}{4 * V * I} \quad (6.1)$$

The efficiency versus absolute temperature ratio for both the thermoelectric and resistive heater pump are obtained in Figure 65 The pump output is calculated by using the average Δp and average flowrate obtained from the pressure-flowrate experiment in

Figure 64. The slope of the pressure-flowrate curves is higher for the thermoelectric pump compared to the resistive heater pump. The flowrate will depend on the number of pores or rather the cross sectional area of the porous membrane which is 10 times more in the resistive heater pump. At the same temperature ratio although the active pump area is an order of magnitude less for the thermoelectric pump its efficiency is higher compared to the resistive heater pump shown in *Figure 65*, which proves that thermoelectric helps to increase efficiency of these pumps. In the future using a different thermoelectric design the efficiency could be further increased.

The different approaches would include having a smaller thermoelectric and thus increasing the active pump area in the same pump packaging as from the present design of radial thermoelectric pump, the thermoelectric could be made nanoporous to cut down on the heat losses and the pore sizes of the pump material could be engineered to reduce reverse pressure flow.

Another method of categorizing pump efficiency is called thermomolecular pressure difference (TMPD). Thermomolecular pressure difference is defined as the maximum normalized steady-state pressure difference that can be produced to that of the normalized temperature difference applied to a channel permitting thermal transpiration [49].

$$TMPD = \frac{\frac{\Delta p_{max}}{p_{av}}}{\frac{\Delta T_{max}}{T_{av}}} \quad (6.2)$$

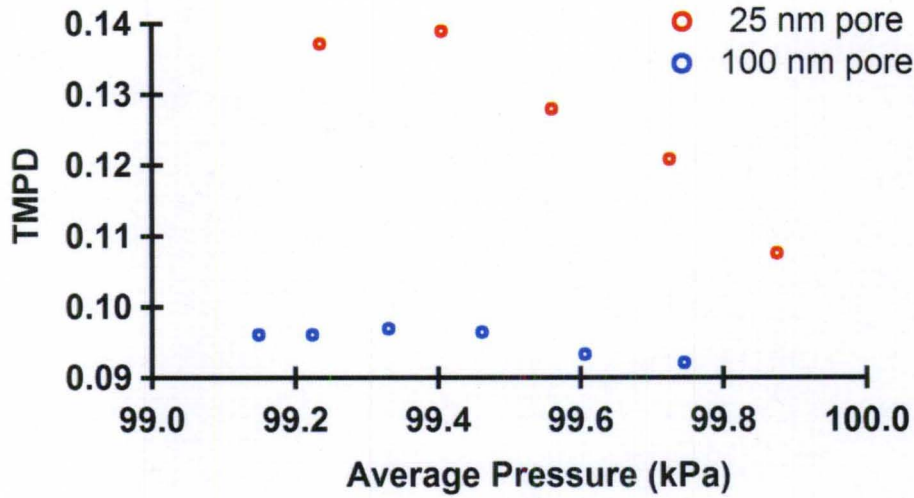


Figure 66. TMPD comparison of the thermoelectric radial design pump for channel size of 25 nm and 100 nm against working pressure.

Here, Δp_{\max} is the maximum pressure difference when the flowrate is zero, p_{av} is the average operating pressure of the pump, ΔT_{\max} is the maximum temperature at which the maximum pressure difference is obtained and T_{av} is the average of the hot and cold side temperatures of the pump's channel.

The gas Knudsen number and the accommodation coefficient of the channel's wall are the primary parameters which determine the TMPD. As the capillary radius becomes on the order of several nanometers the mean temperature of the tube also becomes important. The maximum pressure difference is obtained at zero flowrate and thus if the flowrate equation (3.41) is set to zero, the TMPD becomes proportional to the ratio of the flow coefficients which for a particular Knudsen number could be found from Figure 67.

$$TMPD = \frac{\frac{\Delta p_{\max}}{p_{\text{avg}}}}{\frac{\Delta T_{\max}}{T_{\text{avg}}}} = \frac{Q_T}{Q_P} \quad (6.3)$$

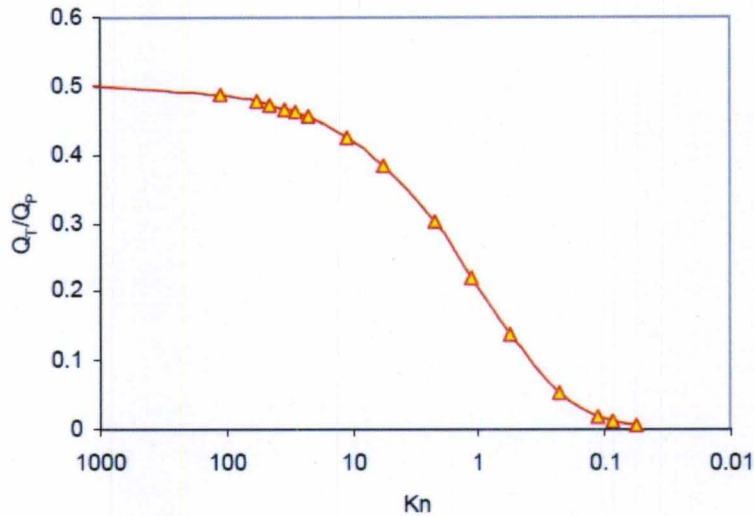


Figure 67. Ratio of flow coefficients plotted against a range of Knudsen numbers. (figure taken from [49])

The TMPD values are 0.126 for the 25 nm and 0.096 for the 100 nm pore diameter membrane respectively. The theoretical TMPD values for 25 nm pore diameter is 0.25 and for 100 nm pore diameter is 0.15 which are higher than the values obtained from the experiments in *Figure 66*.

Along with the reverse pressure flow, incorrect temperature measurements on the surfaces of the membrane are possible likely causes of the discrepancy in the TMPD values. The pump design makes it difficult to measure the temperatures accurately on either side of the porous membrane. Improper thermal contact of the thermocouples also adds to the problem of accurate temperature measurements. The theory of TMPD does not account for the convective loss through the gas flow.

CHAPTER 7 – CURRENT PROGRESS USING NANOPOROUS THERMOELECTRIC AS KNUDSEN PUMP

7.1 Nanoporous Thermoelectric

As discussed in Chapter 3, the optimal way to increase the efficiency of this Knudsen pump is to implement a thermoelectric to control both hot and cold end temperatures of the channel in an active manner. The pump channel also needs a lower conductance which is achieved by multiple channels in the form of pores to improve the flowrate.

7.2 Merits of using nanoporous thermoelectric

The successful pump made out of a thermoelectric does not efficiently couple the

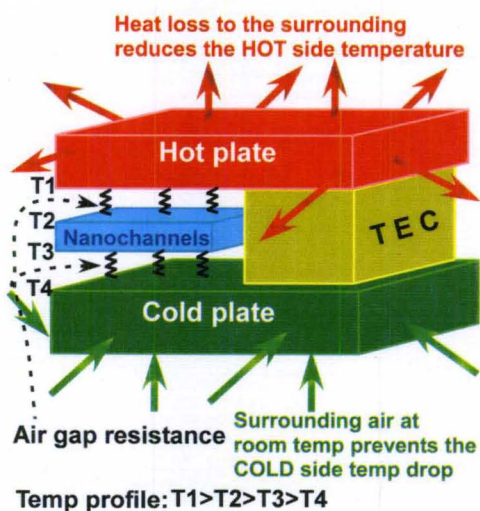


Figure 68. Diagram illustrating thermal losses in the thermoelectric pump.

temperatures of the heat spreader and the ends of the channel material due to the air gaps, which is reducing the efficiency of the pump. There are also thermal losses to the environment from the surfaces of the heat spreaders. *Figure 68* shows the air gap resistances between the pump channels and the heat spreaders which drastically reduce the temperature gradient across the pump channel ends. This is also evident from the simulations in Chapter 6. As shown in *Figure 68*, the temperature on the hot side plate is T_1 , and the temperature on the cold side plate is T_4 , where $T_1 > T_4$. If there were no air gaps the temperature difference across the pump channels would have been $|T_1 - T_4|$. But in actual practice, due to the air gaps the hot side temperature reaching the channel material is T_2 , where $T_2 < T_1$ and the cold side temperature reaching the channel material is T_3 , where $T_3 > T_4$. Thus, $|T_2 - T_3| < |T_1 - T_4|$. So, overall temperature difference along the channels gets reduced. The problem of heat loss to the surroundings from the hot plate and heat gain from the surroundings to the cold plate could be minimized by proper insulation but still cannot be totally eliminated and thus having no heat spreader to

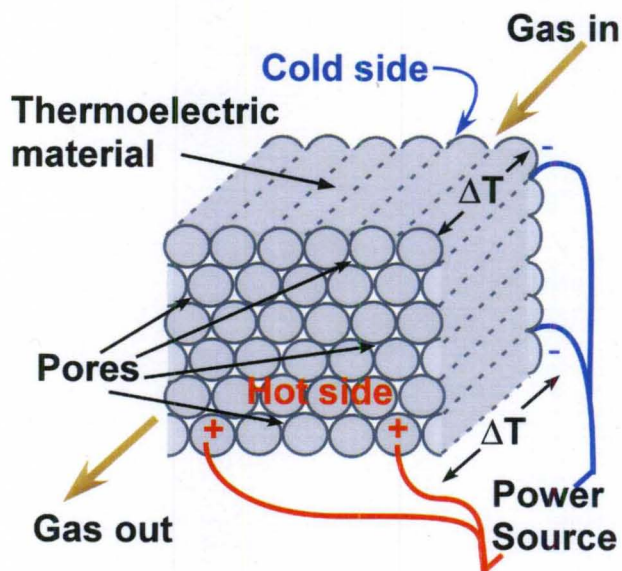


Figure 69. Schematic showing the working of a nanoporous thermoelectric Knudsen pump.

transfer the energy is the best design.

Using a porous thermoelectric has tremendous potential for making a better Knudsen pump to compensate for the drawbacks identified above. If successfully designed and fabricated this nanoporous thermoelectric in itself will be a pump as well as a highly efficient thermoelectric, thus killing two birds with one stone. The nano pores of this thermoelectric will form the channels for thermal transpiration which will give a high flowrate and the nanoporous thermoelectric when used as a thermoelectric cooler will make one side hot and the other side cold thus setting up the temperature difference required for the operation of the pump. In this model there will be no air gaps existing between the pump channel and the thermoelectric since the channels are essentially forming the thermoelectric too and will utilize the maximum energy generated. There are no heat spreaders which will make a compact pump and reduce thermal losses to the atmosphere and the entire thermoelectric energy will be used up to create the temperature gradient between the openings of the nanochannels.

The *Figure 69* shows a schematic of the nanoporous thermoelectric as a pump. The bulk thermoelectric material will be made nanoporous either in the form of straight channel pores or a cluster of ordered zig-zag pores which open at both ends. The faces of the thermoelectric except the front and rear will be sealed for gas leakage. The front and rear faces of the thermoelectric will have electrical contacts for current flow. When excited by a voltage source the charge carriers will propagate and carry the heat with them which will make one face hot and the other face cold. Since these faces are opened to the atmosphere the gas will start flowing from the cold face to the hot face due to thermal transpiration. For measurement purposes the cold face will be connected to a gas

inlet which will be either used for pressure measurement or flow measurement similar to earlier pumps.

7.3 Nanoporous thermoelectric materials

Nanoporous Bismuth has been shown to have a thermal conductivity as much as 10x lower than bulk Bismuth [95, 96], and theoretical work has shown that the ZT could be greater than 4 [97, 98]. Although there are many promising thermoelectric materials to consider, the low melting temperature of Bismuth makes it an easy material to work with. Nanoporous silicon has been shown to have a 100 times improvement in the ZT compared to bulk [99, 100], making it an attractive candidate for this research. Other important promising thermoelectric materials which could be made nanoporous for the pump are tellurium and bismuth telluride. The drawback of using these materials is their higher melting point compared to bismuth which makes fabrication difficult. Tellurium has a higher thermo power than bismuth but a lower electrical conductivity on the other hand. Bismuth telluride which is an alloy of both bismuth and tellurium is supposed to give the maximum ZT at room temperature since it has a higher electrical conductivity and low thermal conductivity compared to both bismuth and tellurium.

7.4 Methods to make nanoporous thermoelectric

7.4.1 Porous Si as a Pump

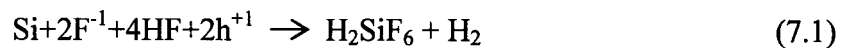
Making the well-known thermoelectric materials like Bi, Te, Se into synthetic nanostructured materials for improved ZT is highly attractive but on the other hand it's expensive too. Si is the widely used material in the semiconductor industry and has low process cost and high yield capabilities. Si in its bulk form is a bad thermoelectric due to

a high thermal conductivity but recent advances have shown a tremendous increase in its thermoelectric property in the form of silicon nanowires [56]. For the Knudsen pump it is difficult to integrate the nanowires into a pump but its complement nanoporous silicon can make a highly efficient Knudsen pump. A theoretical paper on porous silicon mentions that porous silicon can be a very effective thermoelectric material for future [61]. Porous silicon initially became popular due to its photoluminescence properties [101] but it also showed an extremely low thermal conductivity [102, 103] and has been used as thermal isolation in MEMS sensors. Thus, porous silicon holds a good promise for a good thermoelectric material due to its low thermal conductivity. The thermal conductivity of porous silicon has been reported to be 0.6 W/mK, a reduction in three orders of magnitude compared to bulk silicon [104].

7.4.1.1 Formation of porous silicon

Porous silicon can be formed by anodic etching of silicon substrate, dry etching of patterned bulk silicon, stain etching and other newer methods depending on the applications[105, 106]. Anodic etching is one of the most common techniques and is followed in our experiments. Anodization of mono crystalline silicon wafer in presence of aqueous HF results in the formation of porous silicon. Evolution of hydrogen takes place during the formation of porous silicon.

The following chemical reaction illustrates the mechanism [107]:



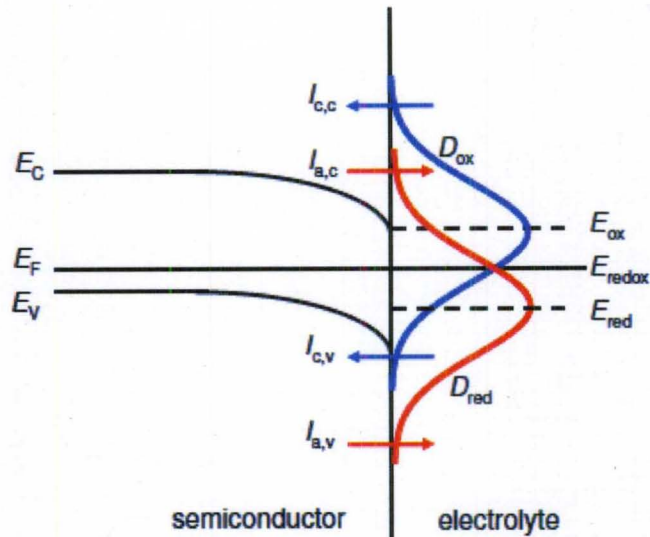


Figure 70. Band diagram at the interface of the silicon and the electrolyte showing different energy levels that lead to the concept of formation of porous silicon. (figure from PhD. dissertation "Porous Silicon for Thin Solar Cell Fabrication", by Osama Tobail)

To clearly understand the porous silicon formation based on the reaction at the interface of the semiconductor and the electrolyte a simplified band diagram is depicted in Figure 70. Analogous to the Fermi level E_f in semiconductors, the energy level of electrons in the electrolytes are characterized by the redox potential E_{redox} . The redox potential determines the tendency of the species in the electrolytes to give up or accept electrons. The redox potential is the mathematical mean of the energy of the oxidized species E_{ox} and that of the reduced species E_{red} . The density of empty states has a Gaussian distribution around the energy level of the oxidized species E_{ox} and the density of occupied states has a Gaussian distribution around the energy level of the reduced species E_{red} . When a semiconductor and an electrolyte comes in contact there is a thermodynamic equilibrium $E_f = E_{redox}$ at the interface due to charge transfer. In case of n type silicon electrons flow from silicon to the electrolyte and for p type the electrons move from the electrolyte to the silicon. The anodic current involves an electron transfer

from the electrolyte to the semiconductor. Electron transfer from the electrolyte to the valence band of the semiconductor depends on the availability of holes at the semiconductor surface.

Different models have been proposed on the mechanism of porous silicon formation [108, 109]. The research by Lehman and Goesele in the early 1990s postulated quantum confinement theory in porous Si to be responsible for the formation of micropores in heavily doped p type Si. The quantum confinement occurs from the increased band gap caused by quantum porous structure. The quantum confinement prevents the charge carriers from entering the walls of the pores and thus only the pore tips dissolve leading to the pore depth.

Table 7. Porous silicon can be classified based on the pore diameter[IUPAC classification of pore size][110]:

Type of porous Si	Pore size d_p [nm]
Microporous silicon	$d_p \leq 2$
Mesoporous silicon	$2 < d_p \leq 50$
Macroporous silicon	$d_p > 50$

7.4.1.2 Pore Morphology

Porous silicon exhibits various pore morphologies depending on doping type, concentration of doping, current density of the electrochemical etching process, electrolyte concentration and illumination [110].

The morphology of pores formed on n type silicon depends on illumination – frequency, intensity and direction (front and back). Back side illumination produces straight pores while front side produces random interconnected pores [111]. In n type

silicon holes are minority carrier. Electrochemical dissolution requires holes. Light assisted etching is helpful in n type silicon since it helps generate electron-hole pairs. For a n-type silicon the diameter of pore decreases with doping concentration of the sample and for a p-type silicon the diameter of pore increases with increase in sample doping. The pore diameter increases with an increase in current density and an increase in potential. The pore diameter decreases with increase in HF concentration.

7.4.1.3 Porous Silicon membrane fabrication

The following process outlines the experiment performed to obtain porous silicon membranes. P type etching is preferred since it does not need any illumination and it's easier to maintain a dark atmosphere during etching. The p type wafers have resistivity of 0.1 ohm-cm. Aluminum is being used as the metal contact layer. The current density is reduced towards the end of the etching so as to get more uniform pores and prevent forming of pores with large diameters which will lead to cracking. The porous silicon formation has been carried conducted in a Teflon container with a gold mesh as the cathode and the silicon as the anode shown in *Figure 71*. The etching time for moderately doped p type silicon based in 1:1 HF:C₂H₅OH concentration has been estimated to be around 30 min for a 50 micrometer depth based on the following formula [112]:

$$r = 10^{[0.89 \cdot \log J - 1.2]} \quad (7.2)$$

where r is the rate of porous silicon etching(micrometer/min) and J is the current density(mA/cm²).

The fabrication of the complete porous silicon chip has been outlined in *Figure 72*. A setup shown in *Figure 71* is used for the anodic etching of silicon. Teflon is used as the material to make the etching cell. The oxidized silicon wafer is patterned and then etched in TMAH to thin it down to 50 μm . Aluminum is sputtered on the backside of the wafer and then annealed to make proper ohmic contacts during etching. A gold coated metallic mesh is used as the cathode and the silicon sample to be etched is used as the anode. The dicing lines on the wafer are also thinned down in the TMAH etching process and thus the samples could be easily detached from the whole wafer. Aluminum foil is used as the backside contact which is pressed with a rubber O-ring against the back side of the sample for proper contact with the sputtered aluminum. The O-ring also prevents leaking of the electrolyte. After the etching of pores and stripping off the metal contact layer, the pores have to be opened for them to be through from one side of the wafer to another. This is done by the DRIE, a recipe which has mostly SF_6 gas to etch silicon, a

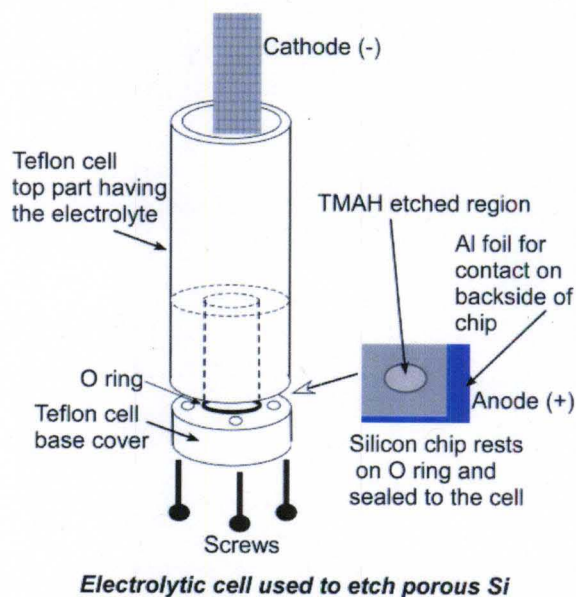
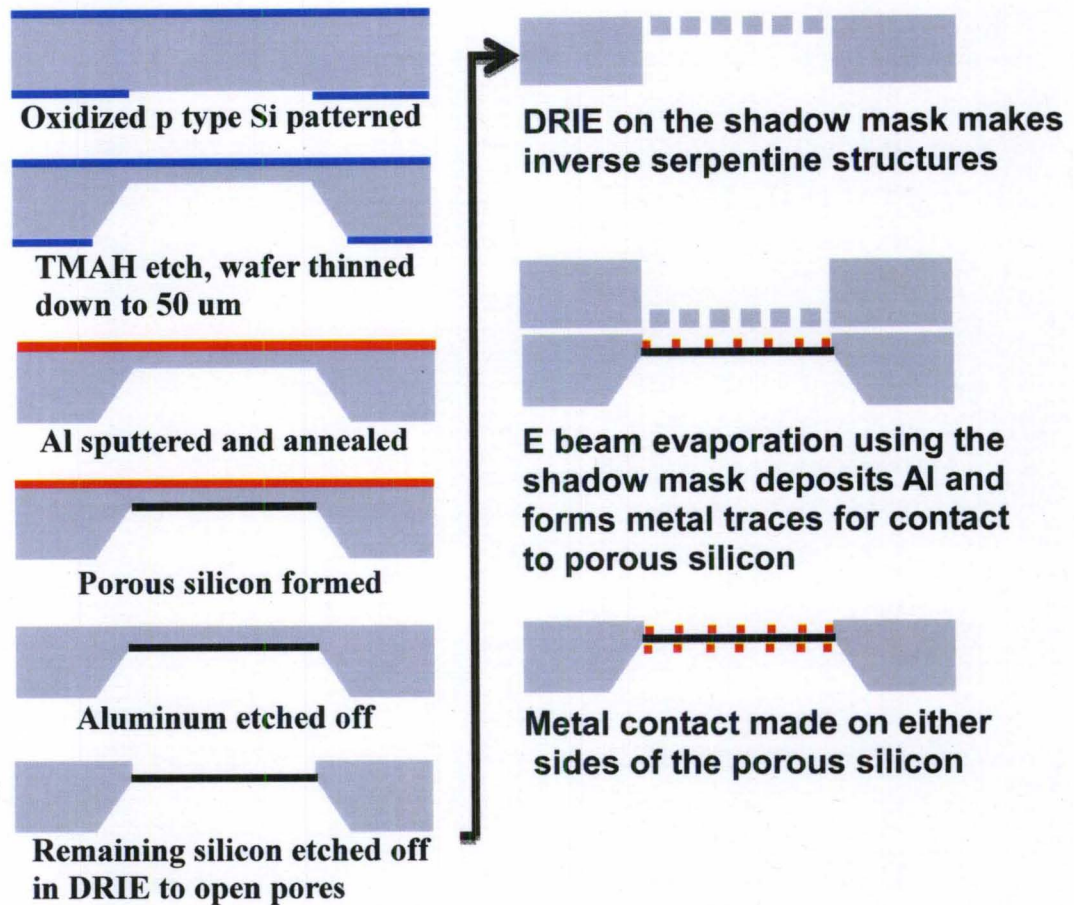


Figure 71. Schematic of the set up with electrical connections and the silicon chip which is made porous by anodic etching.

little oxygen and no passivation. The reason for this step is that in porous etching the sides of the sample or the periphery of the silicon bordered by the O-ring etches more than that of the center at any given time. Once, the sides etch completely or when the electrolyte seeps in through those side pores to the other side there is no more etching as the current conducts through the electrolyte to make the circuit rather than through the wafer as it has a least resistive path.

Now, after the formation of porous silicon for thermoelectric effect proper contact has to be made. Electron beam evaporation is used along with shadow masking to deposit thin film of aluminum in the form of a serpentine structure so as to cover the porous silicon uniformly on both sides and also leaving half of the pores opened for gas flow as shown in *Figure 75b*. Shadow masking was preferred because of the fragile structure of the porous silicon since any further wet etching may damage the porous membrane. Electron beam evaporation has a larger line of sight than sputtering and thus was preferred since with the shadow mask there will be significant distance to cover before the deposition actually falls on the target porous membrane. The same shadow mask was used twice: once on each side after breaking the vacuum in the electron beam evaporator. The metal used was aluminum and the thickness was around 0.5 micron.



■ Silicon ■ Oxide ■ Aluminum ■ Porous Si

Figure 72. Process flow for making porous silicon membranes. Contacts are made thereafter using shadow mask evaporation.

7.4.1.4 Results

The scanning microscope images of the porous silicon etched membranes obtained shows pores on both sides of the membrane which indicated that channels have been formed in the silicon chip. Figure 73a shows pores on the front face of silicon where the etching began and Figure 73b shows the pores on the back face of the silicon which propagated through the anodic etching from the front face. For the same current

density of 40 mA/cm^2 , the pores on the back side are larger in diameter which measure around 80 nm as compared to those on the front face which measure around 20 nm . The reason is attributed to the reduction in concentration of the etchants over the etching period. *Figure 74a* shows the cross sectional view of silicon sample which has been etched in a double cell from both sides. The method of etching from both sides was tried to reduce pore size variation from top to bottom face since double side etching takes less time compared to single cell etching. In double cell etching there are two electrodes in each chamber of the cell. The current completes the circuit through the silicon and in the process the anodic etching takes place. This method eliminates the metal deposition step on the sample since wired electrical connection is not made to the silicon during etching. *Figure 74b* shows the cross sectional view of the silicon sample etched from one side in a single cell etching bath. The image is taken on a sample which is not completely porous since a fully etched porous sample is difficult to profile in the SEM.

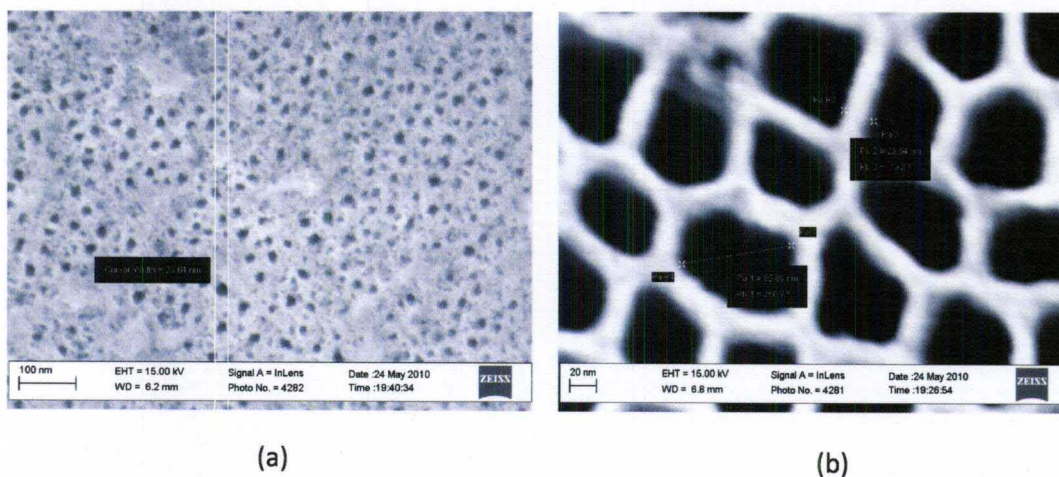


Figure 73. (a) SEM image showing pore distribution and diameter on the front side where of the nanoporous silicon (b) pore distribution and diameter on the back side. Etching was done at 40 mA/cm^2 in 1:1:: HF:C₂H₅OH

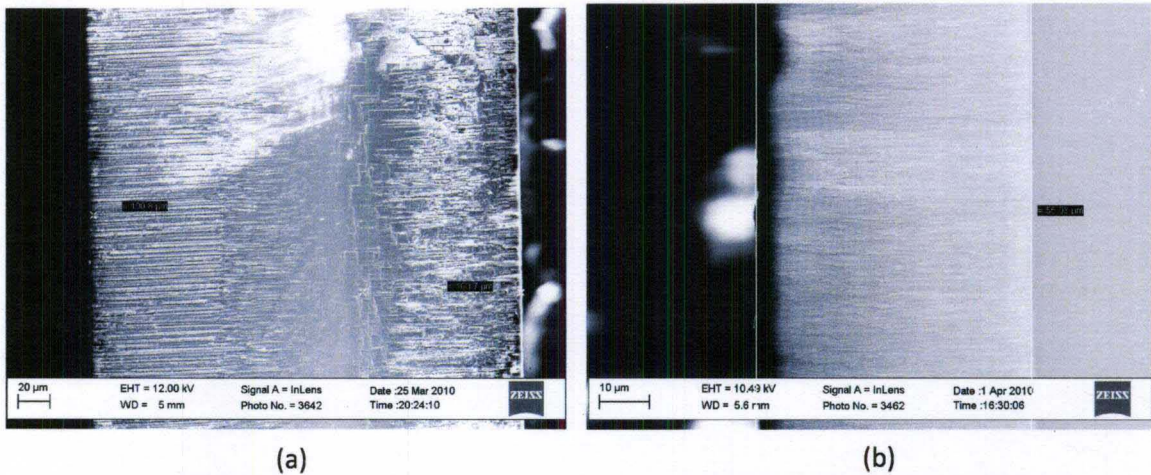


Figure 74. (a) Cross section of silicon wafer etched in double cell etching bath at 60 mA/cm^2 in 1:1:1::HF:H₂O:C₂H₅OH for 30 minutes each side, (b) cross section of wafer etched in single cell etch bath using conditions of Figure 73.

The porous silicon experiment as a whole was partly successful in just making the porous silicon membranes. The porous silicon templates were integrated as Knudsen pumps and supplied with current (see Figure 75a). No pumping was observed in either direction. Possible reasons could be that by making the silicon porous the electrical conductivity was

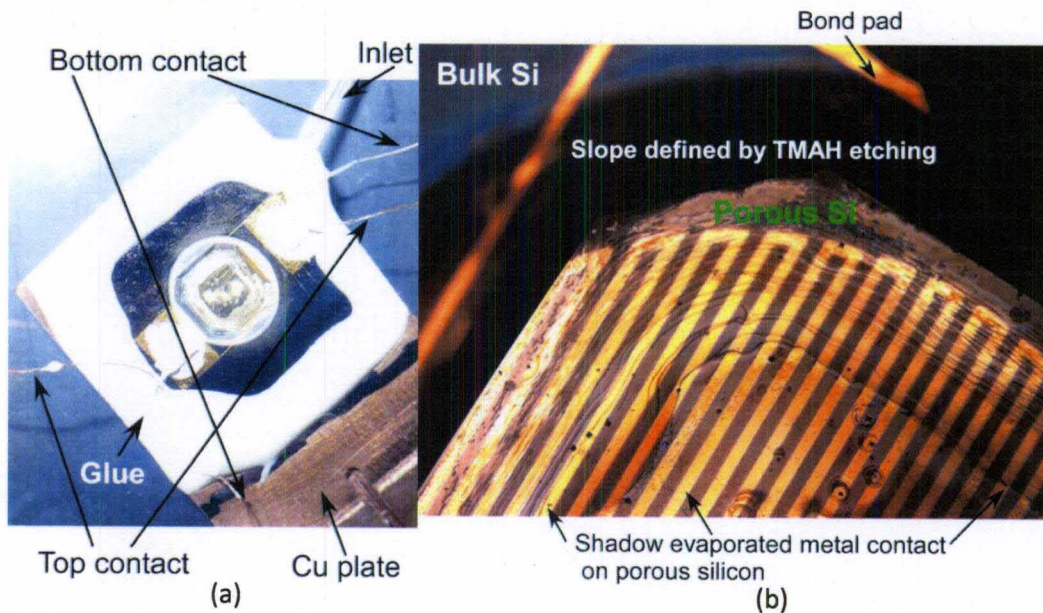


Figure 75. Fabricated pump out of porous silicon with electrical connections shown in (a), optical microscope image of one side of the membrane showing metal contact made by ebeam evaporation shown in (b).

degraded since during the test the contact resistance across bond pads from the top to bottom side measured very high resistances. Also, the porous membrane was surrounded by bulk silicon which may have nullified the thermoelectric effect.

7.4.2 Hot pressing to make nanoporous Bismuth

In this the material of interest is melted by heating them to a temperature over their melting point and then by using external pressure the molten material is forced into a nanoporous host material [113, 114]. The hot press schematic is shown in *Figure 76a* and the equipment is shown in *Figure 76b*. The external pressure is required since most thermoelectric materials have a higher surface energy compared to the host materials.

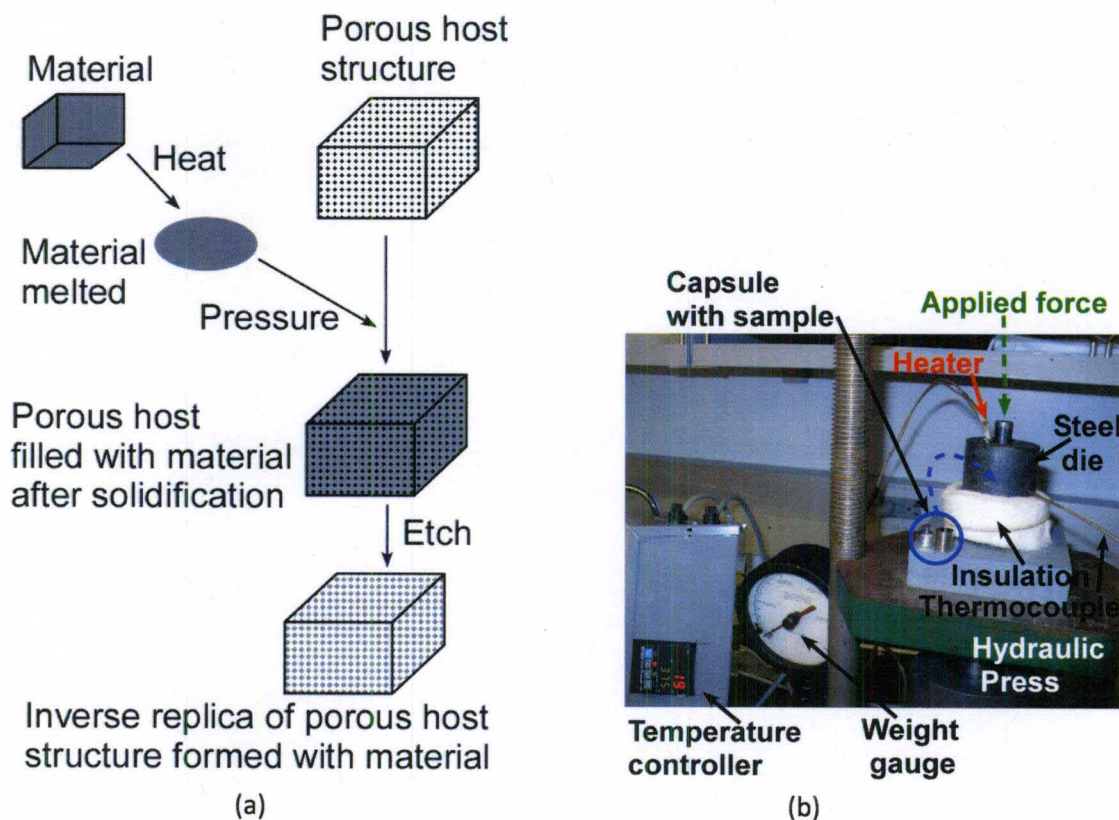


Figure 76. (a) Schematic of the hot press method. (b) The hot press equipment setup along with temperature controller.

The molten thermoelectric material will occupy all the voids of the host nanoporous material and then it will be cooled below its solidification temperature to solidify in those voids. Etching or removal of the host material without destroying the thermoelectric material will make an inverse replica of the host material with a thermoelectric material. The host material should have interconnected voids so that the electrical continuity is maintained in the synthesized nanoporous material. The removal of the host material will lower the thermal conductivity and also form the channels automatically required for thermal transpiration gas flow.

The samples are formed by melt injection of bismuth into silica colloidal crystals. The colloidal crystals are obtained from Dr. G. Sumanasekera in the Department of Physics at the University of Louisville. They are grown using slow sedimentation of monodispersed aqueous silica colloids in a glass cylinder, followed by sintering at 700–750 °C for several hours [92]. The resulting crystal (*Figure 77b*) consists of closely packed, interconnected silicon dioxide spheres arranged in a fcc lattice (*Figure 77a*) with

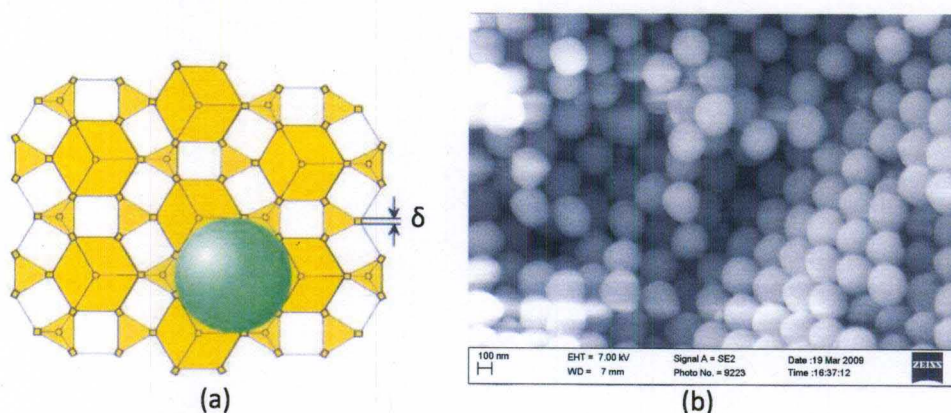


Figure 77. (a) Schematic of arrangement of the spheres of silicon dioxide in the silica crystal, showing octagonal and tetrahedral voids and the interconnect between the voids as δ [92], (b) SEM image of the colloidal silica crystal showing the actual arrangement of spheres.

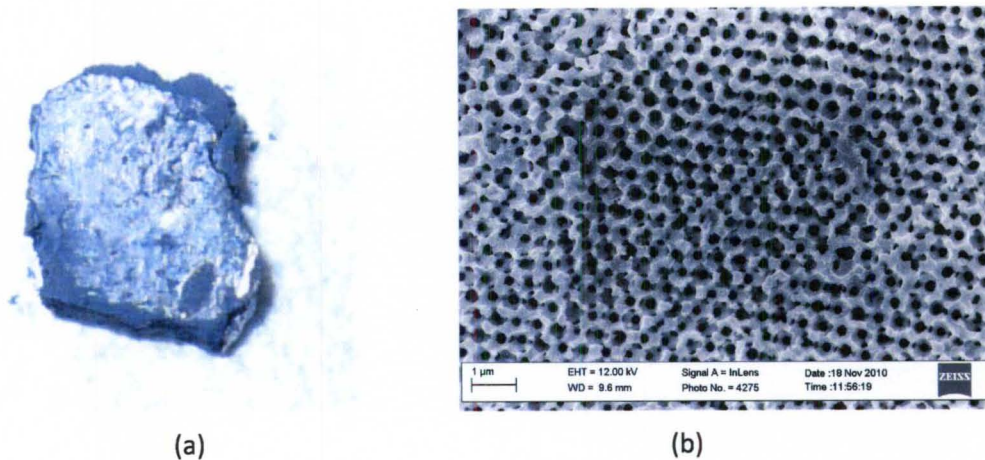


Figure 78. (a) Photograph of nanoporous bismuth obtained from hot pressing after the silica has been etched, (b) SEM image of the nanoporous bismuth showing the voids

interconnected octahedral and tetrahedral voids between the spheres.

The silica colloids used in this investigation have average sphere diameters of 300 nm and octahedral and tetrahedral voids of approximately 120 and 60 nm in diameter, respectively. The voids are interconnected by narrow regions δ that are 10–20 nm in diameter. The voids are filled with bismuth using the melt injection method. A silica colloidal crystal approximately $(5 \times 5 \times 4) \text{ mm}^3$ in size is combined with 99.999% pure 100 mesh bismuth powder in a stainless steel capsule. The infiltration is done by applying a load of 13 – 15 klbs (8–10 kbars) on the capsule at a temperature of approximately 400 °C for several hours. The bismuth infiltrated colloidal sample is then removed from the capsule by grinding off the stainless steel capsule. Next, the bismuth/ silica mixture is mechanically polished to remove the excess uninfiltreated bismuth. Finally, a bismuth inverse replica of the colloidal crystal is obtained by etching out the silica spheres using a pure HF acid solution shown in *Figure 78a*. *Figure 77b* shows the silica colloidal crystals before filling with bismuth and *Figure 78b* after bismuth infiltration without silica.

7.4.3 MOCVD to make nanoporous Tellurium

MOCVD – Metal Organic Chemical Vapor Deposition is a vapor phase process mainly used for producing epitaxial film semiconductors. MOCVD processes were developed by reacting group III organic compounds with group V hydrides under appropriate temperature and pressure to produce molecules of the required material which deposit on the substrate. The organometallic compounds containing the thermodynamic elements are placed in the reactor along with the nanoporous host material which is the substrate in this case (*Figure 79*). After the CVD of the thermoelectric elements on the host structure, the latter is etched away or removed and a nanoporous thermoelectric structure is obtained.

The key difference in both these methods is that while hot pressing is a volumetric template MOCVD is a surface template. Samples obtained by hot pressing are more

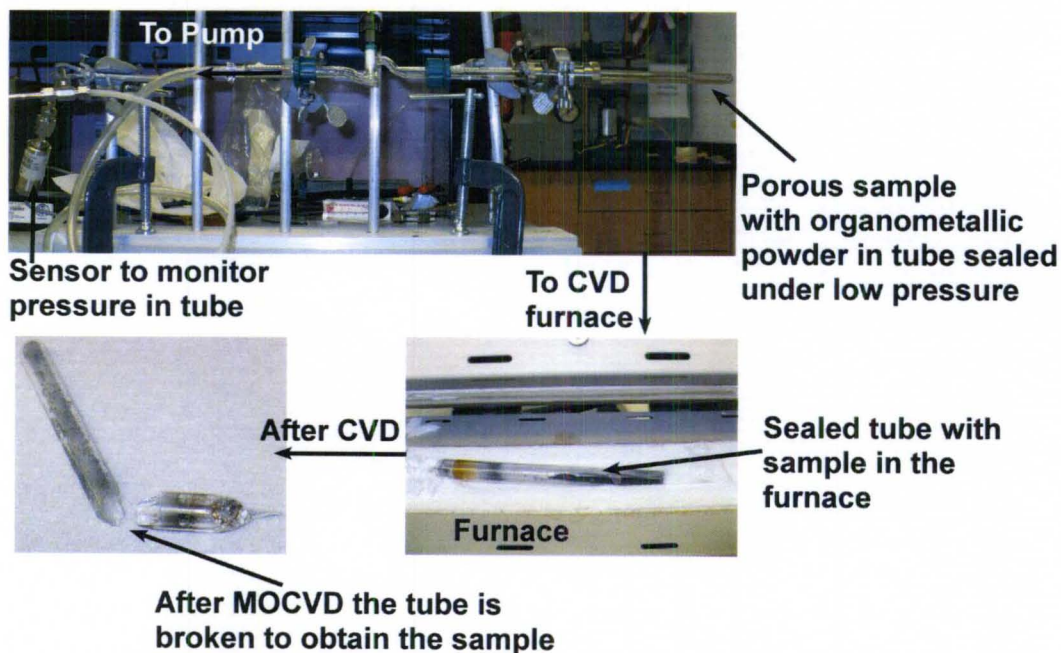
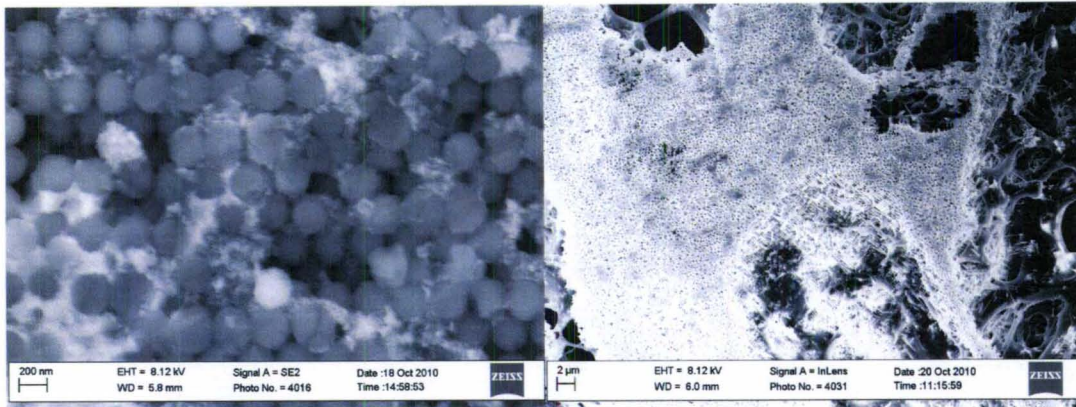


Figure 79. Experimental set up used for MOCVD. The tube reactor being shown in detailed view after the deposition. The actual MOCVD process takes place in the tube inside the furnace.



(a)

(b)

Figure 80. SEM image of a MOCVD tellurium sample (a) with silica, (b) after removing the silica. After the silica has been etched, the porosity is found to be non-uniform, showing a non-uniform deposition.

robust due to the volumetric template compared to those obtained by MOCVD. The advantage of the MOCVD process over hot pressing is that samples will have more porosity.

The sequence of steps leading to the formation of nanoporous thermoelectric follows. First, the opal was impregnated with TeBr_2 in ethanol solution. The sample was dried and the impregnated TeBr_2 was chemically reduced at 400°C in flowing Ar/H_2 to produce an elemental Te layer. After this pretreatment, the next step was to deposit by MOCVD significantly larger amounts of Te from the vapor phase. This was accomplished as follows. The pretreated opal was sealed in a pyrex glass tube together with diphenyl ditelluride and evacuated to a low pressure. The tube was then sealed by a hot flame using an oxy-acetylene torch. The sealed tube was then placed in a tube furnace and heated to 375°C for several hours. At these temperatures, the organometallic compound thermally decomposes to Te and is deposited on the hot opal surfaces, coating the same with tellurium but not completely filling the voids [115]. Then the furnace is

cooled down and the sample is obtained by breaking the tube carefully. The sample is then polished to remove any debris blocking the pores on the surface and finally the silica crystal is etched away in HF.

The tellurium coated silica sample is shown in *Figure 80a* and after etching away the silica the sample is shown in *Figure 80b*. It is seen that the non-uniform deposition has left big open voids in the sample which is not suitable to operate a Knudsen pump.

7.5 Results from Hot press and MOCVD methods

Following table summarizes the results obtained from the hot pressing and MOCVD methods:

Table 8. Nanoporous thermoelectric experimental results.

Process	Thermoelectric material	Thermopower ($\mu\text{V/K}$)	Temperature difference ($^{\circ}\text{C}$)
Hot pressing	Bismuth	-69.1	0.4
MOCVD	Tellurium	357	Not measured
MOCVD	Tellurium coated silica	343	Joule heating

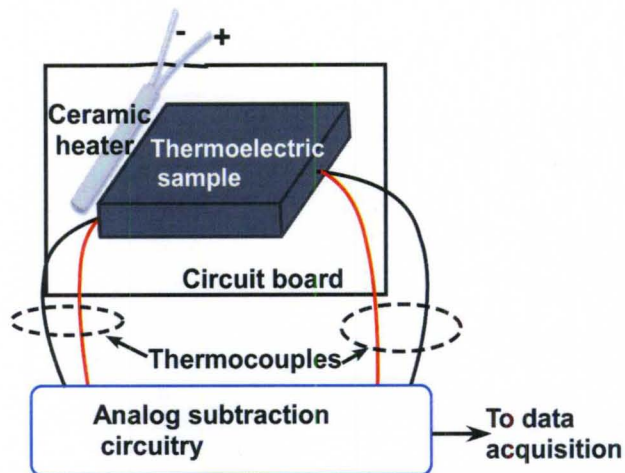


Figure 81. Illustration showing thermopower measurement set up.

For thermopower measurements, the sample is thermally anchored to an integrated circuit IC chip package consisting of two copper plates separated by an air gap. A ceramic heater is mounted on one of the copper plates whose temperature was maintained at 302K. The gap between the copper plates ensures that the heat pulse travels through the sample and not the chip package. Wires are attached to the sample using silver paste: two gold-chromel wires on opposite edges of the sample act as thermocouples/current contacts. This thermopower measurement consists of heating the sample using a voltage pulse (of varying amplitude of 0 - 10 V) and measuring the temperature gradient across the two thermocouples, as shown in *Figure 81*. The thermopower is then calculated using a simple analog subtraction circuit containing three instrumentation amplifiers [116].

The samples are tested to see how efficient they are as a peltier cooler first before testing for the actual pump. Electrical contacts are made using silver paint to the tellurium sample obtained by MOCVD, which produced a lot of joule heating. The heating of the sample did not reverse side with change in polarity of supply voltage and also cold side temperature never went below room temperature. When electrical contacts

are made using a solder to the bismuth sample a temperature difference is obtained between the two opposite faces which has the contacts. Thus, solder makes a good electrical contact to Bismuth. Tin and Bismuth forms a eutectic at 140°C so it is easy to solder on bismuth. Just with contacts and no heat sink a temperature difference of 0.4°C is obtained on the hot pressed bismuth sample when a current of 0.078 A is passed through it. The hot side is 0.2°C above room temperature and the cold side is 0.2°C below the room temperature. The resistance measured across the terminals of the sample is 0.61 ohms. The terminals are separated by 6 mm. The cross-sectional area of the terminal faces is 0.000018 m². The room temperature is 297°K. With the voltage polarities reversed, the same temperature difference is obtained with the hot and cold sides reversed, thus successfully demonstrating a thermoelectric effect. When one side is affixed to a copper plate as a heat sink, the cold side temperature does not go below room temperature since the room temperature is quickly conducted by the copper plate which has a high thermal conductivity.

The MOCVD samples without the silica are very fragile to be tested as a peltier cooler as the sample would break while soldering electrical connections. The MOCVD of tellurium samples with the silica are difficult to solder since the silica surface formed the major surface area where solder would not stick. So, for both of these tellurium samples only thermopower was measured. The thermopower for only porous tellurium is 357 μV/K and for porous tellurium coated on silica is 343 μV/K. The difference in thermopower values for the tellurium samples was because of the heat conduction through the silica negating the thermoelectric effect.

7.5 Sintering of doped Bismuth Telluride

With the above methods of nanoporous thermoelectric not falling in place due to various reasons, like high temperature of melting point of bismuth makes it impossible to melt inject the same into porous voids, nonuniform deposition and thus a fragile structure of thermoelectric in MOCVD process and high contact resistance of porous silicon, sintering appears to be an attractive alternative.

Sintering does not need a temperature over the melting point of the substance and neither does it need the pressure high enough to overcome the high surface tension forces present at the nanoscale. Sintering is the term used to describe the process of combining grains of a substance by bonding them using heat and pressure. Mobility increases with temperature. Higher temperature causes the atoms to move faster in response to the applied sintering stress. It also allows transport by viscous and plastic flow. Sintering is faster at higher temperature due to more active atoms and available sites. If N is the number of available sites and N_0 is the total number of atoms, they are related by the Arrhenius equation:

$$\frac{N}{N_0} = e^{-\frac{Q}{RT}} \quad (7.3)$$

where Q is the activation energy, R is the gas constant and T is the absolute temperature.


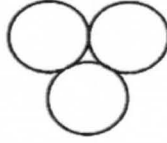
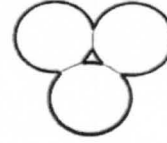
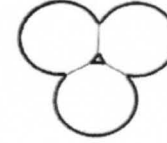
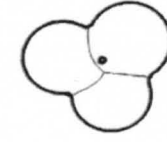
If the nanoparticulate grains of the thermoelectric material could be fused by applying the right temperature and pressure in such a way so as to fuse them with each other and simultaneously make sure that they do not coalesce completely then a nanoporous network could be obtained. This could serve as the nano channels for thermal transpiration and with these nanopores made in the thermoelectric material could provide us with the Knudsen pump which will be driven by thermoelectric power. Pores are

present in the powder compact as inter-particle voids. During sintering the pores can be formed by uneven phase distribution, unbalanced diffusion events, reactions with the atmosphere and capillary spreading of a molten liquid.

The advantages of sintering are:

- ✓ A wide range of thermoelectric materials with high melting point that are difficult to make nanoporous by conventional methods could be easily manufactured by this process.
- ✓ It requires minimum number of process steps and is thus cost effective.
- ✓ It is robust. Cracks and leaks will be minimized in the porous thermoelectric which is an important feature in successful operation of the Knudsen pump.
- ✓ The pore size could be easily controlled by adjusting the pressure of compaction and temperature and the grain size. Pore size increases at lower sintering temperature but the overall porosity decreases.
- ✓ Different geometries could be designed for the pump since the process is no longer dependent on a host material like hot pressing and MOCVD method, and thickness limited the porous silicon method.

The major drawback of this method is the repeatability and controllability of the porosity of the sample. Also, the number of pores per unit volume will be smaller than the above methods since the channels may not be opened all the way through from one end to the other due to grains collapsing during sintering process.

<u>Stages</u>		<u>Description</u>
0. Adhesion		Particles in contact
d: 0.5 p_0 : 0.5 p_c : 0		Particles adhere and form necks
1. First Stage		Necks grow and P_0 decreases
d: 0.6 p_0 : 0.4 p_c : 0		Necks become large pores change to spheroids Open pores disappear Closed pores appear
2. Intermediate Stage		Grain boundary migration occurs leaving spherical closed pores isolated from grain boundary diffusion routes
3. Final Stage		
d: 1 p_0 : 0 p_c : 0		

d: fraction of density to theoretical density
 p_0 : Open porosity
 p_c : Closed porosity

Figure 82. Schematic showing densification of stages in sintering process. The densification intermediate stages determine the porous nature of the sample. (figure adapted from [117])

To make highly porous material densification has to be avoided [117]. Surface diffusion and evaporation-condensation helps in neck growth without densification. Pores with well grown necks have higher fluid permeability and more spherical pore shape. The densification in the sintering process is illustrated in *Figure 82*.

CHAPTER 8 - CONCLUSION AND FUTURE WORK

8.1 Conclusion

The research summarizes methods to increase the pump efficiency by using novel designs and materials. It also highlights the potential for future applications of the pump in the field of bio engineering and energy scavenging by using the improved pump.

For a lateral Knudsen pump two approaches are discussed with regards to choosing the pump material for a higher performance. Silicon was used as the first starting material which has a high thermal conductivity. FEA simulations and experiments in Chapter 3 proved that silicon is not the right material for making a Knudsen pump. It is difficult to obtain significant temperature gradient for successful operation of the pump within a short channel length. If the channel length is made longer to attain higher temperature gradient then the flowrate is sacrificed. Glass with an order of magnitude lower thermal conductivity and with fabrication ease similar to silicon was also tried. The results are better than that of silicon and with glass widely used in microfluidic devices this pump could potentially be integrated with Lab On A Chip for microfluidic applications. But microfabricated straight single channel pumps in silicon and glass have low flow rates which are not always adequate for potential applications.

To improve the flowrate by making the channel conductance higher nanoporous materials are investigated. With similar thermal conductivity as that of glass silica colloidal crystal samples have been made into Knudsen pumps in Chapter 4. The crystals

are made by sintering of silica beads and their robust nature is ideal for this pump. The interconnected beads are in a hexagonal closed packing with tetragonal and orthogonal voids formed in the arrangement of the silica spheres. These voids serve as the channels for thermal transpiration. The samples could be formed in any size which determines the flowrate and pressure difference obtained by the pump. This porous silica pump has been successfully tested for human and solar powered Knudsen pumps. Although silica aerogels were also tried for the same purpose, their delicate nature decreases the yield and operational ease of these types of pumps. The solar and human powered pumps perform nicely without any active input power. Thus, it opens up the possibility of using these pumps in remote places for drug delivery in humans by using the body temperature powered pump and it also finds use in running the pump using waste heat recovery. The flowrates (0.017 mL/min – 0.136 mL/min) achieved by these passive pumps are on the level of some of the micro pumps pumps used in modern drug delivery devices.

After the success with the passive pumps the need was still there to find even lower thermally conducting nanoporous membranes for which a 105 μm cellulose ester porous filter membrane is used for gas pumping. These polymer membranes have an order of magnitude lower thermal conductivity value compared to that of silica colloidal crystal. Thus, they are able to maintain a higher temperature gradient for the same input power within a shorter channel length which dramatically improves the flowrate and thus the overall efficiency of the pump. However, with only active heating and passive cooling the pump performance is limited. Thus, when a thermoelectric is employed to actively heat and cool each end simultaneously, the heat sink is eliminated, the pump becomes bidirectional and the net molecular flux from cold to hot side is increased by

attaining much lower temperatures at the cold end that could not have been possible with only active heating of the hot side. The normalized flowrate (1.5 sccm/cm^2) reported is to date the highest achieved by any Knudsen pump with the radial pump design using a thermoelectric. The radial design has better uniformity in heat distribution across the entire membrane and the thermal resistances due to air gap also could be optimized as compared to that of the lateral pump with the thermoelectric.

The polymer based pump has also been characterized for optimum pore size and efficiency. The pore size characterization experiment throws light into the fact that a better pump is obtained when the channel size has a higher Knudsen number. On the other hand it also shows that practically it is possible to get thermal transpiration effect close to viscous flow regime. The pressure-flow curve characteristics show that at no load much higher flowrates could be achieved by the pump. The overall efficiency of a thermoelectric pump with smaller active pump area has been found to be higher compared to a conventional Knudsen pump whose active pump area is 10 times larger than the former.

There is still room for improvement with the thermoelectric design as any amount of air gap will reduce the temperature across the nanoporous material. Also, the heat spreaders contribute to significant thermal losses to the environment. To eliminate these shortcomings it is desired to make the nano channels out of the thermoelectric material itself. This approach necessitates the use of a nano-porous thermoelectric. The nanoporous thermoelectric is expected to make the pump compact, reduce power consumption, and reduce energy losses. Also, the thermoelectric material may achieve a higher figure of merit compared to its bulk counterpart due to the nano pores which by

quantum confinement reduces the thermal conductivity of the material and thus enhances the figure of merit.

In Chapter 7 several approaches have been tried to fabricate leak free porous thermoelectric material. Also, different thermoelectric materials have been experimented with to get a better Peltier cooling. The technique of hot pressing worked for bismuth but not for bismuth telluride. Bismuth telluride has a higher figure of merit so is a better thermoelectric than bismuth but also has a higher melting point than bismuth which makes hot pressing difficult. The porous silicon membranes showed high contact resistance which indicated the reduction of electrical conductivity during porous silicon formation. The MOCVD of tellurium on the porous host structure was non-uniform which left wider channels in the sample after etching away the silica and thus had leakage paths and was very fragile to integrate the pump. In the next section the present work in progress on making a nanoporous thermoelectric is briefly described with the results obtained so far.

8.2 Future work

Abderrazzak Faiz, a PhD candidate in Mechanical Engineering at the University of Louisville, is continuing this research project. He has demonstrated that the nanoporous thermoelectric concept, discussed in Chapter 7, is feasible by using the sintering process.

8.2.1 Sintering process

The process flowchart in *Figure 83* describes the process of sintering. As smaller particle size is required to form nanopores the grain size of the thermoelectric material has to be really small in the order of the pore size. To make such finer grains ball milling

is employed. The powder is obtained by milling the pellets of the thermoelectric obtained from Align Sourcing LLC. These are both n and p type doped bismuth telluride pellets used to obtain a high Z thermoelectric material so as to get the maximum temperature difference which is essential for an efficient Knudsen pump.

The powder is pressed in the die and then the die is heated slowly to the required sintering temperature then left at that condition for some time. Then the temperature is brought back to room temperature and the pressure released. The sintered sample is tapped out from the die.

8.2.2 Sintered bismuth telluride porous pump

The sintered sample is tested for its thermoelectric properties as well as pore formation.

The thermoelectric properties are tested by measuring the thermopower of the sample.

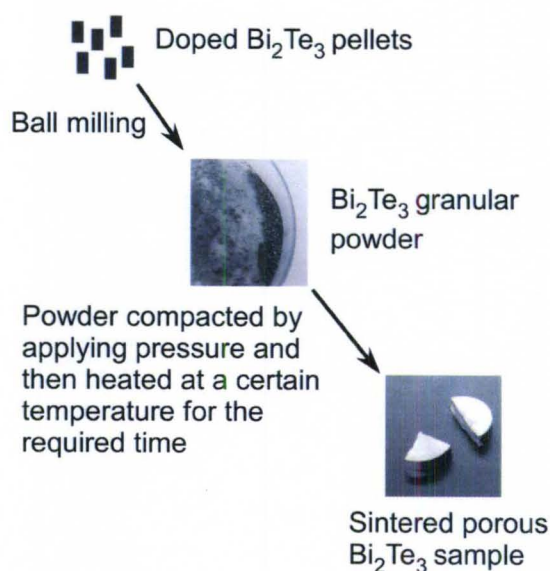


Figure 83. Sintering process flow.

The pores on the surface of the sample are imaged using a scanning electron microscope. Then electrical connections are made on either side of the porous sample depending on which length the temperature difference is to be obtained. Thereafter, the sample with the electrical connection on one side is mounted on a metallic base and glued with vacuum epoxy. The metallic base acts as a fixture for the connection of the inlet from the sensor to the sample and also serves as a heat sink. The fabricated pump is shown in *Figure 84*.

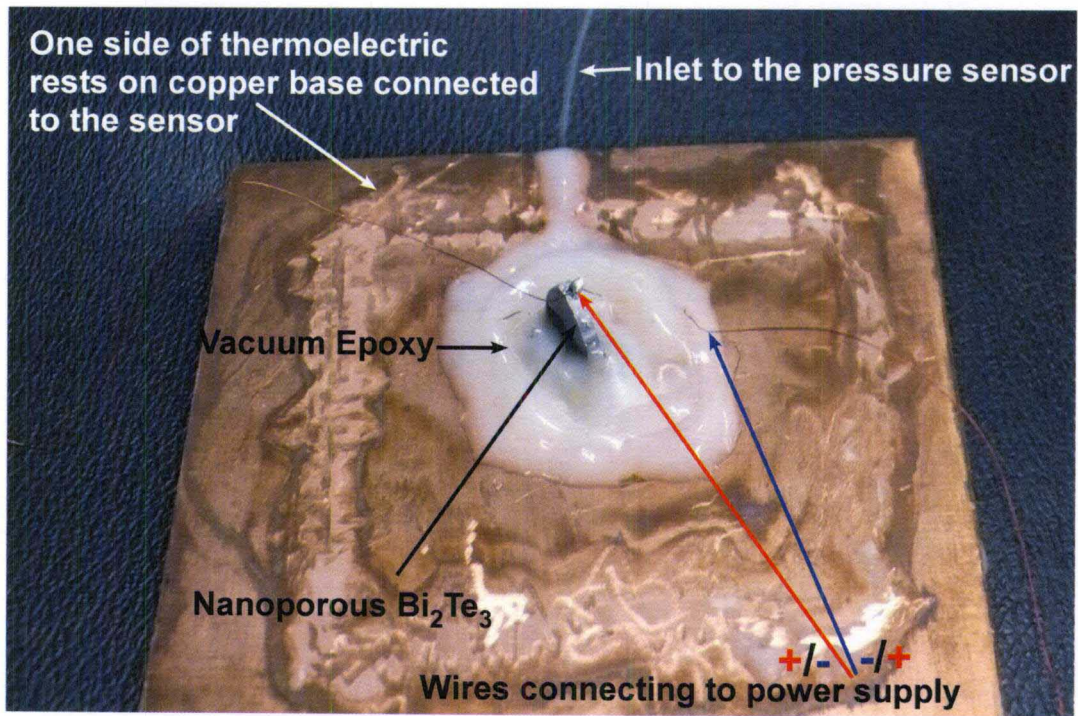


Figure 84. Sintered nano porous thermoelectric pump with inlet and power connectors.

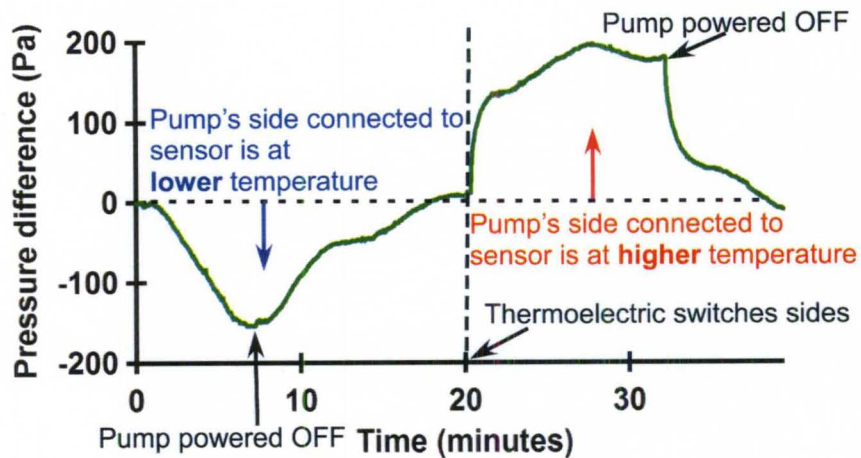


Figure 85. Pressure sensor connected to the pump measured the change in pressure at the cold side of the pump as against the ambient pressure in both modes of operation. The net difference in pump pressure is plotted in both forward and reverse pumping modes.

8.2.3 Results for the sintered pump

The pump has so far been only tested in the pressure mode in both forward and reverse directions. The testing procedure is the same as that in the earlier chapters.

Figure 85 shows the graph for the pressure mode testing. It is clearly seen that pumping has taken place due to Peltier effect from the thermoelectric and the direction of pumping reverses with the change in polarity of the supply voltage to the thermoelectric. The pressure difference when measured at the end of the porous thermoelectric which is at a lower temperature drops down and then the pump is powered OFF. The graph goes back up to catch up with the ambient pressure when there is no more pumping. Then with the voltage polarity to the thermoelectric reversed the previously cold end of the porous thermoelectric now becomes the hotter side and pumping takes place in the reverse direction which is evident from the graph since it rises above the ambient pressure. Again with the pump OFF the graph comes back to the normal ambient pressure mark. The

pressure drop magnitude is asymmetric due to the fact that on one side of the porous thermoelectric a heat sink is used to hold the pump to the sensor attachment. So, when the thermoelectric side attached to that plate is cooling the heat sink facilitates the cooling but when the side is heating the mass of the heat sink results in temperature loss and thus the magnitude of temperature difference is not the same in both modes of pumping and.

This is a preliminary result to just prove the concept and it has tremendous scope of improvement in future. Thereafter the porous thermoelectric pump could be used for potential applications like generation of pneumatic power for microfluidic devices and it could also be used for generating electrical power by supplying heat energy. Work is in progress to tailor the channel size, increase porosity, develop better electrical contacts and doping of materials for making a better pump.

Table 9 below summarizes the major Knudsen pumps and compressors built to date and highlights the results of their pumping characteristics:

Pump Maker - Year	Type of Knudsen Pump	Max. Flowrate (mL/min)	Max. ΔP (kPa)	Input Power (W)	Directionality	Footprint (mm ²)	Fabrication	Efficiency
Young et al @ USC - 2005[27]	Porous aerogel	0.24	1.07	0.065 /cm ²	Unidirectional	--	Easy	--
McNamara et al @ UMich - 2005 [29]	Microfabricated lateral design	10 ⁻⁶	54.7	0.08	Unidirectional	1.5 x 2	Complex	2.85E-09
Gupta et al @ UMich - 2008[30]	Porous zeolite	0.12	1	5.35	Unidirectional	55x55	Easy	9.35E-08
Gupta et al @ UMich - 2009[31]	Porous ceramic - 9 stages	0.0037	12	3.4	Unidirectional	25x25	Moderate	5.44E-08
Gupta et al @ UMich - 2010[118]	Porous polymer	0.4	0.33	1.4	Unidirectional	14x14	Easy	3.93E-07
Pharas et al @ UofL - 2010[119]	Porous multiple polymer membranes with thermoelectric	0.125	0.483	3.65	Bidirectional	29x29	Easy	6.89E-08
Pharas et al @ UofL - 2010[15]	Porous single polymer membrane with thermoelectric	0.74	1.69	8.5	Bidirectional	37x37	Easy	6.13E-07
Bell et al @ UofL - 2011	Colloidal silica - solar powered	0.136	0.414	0	Unidirectional	22.5x22.5	Easy	--
Bell et al @ UofL - 2011	Colloidal silica - human powered	0.017	1.5	0	Unidirectional	11x11	Easy	--
Abderazzak et al (in progress) @ UofL	Doped porous bismuth telluride	Not measured yet	0.15	0.3	Bidirectional	--	Moderate	--

Table : 9. Table summarizing the major Knudsen pumps made to date highlighting their pumping characteristics.

REFERENCES

- [1] Y. Fukuta, Y. A. Chapuis, Y. Mita, and H. Fujita, "Design, fabrication, and control of MEMS-based actuator arrays for air-flow distributed micromanipulation," *Journal of Microelectromechanical Systems*, vol. 15, pp. 912-926, Aug 2006.
- [2] S. V. Garimella, V. Singhal, and D. Liu, "On-chip thermal management with microchannel heat sinks and integrated micropumps," *Proceedings of the Ieee*, vol. 94, pp. 1534-1548, Aug 2006.
- [3] C. J. Lu, W. H. Steinecker, W. C. Tian, M. C. Oborny, J. M. Nichols, M. Agah, J. A. Potkay, H. K. L. Chan, J. Driscoll, R. D. Sacks, K. D. Wise, S. W. Pang, and E. T. Zellers, "First-generation hybrid MEMS gas chromatograph," *Lab on a Chip*, vol. 5, pp. 1123-1131, 2005.
- [4] R. Yokokawa, T. Saika, T. Nakayama, H. Fujita, and S. Konishi, "On-chip syringe pumps for picoliter-scale liquid manipulation," *Lab on a Chip*, vol. 6, pp. 1062-1066, 2006.
- [5] D J Laser and J. G. Santiago, "A review of micropumps," *Journal of Micromechanics and Microengineering*, vol. 14, 2004.
- [6] H. Kim, A. A. Astle, K. Najafi, L. P. Bernal, and P. D. Washabaugh, "A fully integrated high-efficiency peristaltic 18-stage gas micropump with active microvalves," in *20th IEEE International Conference on Micro Electro Mechanical Systems, MEMS 2007, January 21, 2007 - January 25, 2007*, Kobe, Japan, 2007, pp. 131-134.
- [7] S. Bohm, W. Olthuis, and P. Bergveld, "A plastic micropump constructed with conventional techniques and materials," *Sensors and Actuators a-Physical*, vol. 77, pp. 223-228, Nov 1999.
- [8] K. P. Kamper, J. Dopfer, W. Ehrfeld, and S. Oberbeck, "A self-filling low-cost membrane micropump," in *Proceedings IEEE Eleventh Annual International Workshop on Micro Electro Mechanical Systems An Investigation of Micro Structures, Sensors, Actuators, Machines and Systems, 25-29 Jan. 1998*, New York, NY, USA, 1998, pp. 432-7.

- [9] A. Wego and L. Pagel, "A self-filling micropump based on PCB technology," *Sensors and Actuators a-Physical*, vol. 88, pp. 220-226, Mar 2001.
- [10] E. Meng, W. Xuan-Qi, H. Mak, and T. Yu-Chong, "A check-valved silicone diaphragm pump," in *Proceedings IEEE Thirteenth Annual International Conference on Micro Electro Mechanical Systems, 23-27 Jan. 2000*, Piscataway, NJ, USA, 2000, pp. 62-7.
- [11] K. S. Yun, I. J. Cho, J. U. Bu, C. J. Kim, and E. Yoon, "A surface-tension driven micropump for low-voltage and low-power operations," *Journal of Microelectromechanical Systems*, vol. 11, pp. 454-461, Oct 2002.
- [12] A. Richter, A. Plettner, K. A. Hofmann, and H. Sandmaier, "A MICROMACHINED ELECTROHYDRODYNAMIC (EHD) PUMP," *Sensors and Actuators a-Physical*, vol. 29, pp. 159-168, Nov 1991.
- [13] D. J. Laser, A. M. Myers, Y. Shuhuai, K. F. Bell, K. E. Goodson, J. G. Santiago, and T. W. Kenny, "Silicon electroosmotic micropumps for integrated circuit thermal management," in *IEEE International Solid-State Sensors and Actuators Conference, 8-12 June 2003*, Piscataway, NJ, USA, 2003, pp. 151-4.
- [14] J. S. Jang and S. S. Lee, "Theoretical and experimental study of MHD (magnetohydrodynamic) micropump," *Sensors and Actuators a-Physical*, vol. 80, pp. 84-89, Mar 2000.
- [15] K. Pharas and S. McNamara, "Knudsen pump driven by a thermoelectric material," *Journal of Micromechanics and Microengineering*, vol. 20, 2010.
- [16] J. M. Edwards, M. N. Hamblin, H. V. Fuentes, B. A. Peeni, M. L. Lee, A. T. Wooley, and A. R. Hawkins, "Thin film electro-osmotic pumps for biomicrofluidic applications," *Biomicrofluidics*, vol. 1, pp. 014101(1)-014101(11), 2007.
- [17] Shunichi Hayamizu, Kusunoki Higashino, Yasuhisa Fujii, Yasuhiro Sando, and K. Yamamoto, "Development of a bi-directional valve-less silicon micro pump controlled by driving waveform," *Sensors and Actuators A*, vol. 103, pp. 83-87, 2003.
- [18] O. Reynolds, "On certain Dimensional Properties of Matter in the Gaseous State," *Phil. Trans. R. Soc. Lond.*, vol. 170, pp. 727-845, 1879.
- [19] J. C. Maxwell, "On Stresses in Rarified Gases Arising from Inequalities of Temperature," *Phil. Trans. R. Soc. Lond.*, vol. 170, pp. 231-256, 1879.
- [20] M. Knudsen, "Eine Revision der Gleichgewichtsbedingung der Gase. Thermische Molekularströmung," *Annalen der Physik*, vol. 336, pp. 205-229, 1909.

- [21] M. Knudsen, "Thermischer Molekulardruck der Gase in Röhren," *Annalen der Physik*, vol. 338, pp. 1435-1448, 1910.
- [22] K. Martin, *Kinetic Theory of Gases*, Third ed.: London Methuen & Co. Ltd. New York John Wiley & Sons. Inc., 1950.
- [23] J.P.Hobson, "Accommodation Pumping—A New Principle for Low Pressures " *JVST*, vol. 7, 1970.
- [24] D. H. Tracy, "THERMOMOLECULAR PUMPING EFFECT," *Journal of Physics E-Scientific Instruments*, vol. 7, pp. 533-536, 1974.
- [25] G. Pham-Van-Diep, P. Keeley, E. P. Muntz, and D. P. Weaver, "A micromechanical Knudsen Compressor," in *19th International Symposium on Rarefied Gas Dynamics*, 1995, pp. 715-721.
- [26] S. E. Vargo, "The development of the MEMS Knudsen compressor as a low power vacuum pump for portable and in situ instruments," University of Southern California Ph.D., ProQuest, UMI Dissertations Publishing, 2000.
- [27] M. Young, Y. L. Han, E. P. Muntz, and G. Shiflett, "Characterization and Optimization of a Radiantly Driven Multi-Stage Knudsen Compressor," *AIP Conference Proceedings*, vol. 762, pp. 174-179, 2005.
- [28] Y. L. Han and E. P. Muntz, "Experimental investigation of micro-mesoscale Knudsen compressor performance at low pressures," *Journal of Vacuum Science & Technology B*, vol. 25, pp. 703-714, 2007.
- [29] Shamus McNamara and Y. B. Gianchandani, "On-Chip Vacuum Generated by a Micromachined Knudsen Pump," *Journal of Microelectromechanical Systems*, vol. 14, pp. 741-746, 2005.
- [30] Naveen K. Gupta and Y. B. Gianchandani, "Thermal Transpiration in zeolites: A mechanism for motionless gas pumps," *Applied Physics Letters*, vol. 93, 2008.
- [31] N. K. Gupta and Y. B. Gianchandani, "A PLANAR CASCADING ARCHITECTURE FOR A CERAMIC KNUDSEN MICROPUMP," in *Transducers*, Denver,CO,USA, 2009.
- [32] D. Copic and S. McNamara, "Efficiency derivation for the Knudsen pump with and without thermal losses," *J.Vac.Sci.Technology A*, vol. 27(3), pp. 486-502, 2009.
- [33] Y.-L. Han, "Thermal-Creep-Driven Flows in Knudsen Compressors and Related Nano/Microscale Gas Transport Channels," *Journal of Microelectromechanical Systems*, vol. 17, pp. 984-997, 2008.

- [34] X. Guo, D. Singh, J. Murthy, and A. A. Alexeenko, "Numerical simulation of gas-phonon coupling in thermal transpiration flows," *Phys Rev E Stat Nonlin Soft Matter Phys*, vol. 80, p. 046310, 2009.
- [35] Y.-L. Han, E. P. Muntz, A. Alexeenko, and M. Young, "Experimental and computational studies of temperature gradient-driven molecular transport in gas flows through nano/microscale channels," *Nanoscale and Microscale Thermophysical Engineering* vol. 11, pp. 151-175, 2007.
- [36] Y. Sone, Y. Waniguchi, and K. Aoki, "One-way flow of a rarefied gas induced in a channel with a periodic temperature distribution," *Physics of Fluids*, vol. 8, pp. 2227-2235, 1996.
- [37] A. Passian, R. J. Warmack, T. L. Ferrell, and T. Thundat, "Thermal transpiration at the microscale: A Crookes cantilever," *Physical Review Letters*, vol. 90, 2003.
- [38] Karniadakis and Beskok, Eds., *Micro Flows Fundamentals and Simulations*. New York: Springer Verlag, 2002.
- [39] M. Knudsen, *Ann.Phys(Leipzig)*, vol. 4, 1915.
- [40] E. H. Kennard, *Kinetic Theory Of Gases*: McGraw-Hill Book Company, Inc., 1938.
- [41] Y. Sone, *Kinetic Theory and Fluid Dynamics*: Birkhauser, 2002.
- [42] J. C. Williams, "THERMAL TRANSPIRATION - A CONTINUUM GASDYNAMICS VIEW," *Journal of Vacuum Science & Technology*, vol. 8, pp. 446-&, 1971.
- [43] L. B. Loeb, *The kinetic Theory Of Gases*: Dover Publications, Inc, 1961.
- [44] S. Felix, "Application of the Cercignani–Lampis scattering kernel to calculations of rarefied gas flows. II. Slip and jump coefficients," *European Journal of Mechanics - B/Fluids*, vol. 22, pp. 133-143.
- [45] F.M.Sharipov, "Rarefied Gas Flow through a Long Tube at Arbitrary Pressure and Temperature Drops," *Journal of Vacuum Science and Technology A*, vol. 15, pp. 2434-2436, July 1997 1997.
- [46] F. Sharipov, "Non-isothermal gas flow through rectangular microchannels," *Journal of Micromechanics and Microengineering*, vol. 9, pp. 394-401, Dec 1999.
- [47] M. Nathan, "Efficient Numerical Techniques for Multiscale Modeling of Thermally Driven Gas Flows with Application to Thermal Sensing Atomic Force

- Microscopy," PhD, Mechanical Engineering, Georgia Institute of Technology, 2006.
- [48] S. E. Vargo, E. P. Muntz, G. R. Shiflett, and W. C. Tang, "Knudsen compressor as a micro- and macroscale vacuum pump without moving parts or fluids," *Journal of Vacuum Science & Technology a-Vacuum Surfaces and Films*, vol. 17, pp. 2308-2313, 1999.
- [49] Y.-L. Han, "Investigation of micro/meso-scale Knudsen compressors at low pressures," PhD, University of Southern California, 2006.
- [50] J. J. M. Beenakker, V. D. Borman, and S. Y. Krylov, "MOLECULAR-TRANSPORT IN THE NANOMETER REGIME," *Physical Review Letters*, vol. 72, pp. 514-517, Jan 1994.
- [51] J. J. M. Beenakker, V. D. Borman, and S. Y. Krylov, "MOLECULAR-TRANSPORT IN SUBNANOMETER PORES - ZERO-POINT ENERGY, REDUCED DIMENSIONALITY AND QUANTUM SIEVING," *Chemical Physics Letters*, vol. 232, pp. 379-382, Jan 1995.
- [52] M. Whitby and N. Quirke, "Fluid flow in carbon nanotubes and nanopipes," *Nature Nanotechnology*, vol. 2, pp. 87-94, 2007.
- [53] Z. G. Li and L. Hong, "On the Knudsen transport of gases in nanochannels," *Journal of Chemical Physics*, vol. 127, Aug 2007.
- [54] H. J. Goldsmid, *Introduction to Thermoelectricity*: Springer, 2009.
- [55] A. I. Hochbaum, R. K. Chen, R. D. Delgado, W. J. Liang, E. C. Garnett, M. Najarian, A. Majumdar, and P. D. Yang, "Enhanced thermoelectric performance of rough silicon nanowires," *Nature*, vol. 451, pp. 163-U5, 2008.
- [56] A. I. Boukai, Y. Bunimovich, J. Tahir-Kheli, J.-K. Yu, W. A. G. III, and J. R. Heath, "Silicon nanowires as efficient thermoelectric materials," *Nature* vol. 451, 2008.
- [57] L. D. Hicks and M. S. Dresselhaus, "EFFECT OF QUANTUM-WELL STRUCTURES ON THE THERMOELECTRIC FIGURE OF MERIT," *Physical Review B*, vol. 47, pp. 12727-12731, 1993.
- [58] L. D. Hicks and M. S. Dresselhaus, "THERMOELECTRIC FIGURE OF MERIT OF A ONE-DIMENSIONAL CONDUCTOR," *Physical Review B*, vol. 47, pp. 16631-16634, 1993.
- [59] A. Shakouri, "Nanoscale Thermal Transport and Microrefrigerators on a Chip," in *Proceedings of the IEEE*, 2006.

- [60] W. Kim, J. Zide, A. Gossard, D. Klenov, S. Stemmer, A. Shakouri, and A. Majumdar, "Thermal conductivity reduction and thermoelectric figure of merit increase by embedding nanoparticles in crystalline semiconductors," *Physical Review Letters*, vol. 96, 2006.
- [61] J.-H. Lee, G. A. Galli, and J. C. Grossman, "Nanoporous Si as an Efficient Thermoelectric Material " *Nano Letters*, vol. 8, pp. 3750-3754, 2008.
- [62] M. Datta, R. D. Whaley, and M. Dagenais, "Design and fabrication of thin film resistive heaters for hybrid optoelectronic packaging," *Ieee Transactions on Advanced Packaging*, vol. 25, pp. 495-502, 2002.
- [63] R. F. Wolffenbuttel, "Low-temperature intermediate Au-Si wafer bonding; eutectic or silicide bond," *Sensors and Actuators a-Physical*, vol. 62, pp. 680-686, 1997.
- [64] Y. T. Cheng, L. W. Lin, and K. Najafi, "Localized silicon fusion and eutectic bonding for MEMS fabrication and packaging," *Journal of Microelectromechanical Systems*, vol. 9, pp. 3-8, 2000.
- [65] L. Jungchul, T. L. Wright, M. R. Abel, E. O. Sunden, Alexei Marchenkov, Samuel Graham, and W. P. King, "Thermal conduction from microcantilever heaters in partial vacuum," *Journal of Applied Physics*, vol. 101, pp. 1-6, 2007.
- [66] C. M. Jha, M. A. Hopcroft, and Manu Agarwal, "IN-CHIP DEVICE-LAYER THERMAL ISOLATION OF MEMS RESONATOR FOR LOWER POWER BUDGET," in *ASME International Mechanical Engineering Congress and Exposition*, Chicago, Illinois, USA, 2006.
- [67] C. Gwiy-Sang, "Fabrication and characterization of micro-heaters with low-power consumption using SOI membrane and trench structures," *Sensors and Actuators A*, vol. 112, pp. 55-60, 2003.
- [68] Z. Wenhua, Z. Weibin, and Kimberly Turner, "SCREAM'03: A SINGLE MASK PROCESS FOR HIGH-Q SINGLE CRYSTAL SILICON MEMS," in *2004 ASME International Mechanical Engineering Congress and Exposition*, Anaheim, California USA, 2004.
- [69] N. Miki, X. Zhang, R. Khanna, A. A. Ayon, D. Ward, and S. M. Spearing, "Multi-stack silicon-direct wafer bonding for 3D MEMS manufacturing," *Sensors and Actuators a-Physical*, vol. 103, pp. 194-201, 2003.
- [70] U. Gosele, Q. Y. Tong, A. Schumacher, G. Krauter, M. Reiche, A. Plossl, P. Kopperschmidt, T. H. Lee, and W. J. Kim, "Wafer bonding for microsystems technologies," *Sensors and Actuators a-Physical*, vol. 74, pp. 161-168, 1999.

- [71] J. L. Perry and S. G. Kandlikar, "Review of fabrication of nanochannels for single phase liquid flow," *Microfluidics and Nanofluidics*, vol. 2, pp. 185-193, 2006.
- [72] P. Abgrall, L. N. Low, and N. T. Nguyen, "Fabrication of planar nanofluidic channels in a thermoplastic by hot-embossing and thermal bonding," *Lab on a Chip*, vol. 7, pp. 520-522, 2007.
- [73] S. R. Quake and A. Scherer, "From micro- to nanofabrication with soft materials," *Science*, vol. 290, pp. 1536-1540, 2000.
- [74] X. D. Huang, L. R. Bao, X. Cheng, L. J. Guo, S. W. Pang, and A. F. Yee, "Reversal imprinting by transferring polymer from mold to substrate," *Journal of Vacuum Science & Technology B*, vol. 20, pp. 2872-2876, 2002.
- [75] J. J. Dumond, H. Y. Low, and I. Rodriguez, "Isolated, sealed nanofluidic channels formed by combinatorial-mould nanoimprint lithography," *Nanotechnology*, vol. 17, pp. 1975-1980, 2006.
- [76] L. J. Guo, X. Cheng, and C. F. Chou, "Fabrication of size-controllable nanofluidic channels by nanoimprinting and its application for DNA stretching," *Nano Letters*, vol. 4, pp. 69-73, 2004.
- [77] Y. P. Kong, H. Y. Low, S. W. Pang, and A. F. Yee, "Duo-mold imprinting of three-dimensional polymeric structures," *Journal of Vacuum Science & Technology B*, vol. 22, pp. 3251-3256, 2004.
- [78] C. Liu, "Recent developments in polymer MEMS," *Advanced Materials*, vol. 19, pp. 3783-3790, 2007.
- [79] L. Brown, T. Koerner, J. H. Horton, and R. D. Oleschuk, "Fabrication and characterization of poly(methylmethacrylate) microfluidic devices bonded using surface modifications and solvents," *Lab on a Chip*, vol. 6, pp. 66-73, 2006.
- [80] J. C. T. Eijkel, J. Bomer, N. R. Tas, and A. Van Den Berg, "1-D nanochannels fabricated in polyimide," *Lab on a Chip*, vol. 4, pp. 161-163, 2004.
- [81] Chakravarthy Yamarthy, Kunal Pharas, Alexander Schultz, and S. McNamara, "Pneumatic Pumping of Liquids Using Thermal Transpiration for Lab-on-a-Chip Applications," in *Proceedings of IEEE Sensors*, NewZealand, 2009.
- [82] H. Song, M. R. Bringer, J. D. Tice, C. J. Gerdt, and R. F. Ismagilov, "Experimental test of scaling of mixing by chaotic advection in droplets moving through microfluidic channels," *Applied Physics Letters*, vol. 83, pp. 4664-4666, 2003.

- [83] D. S. Reichmuth, T. J. Shepodd, and B. J. Kirby, "Microchip HPLC of peptides and proteins," *Analytical Chemistry*, vol. 77, pp. 2997-3000, 2005.
- [84] S. Tia and A. E. Herr, "On-chip technologies for multidimensional separations," *Lab on a Chip*, vol. 9, pp. 2524-2536, 2009.
- [85] S. Haeberle and R. Zengerle, "Microfluidic platforms for lab-on-a-chip applications," *Lab on a Chip*, vol. 7, pp. 1094-1110, 2007.
- [86] M. A. Burns, C. H. Mastrangelo, T. S. Sammarco, F. P. Man, J. R. Webster, B. N. Johnson, B. Foerster, D. Jones, Y. Fields, A. R. Kaiser, and D. T. Burke, "Microfabricated structures for integrated DNA analysis," *Proceedings of the National Academy of Sciences of the United States of America*, vol. 93, pp. 5556-5561, 1996.
- [87] J. W. Van Honschoten, M. Escalante, N. R. Tas, and M. Elwenspoek, "Formation of liquid menisci in flexible nanochannels (vol 329, pg 133, 2009)," *Journal of Colloid and Interface Science*, vol. 332, pp. 520-520, 2009.
- [88] Ngyuen and Werely, *Fundamentals and Applications of Microfluidics*, Second ed. Boston: Artech House, 2006.
- [89] Henrik Bruus, *Theoretical Microfluidics*: Oxford University press, 2008.
- [90] A. Hamraoui and T. Nylander, "Analytical approach for the Lucas-Washburn equation," *Journal of Colloid and Interface Science*, vol. 250, pp. 415-421, 2002.
- [91] P. B. Allen and D. T. Chiu, "Calcium-assisted glass-to-glass bonding for fabrication of glass microfluidic devices," *Analytical Chemistry*, vol. 80, pp. 7153-7157, 2008.
- [92] A. A. Zakhidov, R. H. Baughman, Z. Iqbal, C. Cui, I. Khayrullin, S. O. Dantas, H. Marti, and V. Ralchenko, "Carbon Structures with Three-Dimensional Periodicity at Optical Wavelengths," *Science*, vol. 282, 1998.
- [93] http://www.coleparmer.com/Catalog/0708_pdf_International/KH_0460.pdf.
- [94] <http://www.whatman.com/MixedCelluloseEsterMembranes.aspx>.
- [95] D. W. Song, W.-N. Shen, B. Dunn, C. D. Moore, M. S. Goorsky, T. Radetic, R. Gronsky, and G. Chen, "Thermal conductivity of nanoporous bismuth thin films," *Applied Physics Letters*, vol. 84, 2004.
- [96] W. Shen, B. Dunn, F. Ragot, M. Goorsky, C. Moore, D. W. Song, G. Chen, R. Gronsky, T. Radetic, W. Fuller-Mora, and A. Ehrlich, "Microstructure-property relations for porous bismuth films," in *International Conference on Thermoelectrics*, 1999.

- [97] H. J. Goldsmid, "Bismuth - The thermoelectric material of the future?," Vienna, Austria, 2006, pp. 5-10.
- [98] S. R. Hostler, Y. Q. Qu, M. T. Demko, A. R. Abramson, X. Qiu, and C. Burda, "Thermoelectric properties of pressed bismuth nanoparticles," *Superlattices and Microstructures*, vol. 43, pp. 195-207, 2008.
- [99] J.-H. Lee, G. A. Galli, and J. C. Grossman, "Nanoporous Si as an efficient thermoelectric material," *Nano Letters*, vol. 8, pp. 3750-3754, 2008.
- [100] A. Yamamoto, H. Yakazawa, and T. Ohta, "Thermoelectric transport properties of Porous Silicon Nanostructure," in *18th Intl. Conf. on Thermoelectrics*, 1999, pp. 428-431.
- [101] A. G. Cullis and L. T. Canham, "VISIBLE-LIGHT EMISSION DUE TO QUANTUM SIZE EFFECTS IN HIGHLY POROUS CRYSTALLINE SILICON," *Nature*, vol. 353, pp. 335-338, 1991.
- [102] V. Lysenko, P. Roussel, B. Remaki, G. Delhomme, A. Dittmar, D. Barbier, V. Strikha, and C. Martelet, "Study of nano-porous silicon with low thermal conductivity as thermal insulating material," *Journal of Porous Materials*, vol. 7, pp. 177-182, 2000.
- [103] V. Lysenko, S. Perichon, B. Remaki, and D. Barbier, "Thermal isolation in microsystems with porous silicon," *Sensors and Actuators a-Physical*, vol. 99, pp. 13-24, 2002.
- [104] S. Perichon, V. Lysenko, P. Roussel, B. Remaki, B. Champagnon, D. Barbier, and P. Pinard, "Technology and micro-Raman characterization of thick meso-porous silicon layers for thermal effect microsystems," *Sensors and Actuators, A: Physical*, vol. 85, pp. 335-339, 2000.
- [105] V. Lehmann, "Developments in porous silicon research," *Materials Letters*, vol. 28, pp. 245-249, 1996.
- [106] V. Lehmann, "Trends in fabrication and applications of macroporous silicon," *Physica Status Solidi a-Applied Research*, vol. 197, pp. 13-15, 2003.
- [107] X. G. Zhang, "MECHANISM OF PORE FORMATION ON N-TYPE SILICON," *Journal of the Electrochemical Society*, vol. 138, pp. 3750-3756, 1991.
- [108] V. Lehmann and U. Gosele, "POROUS SILICON FORMATION - A QUANTUM WIRE EFFECT," *Applied Physics Letters*, vol. 58, pp. 856-858, 1991.

- [109] V. Lehmann and U. Gosele, "POROUS SILICON - QUANTUM SPONGE STRUCTURES GROWN VIA A SELF-ADJUSTING ETCHING PROCESS," *Advanced Materials*, vol. 4, pp. 114-116, 1992.
- [110] L. Canham, "Properties of Porous Silicon," ed: Institution of Engineering and Technology.
- [111] X. G. Zhang, *Electrochemistry of Silicon and its Oxides*. New York: Kluwer Academic / Plenum Publisher, 2001.
- [112] Z. C. Feng and R. Tsu, Eds., *Porous Silicon*. 1994.
- [113] D.M.Rowe, Ed., *Handbook of Thermoelectrics*. CRC Press, 1995.
- [114] S. Arva and B. Alphenaar, "Determination of the hopping contribution to the thermopower in bismuth infiltrated colloidal crystals," *Journal of Applied Physics*, vol. 102, 2007.
- [115] A. Boulouz, A. Giani, F. Pascal-Delannoy, M. Boulouz, A. Foucaran, and A. Boyer, "Preparation and characterization of MOCVD bismuth telluride thin films," *Journal of Crystal Growth*, vol. 194, pp. 336-341, 1998.
- [116] P. C. Eklund and A. K. Mabatah, "Thermoelectric power measurements using analog subtraction," *Review of Scientific Instruments*, vol. 48, pp. 775-7, 1977.
- [117] K. Ishizaki, D. Komareni, and M. Nanko, *Porous materials: process technology and applications*. Dordrecht, Netherlands: Kluwer Academic Publishers, 1998.
- [118] N. K. Gupta and Y. B. Gianchandani, "A high-flow Knudsen pump using a polymer membrane: performance at and below atmospheric pressures," in *23rd IEEE International Conference on Micro Electro Mechanical Systems (MEMS 2010)*, 24-28 Jan. 2010, Piscataway, NJ, USA, 2010, pp. 1095-8.
- [119] K. Pharas and S. McNamara, "Bi-directional gas pump using a thermoelectric material," in *The 23rd IEEE International Conference on Micro Electro Mechanical Systems MEMS 2010*, Hong Kong, 2010, pp. 1103-1106.
- [120] <http://eetd.lbl.gov/ecs/aerogels/sa-thermal.html>
- [121] <http://www.professionalplastics.com>
- [122] <http://www.azom.com/article.aspx?ArticleID=1114>

APPENDIX A

Deep reactive Ion etching (DRIE) recipe for SCREAM like process:-

a) Bosch process:

Etch time - 9.5 sec

Pass time - 6 sec

Process time - 40 cycles

Line	Gas name	Etch		Passivate	
		Flow(sccm)	Tol(%)	Flow (sccm)	Tol(%)
1	C ₄ F ₈	0	5	75	50
2	SF ₆	160	50	0	5
3	O ₂	13	50	0	5
4	Ar	0	5	0	5

	Power (W)- Etch	Power (W) – Passivate
Coil	550	500
Platen	19	0

b) Passivation process:

Process time - 3 min

Line	Gas name	Flow(sccm)	Tol(%)
1	C ₄ F ₈	100	50
2	SF ₆	0	5
3	O ₂	0	5
4	Ar	0	5

	Power (w)
Coil	500
Platen	0

c) Bosch process with higher platen power:

Etch time - 9.5 sec

Pass time - 6 sec

Process time - 24 cycles

Line	Gas name	Etch		Passivate	
		Flow(sccm)	Tol(%)	Flow (sccm)	Tol(%)
1	C ₄ F ₈	0	5	75	50
2	SF ₆	160	50	0	5
3	O ₂	13	50	0	5
4	Ar	0	5	0	5

	Power (W) - Etch	Power (W) - Passivate
Coil	550	500
Platen	28	0

d) Isotropic etch:

Process time - 6 min (after this go on observing after each minute for like 5 minutes and stop process as soon as heaters start losing linewidths)

Line	Gas name	Flow(sccm)	Tol(%)
1	C ₄ F ₈	0	5
2	SF ₆	160	15
3	O ₂	0	5
4	Ar	0	5

	Power (W)
Coil	500
Platen	0

CURRICULUM VITAE

EDUCATION

- PhD. In Electrical Engineering University of Louisville,
Kentucky
GPA 3.57/4.00 *January 2007 - January 2012.*

PhD Thesis – “Thermally driven Knudsen Gas Pump enhanced with a Thermoelectric”

Adviser: Dr. Shamus McNamara – Department of Electrical and Computer Engineering.

- MS in Electrical Engineering University of Louisville,
Kentucky
GPA 3.49/4.00 *August 2004 – December 2006.*

MS Thesis – “Maskless Lithography”

Adviser: Dr. Shamus McNamara – Department of Electrical and Computer Engineering.

- BS in Electrical Engineering Engineering College Bilaspur,
India
First Division *August 1998- July 2002.*

PUBLICATIONS & CONFERENCE PRESENTATIONS

1. C. Yamarthy, K. Pharas, A. Schultz, and S. McNamara, "Pneumatic Pumping of Liquids Using Thermal Transpiration for Lab-on-a-Chip Applications," in *Proceedings International IEEE Sensors Conference*, New Zealand, 2009, pp. 1931-1934.
2. K. Pharas and S. McNamara, "Bi-directional gas pump using a thermoelectric material," in *The 23rd IEEE International Conference on Micro Electro Mechanical Systems MEMS 2010*, Hong Kong, 2010, pp. 1103-1106.
3. K. Pharas and S. McNamara, "Knudsen pump driven by a thermoelectric material," *Journal of Micromechanics and Microengineering*, vol. 20, 2010.
4. Poster presentation, “A MEMS gas pump with no moving parts”, 13th Annual Kentucky EPSCOR conference, Lexington, KY, October 2, 2007.
5. Technical presentation, “Solar Thermal Powered and Body Heat Powered Knudsen Gas Pump”, 9th Intl. Conference on Nanochannels, Microchannels and Minichannels, Edmonton, Canada, 19-22 June 2011.

PATENT: International Application No. PCT/US2010/053790. Publication Date 28 April 2011.

Work Experience and Summary of Qualifications:

- 6+ years of hands on experience in research and development in the field of microtechnology encompassing MEMS and semiconductor devices (design, fabrication and testing), as a research assistant.
- Worked on projects funded by national institutions like NSF and also contributed in writing successful grant proposals.
- Extensive experience as a teaching assistant to engineering classes at both graduate and undergraduate levels (Fall 2004 - Spring 2011).

OTHER AWARDS

- Awarded Graduate Student Assistantship by REACH at University of Louisville to mentor undergraduate students (August 2005 – May 2006).
- Awarded travel grant for conference travel abroad (January 2010).